Investigating the role of shocks, thermal instability and gravity in molecular cloud formation

Marcin Mikołaj Kupilas
School of Physics and Astronomy
University of Leeds

Submitted in accordance with
Doctor of Philosophy

April 2022

Preface

The chapters in this thesis are based on work presented in the following publications:

1. "Interactions of a shock with a molecular cloud at various stages of its evolution due to thermal instability and gravity", M.M. Kupilas, C.J. Wareing, J.M. Pittard, S.A.E.G. Falle, MNRAS, 2021, 501, 3137
2. "Shocking interactions of supernova remnants with atomic and molecular clouds - the interplay between shocks, thermal instability and gravity in the large cloud regime", M.M. Kupilas, J.M. Pittard, C.J. Wareing, S.A.E.G. Falle, 2022, MNRAS, in press

Paper 1 forms the basis of Chapter 3 and half of Chapter 5. Paper 2 forms the basis of Chapter 4. In all cases, the simulations were performed using the hydrodynamical MG code written and developed by S. A. E. G. Falle, and the heating and cooling prescription was developed by C. J. Wareing. The primary author M. M. Kupilas was responsible for small alterations of the code, the addition of the shock into the simulations, performing production simulations, data manipulation, analysis and interpretation, and writing up of the initial draft of the publications prior to incorporating comments from the co-authors and reviewers. The initial un-shocked model was based entirely on a 3D hydrodynamical scenario presented in Wareing *et al.* (2016a), and the subsequent scenario parameters were decided by the primary author, in conversation with the co-authors. A resolution test of the thermal instability was included in appendix A1 of Paper 1, which was conducted by S. A. E. G. Falle. This was not included in the Thesis.

Acknowledgements

I would like to first thank Dr Sven Van Loo for taking me on again as a student when I resat my Masters, and encouraging me to apply for this PhD. I am also grateful for his help as a secondary PhD supervisor, especially with getting into the swing of things with MG at the start. I would like to thank Prof Sam Falle for providing MG in the first place. More importantly however, I hope that through working with him, his relentless curiosity and hearty spirit has at least marginally rubbed off on me. I would like to thank my primary supervisors Dr Julian Pittard and Dr Christopher Wareing. It was an absolute privilege to be Chris's first PhD student. He was encouraging from the start, helped take the intimidation out from using MG, and kept my spirits up all the way to the finish line. His commitment throughout the process has been humbling, and I have only thanks to give - the next pint of Mythos is on me. It was also an absolute privilege to have been supervised by Julian. I have thoroughly enjoyed learning from him, and picking his brain on stellar feedback and numerical modelling - fields he's forgotten more about than most will ever know. His support and commitment, especially during the pandemic, has really been superlative. I would additionally like to thank Prof Jiannis Pachos, whom I have thoroughly enjoyed collaborating musically and drinking coffee with. It was also an honour to have played piano at his inauguration. I would like to also thank Prof Melvin Hoare and Dr Paul Clark for their Viva questions, feedback, and their great company, as well as everyone else's, at the Fenton and Thai Aroy Dee afterwards. I would like to give a massive thanks to my friends and

family. Everyone from the office, old and new, you are all inspiring, and I hope we do more Astro trips soon, as well as more trips to the Fenton. Johnny, you have always been an outstanding friend and soul brother, and it was a pleasure to have shared my PhD journey with yours. Isaac, I don't know why every conversation we had in the past 4 years escalated to the meaning of life or the system, but I blame you. Alice, after physically picking you up against your will on my first day in the office, I don't know why you've chosen to be such a dear friend to me, but for that I greatly appreciated you. I also want to give special thanks to Matt Girling, Wisdom Agboh, Brad Lister, Luke Holden and Olga Kondur, Cathie, Jill, Olivia, Martin, Caroline, Derek, who all lit up various parts of the past 4 years. Finally I want to say that without the love and support of my family, I could not have made it to this point. Mum and Dad, Agnieszka and Chris, I am profoundly grateful for everything you have done. Sarah, we met when I started the PhD and you have been by my side motivating and encouraging me for the entire ride. I have nothing but gratitude for your love, patience and unyielding strength of character.

Abstract

Using the MG code we performed hydrodynamical simulations to study the relative importance between the thermal instability (TI), gravity and shock impact in the process of molecular cloud formation out of an initially quiescent atomic medium. A total of five scenarios were considered in this Thesis: an un-shocked scenario, two planar shock-cloud scenarios in the *small cloud regime* in Chapter 3, and two supernova-cloud scenarios in the *large cloud regime* in Chapter 4. In both regimes the shock was introduced when the cloud was in a "pre-TI" warm atomic state prior to any noticeable action of the TI, and a "post-TI" state after cold and dense clumps have formed. This allowed us to study the effects of the presence/absence of clumps on the resulting dynamics.

In both shock-cloud scenarios, the planar shock significantly disrupted the clouds and the dynamics were shock dominated. The clouds showed evidence of local gravitational collapse on a 5.16 Myr timescale, which was not seen in our un-shocked clouds. In the pre-TI supernova-cloud case, the ambient pressure dropped below the cloud's after 1 Myr, causing the cloud to expand. Prior to this, the TI was triggered behind the transmitted shock which appeared to form low density clumps, but these did not collapse like in the shock-cloud scenarios. The post-TI supernova had negligible impact on the cloud, and after ~ 3.5 Myr it was almost indistinguishable from the un-shocked cloud - the pressure drop after 1 Myr had no effect either. Some clumps co-alesced and merged due to the impact of the transmitted shock, but this did not aid in collapsing any clumps.

In Chapter 5 we took advantage of the fact that the dynamics in the models were reasonably well understood in the previous chapters, and via a Fourier analysis derived the power spectra of velocity, density and density logarithm. While self-similar scaling was seen in many of the spectra, it was challenging to interpret this as representing turbulence in every case, with some spectra showing misleading results all together.

Contents

Abbreviations

AMR	Adaptive Mesh Refinement
CNM	Cold Neutral Medium
CR	Cosmic Ray
GMC	Giant Molecular Cloud
GOD	Godunov
HD	Hydrodynamics
HIM	Hot Ionized Medium
IR	Infrared
ISM	Interstellar Medium
KH	Kelvin-Helmholtz
KT	Kurganov-Tadmor
MC	Molecular Cloud
MHD	Magnetohydrodynamics
PAH	Polycyclic Aromatic Hydrocarbon
PE	Photoelectric
REC	Recombination
RH	Rankine-Hugoniot
RT	Rayleigh-Taylor
SN	Supernova
SNR	Supernova Remnant
TI	Thermal Instability

ABBREVIATIONS

UV	Ultraviolet
WIM	Warm Ionized Medium
WNM	Warm Neutral Medium
XR	X-Ray

List of Figures

List of Tables

Chapter 1

Introduction

1.1 Motivation

A central process in galactic evolution is the exchange of material and energy between stars and the interstellar medium (ISM). Stars form out of the ISM, and subsequent stellar feedback alters the ISM state thus affecting where, when and how future stellar generations form and evolve. The sites of star formation are molecular clouds (MCs) which themselves undergo a life-cycle of assembly, evolution and dispersal. Thus the study of star formation necessarily passes through the study of MCs.

MCs are typically characterised by their mass and size. From largest to smallest, these are giant molecular clouds (GMCs) ($M \gtrsim 10^5\,\mathrm{M}_\odot$, $R \sim 30-200\,\mathrm{pc}$), MCs ($M \sim 10^3-10^4\,\mathrm{M}_\odot$, $R \sim 2-15\,\mathrm{pc}$), clumps ($M \sim 50-500\,\mathrm{M}_\odot$, $R \sim 0.3-3\,\mathrm{pc}$) and cores ($M \sim 0.5-5\,\mathrm{M}_\odot$, $R \sim 0.03-0.2\,\mathrm{pc}$) (e.g. see table 1 in Bergin & Tafalla, 2007). Recently, filaments have also been added to the MC taxonomy (André *et al.*, 2014), as objects with aspect ratios of $\sim 5-10$, "characteristic width" of 0.1 pc, and mass and size ranges analogous to that of clumps and cores. All of these structures are nested in a hierarchical manner, characterised by non-thermal line-widths (Larson, 1981; Solomon *et al.*, 1987), with smaller and denser structures always occupying a very small fraction of their parent structures' volume.

1. INTRODUCTION

The physics that dominates at different stages of the MC life-cycle is not fully understood, with top-down and bottom-up processes all playing a role. From the top-down, spiral-arm compression (Dobbs *et al.*, 2008; Dobbs & Bonnell, 2008), magneto-rotational instability (Balbus & Hawley, 1991; Tamburro *et al.*, 2009) and galactic shear drives flows whose energies cascade down from galactic scales to smaller scales contributing to supersonic motions in the clouds. Accretion due to gravitationally driven flows and subsequent fragmentation can drive compressive supersonic motions on galactic scales down to scales of molecular clouds and pre-stellar cores (Hoyle, 1953; Field *et al.*, 2008; Klessen & Hennebelle, 2010; Clark *et al.*, 2011; Federrath *et al.*, 2011; Van Loo *et al.*, 2014). On molecular cloud scales, colliding flows and collisions with other clouds can be dynamically important (Wu *et al.*, 2018), and trigger the star formation process (Tan, 2000; Clark *et al.*, 2012; Wu *et al.*, 2015, 2017b,a). Once stars form, GMCs are subsequently affected from within by the feedback from the most massive stars in the form of winds, radiation and supernovae (e.g. Rogers & Pittard, 2013; Wareing *et al.*, 2016b, 2017; Wareing *et al.*, 2018).

Adding to the complexity of the problem, the strong density inhomogeneities observed in the ISM can also be attributed to thermal phase transitions due to inherent instabilities resulting from the balance of heating and cooling processes (Parker, 1953; Field, 1965; Field *et al.*, 1969; Wolfire *et al.*, 1995, 2003). This thermal instability (TI) can develop in association with other processes such as externally driven turbulence (e.g. Saury *et al.*, 2014), spiral-arm shocks (e.g. Yang & Krumholz, 2012; Kim *et al.*, 2008, 2010), gravity and magnetic fields (Wareing *et al.*, 2016a, hereafter WPFVL16).

To understand what physics dominates where and when in an evolving system, it is helpful to use numerical simulations. Here, the physical processes can be switched on or off, and incrementally introduced into the models. This was the case with previous work in our group conducted by WPFVL16, who incrementally introduced the physics of the TI, magnetic fields, gravity, and mechanical feedback due to winds and supernovae (Wareing *et al.*, 2016b, 2017; Wareing *et al.*, 2018). This allowed for a self-consistent study of of the full MC life-cycle of assembly, evolution and eventual dispersal due to stellar feedback and the incremental approach allowed the impact of each physical ingredient to be closely studied - it is an approach we choose to follow here.

In this Thesis, we perform hydrodynamical simulations using the MG code to study the physics of MC formation and evolution. We do this by building on the earlier cloud assembly studies of WPFVL16, and combine them with the extensively studied shock-cloud problem. Our reason for this is that WPFVL16 studied clouds that remained quiescent throughout their entire evolution of $\sim 50\,\mathrm{Myrs}$. It is likely that in the ISM such clouds would be impacted by one or more shocks. We therefore increment the complexity in this direction, and study the effects of a single shock impact on a cloud, attempting to understand the relative importance of the TI, gravity and shock impact in MC formation and evolution. We consider an idealised planar shock in the so-called *small cloud regime* (Klein *et al.*, 1994), and a realistic shock due to a supernova explosion in the *large cloud regime*. We introduce these shocks in a "pre-TI" stage when the cloud is still atomic, and a "post-TI" stage when the cloud contains cold dense clumps and warm interclump gas.

In the remainder of this Chapter, we provide the physical background, focusing on the ISM in Section 1.2.1, thermal instability in Section 1.2.2, gravitational collapse in Section 1.2.3, stellar feedback in Section 1.2.4 and a review of shock-cloud studies in Section 1.2.5, where we also define the small, medium and large cloud regimes. Finally in Section 1.3, we provide an overview of the remaining chapters.

1.2 Physical background

1.2.1 The interstellar medium

The interstellar medium (ISM) is everything in the galaxy that is between its stars. This includes material such as interstellar gas, dust, cosmic rays, and dark matter particles, as well as electromagnetic radiation, and magnetic and gravitational fields (Draine, 2011). In a spiral galaxy like the Milky Way, most of the dust and gas can be found confined to a relatively thin gaseous disk (thickness $\sim 500\,\mathrm{pc}$), and it is within this disk that almost all of star formation takes place. By mass (number), the ISM is made up of $\sim 70\,\%$ ($\sim 90\,\%$) hydrogen, $\sim 28\,\%$ ($\sim 9\,\%$) helium and $\sim 1.5\,\%$ ($\sim 0.1\,\%$) heavier elements (so-called metals) (Ferriere, 2001). Within a 20 kpc radius of the centre of the Milky Way, the total mass of hydrogen amounts to approximately $5 \times 10^9\ M_\odot$, of which 23% is in ionized HII, 60% in neutral HI, and 17% in molecular H_2 (Draine, 2011).

1.2.1.1 Phases of the interstellar medium

Variations of the thermodynamic state of the ISM are vast, and can roughly be separated into hot ($T \sim 10^5 - 10^7\,\mathrm{K}$), warm ($T \sim 10^3$ - $10^5\,\mathrm{K}$) and cold ($T \sim 10^1$ - $10^2\,\mathrm{K}$) material (see e.g. Field *et al.*, 1969; McKee & Ostriker, 1977; Wolfire *et al.*, 1995, 2003). The hot material is almost all ionized, with the warm material being a mixture of ionized and neutral, and the cold material being a mixture of neutral and molecular.

A shock-heated, collisionally ionized component observed in UV, X-ray and synchrotron emission is understood to occupy roughly half of the volume of the ISM. With high temperatures of $T \sim 10^6\,\mathrm{K}$ and low densities of $n \sim 0.001\,\mathrm{cm}^{-3}$, this material forms the “hot ionized medium” (HIM). Material surrounding hot and massive O and B type stars has similar densities and temperatures of $T \sim 10^4\,\mathrm{K}$ after being photoionized by the highly energetic UV stellar photons, creating HII regions and extended low-density photoionized regions that make up the Warm Ionized Medium (WIM). HII gas occupies approximately 10 % of the volume of the ISM and has densities and temperatures in the ranges of $0.1-10^4\,\mathrm{cm^{-3}}$ and $10^4-10^6\,\mathrm{K}$ respectively. It is understood to cool, and be observed by optical, fine-structure, free-free and thermal radio emission.

The second largest component of the ISM, observed via HI 21-cm emission and absorption, and optical and UV absorption, occupies roughly 40 % of the volume. This is the warm neutral medium (WNM). Photoelectric (PE) heating from small grains, polycyclic aromatic hydrocarbons (PAHs) and heating due to cosmic rays, balanced by cooling via optical and fine structure line emission, maintain its state approximately at temperatures of $T\sim10^3-10^4\,\mathrm{K}$ and densities $n\sim0.1-1\,\mathrm{cm^{-3}}$. The final cold component occupies less than 1 % of the ISM volume, and is found to exist in an atomic ($T<100\,\mathrm{K}$ and $n>10\,\mathrm{cm^{-3}}$) state known as the cold neutral medium (CNM), and a diffuse molecular ($T\sim50\,\mathrm{K}$, $n\sim100\,\mathrm{cm^{-3}}$) and dense molecular ($T\sim10-50\,\mathrm{K}$, $n\sim10^3-10^{-6}\,\mathrm{cm^{-3}}$) state. Just like the WNM, the energy exchange in the CNM and molecular medium is dominated by PE heating from grains and PAHs, and by fine structure cooling. In the dense molecular medium, line emission from CO and the fine structure of CI also dominate. The HI 21-cm line can be used to observe all 3 states of the cold component, with CO lines and dust FIR emission available in the denser states. A detailed description can be found in table 1.3 in Draine (2011). We show a summary in Table 1.1.

1.2.2 Thermal instability

An ISM phase can be maintained in thermal equilibrium if there is a balance between its energy losses and gains. These can be expressed via a heat loss/gain function for a parcel of material with density ρ and temperature T as

Table 1.1: Extracted summary from table 1.3 in Draine (2011) showing phases of the ISM. Columns shown are the phase, volume filling fraction, typical temperature, typical density and typical methods of observation

Phase	v/v_{tot}	T [K]	n [cm^{-3}]	Observed by
HIM	≈ 0.5	$10^{5.5}$	~ 0.004	• X-ray • UV • Radio synchrotron
HII gas	≈ 0.1	10^4	$\sim 0.3-10^4$	• Optical lines • Thermal radio continuum
Warm HI (WNM)	≈ 0.4	~ 5000	0.6	• HI 21-cm lines • Optical, UV lines
Cool HI (CNM)	≈ 0.01	100	30	• HI 21-cm lines • Optical, UV lines
H_2 gas	≈ 0.001	$10-50$	$100-10^6$	• HI 21-cm lines • CO 2.6-mm lines • Optical, UV lines • Dist FIR emission

$$\mathcal{L}(\rho, T) = \Gamma(\rho, T) - \rho\Lambda(\rho, T) \tag{1.1}$$

(Field, 1965) where Γ and $\rho\Lambda$ are heating and cooling rates per unit mass respectively.

Wherever $\mathcal{L}$ is non-zero, heating and cooling mechanisms act to return the parcel to an equilibrium state to where $\mathcal{L} = 0$, i.e $\Gamma = \rho\Lambda$. When in equilibrium, in all but a narrow range of states in the warm neutral component, a linear perturbation away from equilibrium returns approximately back to its previous state. Within the narrow range however, perturbations grow to non-linear amplitudes, known as the thermal instability (TI). Perturbed away from equilibrium, material here experiences a phase transition, where a fraction of material cools and condenses to form cold clumps, and a fraction heats and "evaporates" to settle into a warmer atomic phase - this results in a two-phase medium of cold and dense regions embedded in a warm diffuse surrounding.

Figure 1.1*a* shows the phase diagram for the warm neutral component as derived by Wolfire *et al.* (1995) for an absorbing column of $N_{\rm w} = 10^{19}\,{\rm cm}^{-2}$. The regions of stability where $d\log(P)/d\log(n) > 0$ have been labelled as A and C, corresponding to the WNM and CNM respectively. The region of instability, where $d\log(P)/d\log(n) < 0$ is marked as B. Above the curve, cooling dominates, and below the curve heating dominates. Material at A (C) perturbed either side of the equilibrium curve returns back to A (C) where the heating and cooling processes act effectively as a thermostat. However removing energy from material at B means material will keep on cooling until it reaches C, and conversely keep on heating until it reaches A if energy is added to B. It can be seen for this curve there exists a range of pressures between $P^{\rm min}/k \simeq 990\,{\rm K\,cm}^{-3}$ and $P^{\rm max}/k \simeq 3600\,{\rm K\,cm}^{-3}$ where both the WNM and CNM can coexist, which corresponds to the two-phase medium that can be generated due to the thermal instability.

The heating and cooling processes in the different ISM phases were already discussed in Section 1.2.1.1, and those responsible for maintaining the neutral atomic phases can be seen in Fig 1.1(b). Correspondingly, the electron fraction $n_{\rm e}/n$ as a function of n is shown in Fig. 1.1(c) and the equilibrium temperature T as a function of n, as well as ionization parameter $G_0 T^{1/2}$ is shown in Fig 1.1(d). We can see from Fig. 1.1(b) that cooling by CII and OI becomes significant at $n \sim 1\,{\rm cm}^{-3}$ with CII steadily increasing with increasing density. It is this behaviour that is responsible for the TI, and the corresponding rapid drop in electron fraction (Fig. 1.1c) and gas temperature (Fig. 1.1d) as material enters the cold neutral phase.

The first to suggest that condensation phenomena in MCs was due to a ther-

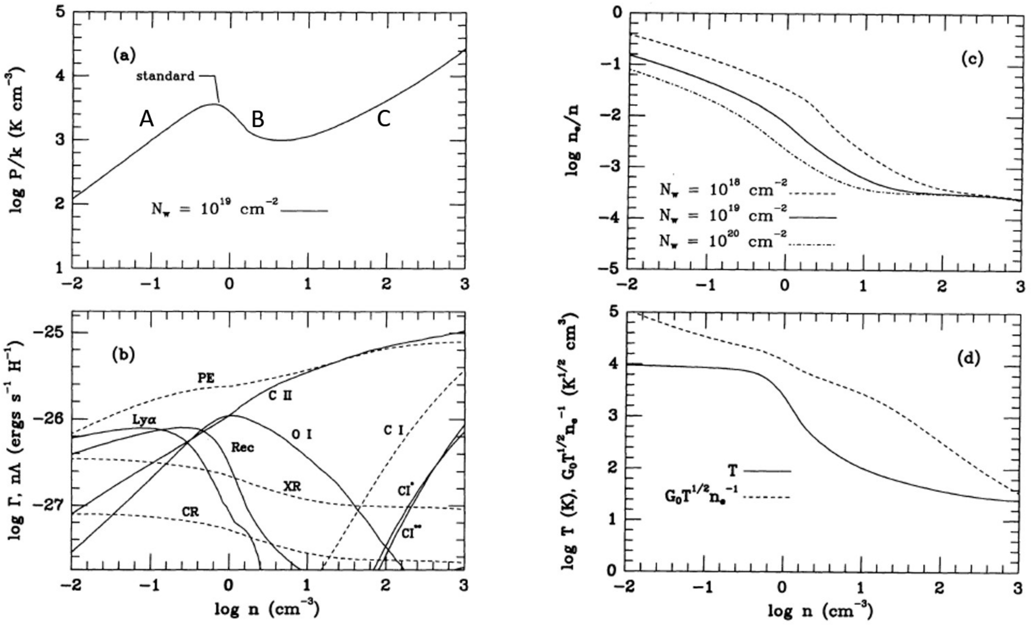

Figure 1.1: Extracted and annotated figure 3 from Wolfire *et al.* (1995) to illustrate the form of the thermal equilibrium in the neutral atomic phases in the ISM.

(a) Thermal pressure P/k vs. hydrogen density n for their "standard model" with absorbing column $N_{\rm w} = 10^{19}\,{\rm cm}^{-2}$. Gas is thermally stable where $d\log(P)/d\log(n) > 0$ (A and C).

(b) Heating and cooling rates per hydrogen nucleus vs. density n for pressure curve shown in panel *a*. Heating rates (*dash*): Photoelectric heating from small grains and PAHs (PE); X-ray (XR); Cosmic ray (CR); photoionization of C (CI). Cooling rates (*solid*): CII fine-structure 370 μm (CII); OI fine-structure (OI); Recombination onto small grains and PAHs (Rec); Lyα plus metastable transitions (Lyα); CI fine-structure 609 μm (CI*); CI fine-structure 370 μm (CI**).

(c) Electron fraction $n_{\rm e}/n$ as a function of hydrogen density n for pressure curve shown in panel *a* (*solid*) for standard $N_{\rm w} = 10^{19}\,{\rm cm}^{-2}$, also shown are curves for $N_{\rm w} = 10^{18}\,{\rm cm}^{-2}$ (*dash*), and for $N_{\rm w} = 10^{20}\,{\rm cm}^{-2}$ (*dash-dot*).

(d) Gas temperature T (*solid*) and ionization parameter $G_0\,T^{1/2}/n_{\rm e}$ (*dash*) as a function of hydrogen density n for pressure curve shown in panel *a*.

mal instability resulting from heating and cooling processes was Parker (1953), and subsequently shown analytically by Field (1965) that density perturbations from infinitesimal density variations can amplify through non-linear growth due to such a phenomenon. As it grows, the TI develops an acoustic mode that is mostly damped in ISM conditions, and an isobaric condensation mode which leads to fragmentation and clumping as long as the sound-crossing time is smaller than the cooling time. Numerous studies have considered the effect of the TI in a diverse range of scenarios, such as flow-driven molecular cloud formation (Lim *et al.*, 2005; Inoue & Inutsuka, 2012), solar prominences (e.g. Xia & Keppens, 2016), star-forming regions (e.g. Kim *et al.*, 2008) and the circumgalactic medium, (e.g. Stern *et al.*, 2016). The efficacy of the TI has also been shown in the context of converting warm diffuse gas into a two-phase medium, driving large scale flows that result in turbulence-like velocity spectra, and generating conditions for local gravitational collapse (Wareing *et al.*, 2019, 2021).

1.2.3 Gravitational collapse

Gravity is critical to the process of molecular cloud and star formation. It is the process of gravitational collapse of molecular material that ultimately forms a star. While gravity acts to generate a force that causes collapse, many forces such as that resulting from thermal, ram or magnetic pressures act to stabilise, and oppose collapse. A powerful theorem to describe the behaviour of material subject to such forces is the Virial theorem (e.g. McKee & Zweibel, 1992; Krumholz, 2015).

The Virial theorem can be used to describe the stability of a system by considering the system's second derivative of its moment of inertia, giving a quantity that tells us the rate of change of the system's expansion or contraction. If this system is a molecular cloud, assumptions can be made regarding its morphology, state and governing physics, to give the Virial parameter often written as

$$\alpha_{\mathrm{vir}} = \frac{2T}{|W|} \tag{1.2}$$

where T is the total kinetic and thermal energies of the cloud, and $|W|$ is the magnitude of the gravitational potential energy of the cloud. Thus, $\alpha_{\mathrm{vir}} > 1$ corresponds to an expanding cloud, and $\alpha_{\mathrm{vir}} < 1$ corresponds to a collapsing cloud.

The simplest system to consider is an infinite, isothermal medium initially at rest, subject to forces due to self-gravity and pressure only, as was analysed formally by Jeans in 1902 (Jeans, 1902). Jeans considers the linear stability of the system of equations for conservation of mass and momentum, and the Poisson equation for gravity. Such a procedure results in a dispersion relation of the form

$$\omega^2 = c_{\mathrm{s}}^2 k^2 - 4\pi G \rho_0, \tag{1.3}$$

where ω is the temporal frequency, k the spatial frequency, c_{s} the sound speed of the medium, G the gravitational constant and ρ_0 the unperturbed volume density.

A dispersion relation gives a relationship of how a spatial frequency relates to the temporal frequency of a wave, of the form $e^{i(kx-\omega t)}$ in this case. By considering the case for $\omega = 0$ in equation (1.3), what is known as the Jeans length can be defined, which is the length-scale that sets the threshold of stability and is expressed as

$$\lambda_{\mathrm{J}} = \frac{2\pi}{k_{\mathrm{J}}} = \sqrt{\frac{\pi c_{\mathrm{s}}^2}{G\rho_0}}. \tag{1.4}$$

Perturbations on the cloud state with sizes $\lambda > \lambda_{\mathrm{J}}$ trigger the instability. An associated Jeans mass can also be defined as $M_\mathrm{J} = \rho\lambda_\mathrm{J}^3/8$.[1] For typical GMCs with $c_\mathrm{s} = 0.2\,\mathrm{km\,s^{-1}}$ and $\rho_0 = 100 m_\mathrm{H}\,\mathrm{cm^{-3}}$, we obtain $\lambda_\mathrm{J} = 3.4\,\mathrm{pc}$. As GMCs are larger than this size, they cannot be stabilised by gas pressure against collapse.

Equation (1.3) can be considered to be defined in terms of a sound-crossing timescale t_sound and a gravitational free-fall timescale t_ff as $\omega^2 \sim 1/t_\mathrm{sound}^2 - 1/t_\mathrm{ff}^2$, where $\mathrm{t_{sound}} \sim \lambda/c_\mathrm{s}$ and $t_\mathrm{ff} \sim 1/\sqrt{G\rho_0}$. This makes it possible to derive how fast we should expect gravitational instabilities to grow if $t_\mathrm{sound} \gg t_\mathrm{ff}$. In the literature, the value derived for a pressureless sphere is often quoted, namely

$$t_\mathrm{ff} = \sqrt{\frac{3\pi}{32G\rho_0}}. \tag{1.5}$$

This free-fall time is the characteristic timescale required for a medium with negligible pressure support to collapse and form a star.

1.2.4 Stellar feedback

Once stars form, their radiation fields, and mechanical output due to winds and supernovae (SNe) from massive stars destroy and disperse molecular material. This eventually ends the star formation process, however further star formation may be triggered also (e.g. Koenig *et al.*, 2011). The most massive O and B stars are by far the most dominant, in spite of representing a minor fraction of the stellar population and the shortest lifetimes in stellar clusters (e.g. Abbott, 1982; Kroupa, 2001).

---

[1] M_J can be somewhat ambiguous, and can refer both to a sphere with a Jeans length in radius, diameter, or a theoretical cube with face lengths corresponding to the Jeans length. In this case, we have followed the definition in Krumholz (2015) and consider a cube whose edges have lengths of $\lambda_\mathrm{J}/2$. In any case, different definitions simply cause a difference in the coefficient, and not how this quantity scales.

1.2.4.1 Radiation

Stellar radiation, especially that due to UV photons from O and B stars, can have a significant impact on the surrounding environment. Firstly, far-ultraviolet photons ($6 < \mathrm{h}\nu < 13.6\,\mathrm{eV}$) are responsible for dissociating molecules such as H_2, CO, OH, O_2, and H_2O, to name a few, into their constituent atomic parts in what is known as photodissociation regions (e.g. Hollenbach & Tielens, 1999). Secondly, photons with $\mathrm{h}\nu > 13.6\,\mathrm{eV}$ ionize the immediate vicinity of O and B stars, creating HII regions and ionizing more remote diffuse areas, together creating the ionized component of the ISM (see Section 1.2.1.1). In neutral regions, elements such as C, Mg, Si, and S are ionized, whose ionization potential lies below the hydrogen threshold of 13.6 eV, also contributing to the warm and hot ionized components. Ionized interstellar regions are heated to temperatures of $\simeq 8000\,\mathrm{K}$ via the liberated photoelectrons, resulting in high thermal pressures and thus the expansion of HII regions (Pittard *et al.*, 2021b).

1.2.4.2 Winds

All massive O and B stars have winds driven by radiation, resulting in a mass loss rate $\dot{M}$ of the star (Kudritzki & Puls, 2000). The winds can be accelerated to terminal velocities of up to $v_\infty \sim 1000\,\mathrm{km\,s^{-1}}$, and have a significant impact on their surroundings. In a uniform medium, the wind from a massive star blows a cavity of hot gas which compresses and sweeps up interstellar material into a rapidly expanding wind-blown bubble. The swept up material is thermalised due to the shock wave that forms at the interface of the wind and surroundings, and is separated by a contact discontinuity from wind material that has been thermalised by the reverse shock that forms as the freely expanding wind is slowed down by the swept up ISM (Castor *et al.*, 1975; Weaver *et al.*, 1977; Pittard *et al.*, 2021a). The swept up gas typically cools quickly, so that the bubble consists of a cold dense shell surrounding a hot ($T \sim 10^7$ K) interior.

A diverse range of scenarios can affect the impact of a wind. For example, individual stellar winds may combine, collectively creating superbubbles and cluster winds (Chevalier & Clegg, 1985; Stevens & Hartwell, 2003; Franeck *et al.*, 2022). The density distribution and gas motions arising from large scale magnetic fields can impact the shape of the bubble (Wareing *et al.*, 2016b; Wareing *et al.*, 2018). Harper-Clark & Murray (2009) postulate that if the wind couples strongly to its surroundings, inhomogeneities in the external medium can cause gaps in the swept-up shell. In such a case, high-pressure gas in the bubble interior can leak out, and cause the bubble to have a lesser impact on its surroundings and lose its characteristic identity. If this coupling is weak however, winds have been shown to carve out low-density channels within their environment and still create wind blown bubbles with hot diffuse interiors. Behaviour like this can remove interclump material that acts as a barrier between the stars and the wider ISM, and open up pathways for the escape of material and energy released by explosions due to supernovae (Rogers & Pittard, 2013; Wareing *et al.*, 2016b, 2017).

1.2.4.3 Supernovae

Supernovae (SNe) have long been understood to be key to the evolution of the ISM (McKee & Ostriker, 1977), dominating the creation of the hot ISM phase and shaping its the large scale multiphase structure (e.g. Hill *et al.*, 2012; Hennebelle & Iffrig, 2014; Walch *et al.*, 2015). In addition, SNe are understood to be key in driving turbulence in diffuse (e.g. Mac Low & Klessen, 2004a) and molecular gas (e.g. Padoan *et al.*, 2016), regulating the star formation rates (e.g. Kim *et al.*, 2011, 2013; Shetty & Ostriker, 2012), and driving galactic winds (Cooper *et al.*, 2008, 2009; Schneider & Robertson, 2017).

SNe typically come in two types, type-I and type-II. Type-Ia SNe usually arise in binary systems in which one star is a white dwarf accreting from a companion. Upon accumulating approximately a Chandrasekhar mass of 1.44 $M_\odot$, the star undergoes thermonuclear instability which ignites the heavy elements in the core such as carbon and helium, and releases $\sim 10^{51}$ erg of kinetic energy into the surroundings (Woosley & Weaver, 1986). A similar amount of energy is released via type-Ib/Ic/II SNe, however their driving mechanism is different, which is due to gravitational collapse of the stellar core, and only stars with masses $\gtrsim 8\,M_\odot$ in their main sequence have the potential to explode in this way. A SN explosion results in a supernova remnant (SNR) expanding into the ISM.

The spherically symmetric expansion of a SNR into a uniform medium has been extensively studied and is understood to evolve through several idealised stages (Woltjer, 1972; Draine, 2011). The SN explosion ejects material into the ISM, sweeping up the surroundings via a forward shock whilst a reverse shock propagates back towards the blast origin. The ejecta expand freely until the swept up ISM mass is roughly on the order of the ejecta mass, typically $\sim 1-10$ $M_\odot$. When the swept up mass is greater than the ejecta mass and the reverse shock has heated the remnant interior to high temperatures, the remnant follows the well-known Sedov-Taylor (ST) adiabatic stage analysed by Sedov (1959) and Taylor (1950). When radiative cooling becomes important, a dense shell is formed at the outer edges of the SNR and the evolution enters a pressure-driven snowplough (PDS) stage. Once the interior pressure drops below the ambient pressure surrounding the remnant, the evolution can enter a momentum-conserving snowplough (MCS) stage. Theoretically, the remnant can be considered to have stalled and mixed with the ISM approximately when the forward shock velocity drops below the sound speed of the surroundings.

In simple analytic models, the position of the forward shock can be approximated to evolve as $R_{\rm SN} \propto t^{\eta}$ (e.g. Cioffi *et al.*, 1988; Draine, 2011), with the power law exponent distinguishing the different stages: $\eta = 1$ in the free expansion stage, 2/5 in the ST stage, 2/7 in the PDS stage and 1/4 in the MCS stage. In reality, SNRs are not likely to expand into a uniform medium, and instead come in contact with inhomogeneities in their surroundings.

1.2.5 The shock-cloud problem

The hot and high velocity flows that result from stellar feedback have been observed to interact with regions of cooler and denser material in the ISM, including molecular clouds, clumps and cores (e.g. Koo *et al.*, 2001; Westmoquette *et al.*, 2010). Objects such as the B59 filament in the Pipe nebula (Peretto *et al.*, 2012) and the MC complexes in the Cygnus X (Schneider *et al.*, 2006) region are well understood to be sites where this is occurring. Such interactions can significantly alter the characteristics of the feedback mechanism, the colder object embedded in the flow, and the wider ISM. As the likelihood of such interactions is very high, since the 1970s it is a problem that has received a large amount of attention, both within and outside of astrophysics. An idealisation of such interactions can be made by considering a planar shock impacting a perfectly spherical cloud, i.e. a shock-cloud interaction, also known as shock-bubble interaction in contexts outside of astrophysics.

An extensive 2D numerical study of an adiabatic shock hitting a spherical cloud was conducted by Klein *et al.* (1994, hereafter KMC94), who examined the effects of varying the shock Mach number M ($M = v_{\rm s}/c_{\rm s}$ where $v_{\rm s}$ is the shock velocity and $c_{\rm s}$ is the pre-shock sound speed), and the density contrast χ ($\chi = \rho_{\rm cl}/\rho_{\rm amb}$ where $\rho_{\rm cl}$ is the cloud density and $\rho_{\rm amb}$ is the ambient density). Many interesting gas dynamical effects were presented. The shock is seen to sweep around the cloud and reconnect at the opposite side to which the impact occurred, which creates a powerful pressure jump and generates a series of reflections and rarefactions of the shock. After the external shock passes, the cloud becomes embedded in higher pressure surroundings, whilst a shock is propagating into the cloud from all sides that is strongest at the front and back. The internal shock propagates towards the centre of the cloud, and is subsequently seen to reconnect there. The cloud then itself becomes over-pressured, as the reconnected shock generates additional internal reflections, which causes the cloud to expand and reverberate. During this time, the cloud is subject to Kelvin-Helmholtz, Rayleigh-Taylor and Richtmeyer-Meshkov instabilities. Note that if the transmitted shock is radiative, the Vishniac non-linear thin shell instability can develop (Vishniac, 1983, 1994).

Many 2D and 3D studies have been conducted since, and have considered effects due to radiative cooling (e.g. Fragile *et al.*, 2004; Yirak *et al.*, 2010), magnetic fields (e.g. Mac Low *et al.*, 1994; Fragile *et al.*, 2005), sub-grid turbulence (e.g. Pittard *et al.*, 2009, 2010; Pittard & Parkin, 2016a), different cloud profiles (e.g. Nakamura *et al.*, 2006) and shapes (e.g. Pittard & Goldsmith, 2016; Goldsmith & Pittard, 2016, 2020), thermal instability (e.g. Van Loo *et al.*, 2007; Inoue & Inutsuka, 2009; Heitsch *et al.*, 2009; Van Loo *et al.*, 2010; Aota *et al.*, 2013; Inoue & Omukai, 2015; Kupilas *et al.*, 2021), and multiple clouds (Poludnenko *et al.*, 2002; Alūzas *et al.*, 2012, 2014). Additional simulation work has been done to study the behaviour of clouds accelerated by galactic winds (Scannapieco & Brüggen, 2015; Banda-Barragán *et al.*, 2019), finite thickness supernova blast waves (Leao *et al.*, 2009; Obergaulinger *et al.*, 2014) and dense shells driven by hot over pressured gas (Pittard, 2011). For more extensive reviews of the literature of shock-cloud interactions see Pittard & Parkin (2016b) and Banda-Barragán *et al.* (2019) who include tables of numerical studies conducted in the past 3 decades, Jiang *et al.* (2010) who compile a list of known galactic supernova remnants known to be interacting with molecular clouds, and Ranjan *et al.* (2011) who review shock-bubble interactions in a non-astrophysical context, and discuss the relevant fluid dynamics.

1.2.5.1 Timescales

KMC94 describe their models in terms of a number of timescales, with a subset of these being adopted by almost all shock-cloud studies in the literature since. The most basic of these is the shock-crossing timescale

$$t_{\rm sc} = \frac{2r_{\rm cl}}{v_{\rm s}}, \tag{1.6}$$

which simply describes the time taken for the external blast wave shock to sweep over the cloud. The second of these is the cloud-crushing timescale

$$t_{\rm cc} = \frac{\chi^{1/2} r_{\rm cl}}{v_{\rm s}}, \tag{1.7}$$

which describes the time taken for the transmitted cloud shock with velocity

$$v_{\rm s,cl} = \frac{v_{\rm s}}{\chi^{1/2}} \tag{1.8}$$

to traverse the cloud radius $r_{\rm cl}$ and crush the cloud. Note that if the shock is strong ($M \gg 1$), the ambient post-shock pressure is approximately $\rho_{\rm amb} v_{\rm s}^2$ and the cloud post-shock pressure is approximately $\rho_{\rm cl} v_{\rm s,cl}^2$. Assuming these are comparable, equating them gives result (1.8), with equations (1.6) and (1.7) then being the basic timescales governing the evolution of the shocked cloud.

After the blast wave passes over the cloud, the cloud is accelerated by the shocked ambient medium until both the cloud and the ambient medium are co-moving, i.e. the relative velocity $v_{\rm rel} = |\overline{v}_{\rm cl} - v_{\rm ps,amb}| = 0$, where $\overline{v}_{\rm cl}$ is the average cloud velocity, and $v_{\rm ps,amb}$ is the post-shock ambient velocity. It is possible therefore to derive a theoretical drag timescale $t_{\rm drag}$ on which one would expect to see this happen, which KMC94 quote as

$$t_{\rm drag} = \frac{\chi^{1/2} t_{\rm cc}}{C_{\rm D}} \tag{1.9}$$

where $C_{\rm D} \sim 1$ is the drag coefficient that comes from the equation of motion that considers the response of the cloud to the ram pressure of the external flow in the strong shock limit $(M \gg 1)$. In reality, this timescale is of the order of a few cloud-crushing timescales.

If where the shock impacts the cloud is considered the front of the cloud, then the Kelvin-Helmholtz instability that arises due to velocity shear, develops on the sides. For perturbation of wavenumber k parallel to the relative velocity $v_{\rm rel}$ between the cloud and the intercloud medium, the Kelvin-Helmholtz growth time is comparable to the cloud-crushing timescale as

$$\frac{t_{\rm KH}}{t_{\rm cc}} = \frac{v_{\rm s}/v_{\rm rel}}{k r_{\rm cl}}. \tag{1.10}$$

(Chandrasekhar, 1961). The Rayleigh-Taylor instability, which arises due to rapid acceleration at the front of the cloud also has a growth time of the order of $t_{\rm cc}$, and can be expressed as

$$\frac{t_{\rm RT}}{t_{\rm cc}} = \frac{1}{(k r_{\rm cl})^{1/2}}. \tag{1.11}$$

The shortest wavelengths grow the fastest, but the longer wavelengths, where $k r_{\rm cl} \sim 1$, are more disruptive. These results suggest that the cloud will be destroyed in a time comparable to $t_{\rm cc}$ (Chandrasekhar, 1961).

An additional timescale of interest is the cooling time $t_{\rm cool}$ which can be expressed as

$$t_{\rm cool} = \frac{E - E_{\rm eq}}{\dot{E}}, \tag{1.12}$$

where E is the thermal energy of the gas, $E_{\rm eq}$ is the energy at thermal equilibrium in the ISM (i.e. for gas that lies along the curve in Fig. 1.1a), and $\dot{E}$ is the energy loss rate, in our case given by the particular form of equation (1.1).

The final timescale of interest is the pressure variation timescale $t_{\rm P}$, which describes a characteristic timescale on which we expect there to be some significant changes to the post-shock pressure, depending on the source of the shock, e.g. driven by blast waves produced by explosions, or winds emanating from point sources. Discussed in KMC94, and formally analysed in McKee *et al.* (1987) in their theory of weakly time-dependent interstellar shocks, for a Sedov-Taylor blast wave, $t_{\rm p}$ is found to approximate well as

$$t_{\rm p} \simeq 0.1 \frac{R_{\rm c}}{v_{\rm s}}, \tag{1.13}$$

where $R_{\rm c}$ is the distance of the nearest part of the surface of the cloud from the blast epicentre, and $v_{\rm s} = dR_{\rm s}/dt$ is the velocity of the blast wave at radius $R_{\rm c}$.

1.2.5.2 Small, medium and large clouds

The condition that enables a physical set-up where an incoming shock onto a cloud has no curvature in its structure and the shock-driving pressure is time independent is known as the *small cloud approximation* (KMC94). Implications of such an approximation can be understood in terms of the time-dependence of the shock-driving pressure, as characterised by $t_{\rm P}$ (equation 1.13), and its comparison with $t_{\rm sc}$ (equation 1.6) and $t_{\rm cc}$ (equation 1.7). Comparison of these timescales allows the definition of the *small cloud regime*, as well as the *medium* and *large cloud regimes* (see e.g. KMC94 and references therein).

The *small cloud regime* thus requires the cloud to be sufficiently small (or blast to be sufficiently large) for t_{p} to satisfy $t_{\mathrm{cc}} \ll t_{\mathrm{p}}$, thus by extension for r_{cl} to satisfy

$$r_{\mathrm{cl}} \ll 0.1\frac{R_{\mathrm{c}}}{\chi^{1/2}}. \tag{1.14}$$

The *medium cloud regime* requires the cloud to be a size such that the blast wave does not change significantly as it sweeps over the cloud, but does change as the cloud is crushed. This requires t_{p} to satisfy $t_{\mathrm{cc}} \gtrsim t_{\mathrm{p}} \gtrsim t_{\mathrm{sc}}$, and by extension for r_{cl} to satisfy

$$0.1\frac{R_{\mathrm{c}}}{\chi^{1/2}} \lesssim r_{\mathrm{cl}} \lesssim 0.05R_{\mathrm{c}}. \tag{1.15}$$

Finally, the *large cloud regime* requires that the cloud is large enough (or blast small enough) that the blast wave ages significantly as it sweeps over the cloud, resulting in vastly weaker compression at the rear of the cloud than the front, such that t_{p} satisfies $t_{\mathrm{sc}} > t_{\mathrm{p}}$ and r_{cl} satisfies

$$r_{\mathrm{cl}} > 0.05R_{\mathrm{c}}. \tag{1.16}$$

1.3 Overview of the Thesis

As mentioned, in this Thesis we study the formation and evolution of molecular clouds out of an atomic interstellar medium due to the thermal instability (TI), gravity, and a shock. We take the opportunity that the role of the TI was extensively studied by WPFVL16 in the context of molecular cloud formation, and combine their work with the extensively studied and well understood shock-cloud problem.

In Chapter 2, we first present the numerical methods used to simulate and study the problem. The interaction is then studied in two physical regimes, and each regime considers two scenarios: one where the shock is introduced whilst the initial cloud is still atomic, and one where a shock is introduced when the cloud has been disturbed by the TI and formed a two-phase medium of cold and dense molecular clumps embedded in warm interclump gas. In the first study (Chapter 3), the shock is approximated to be planar and time independent, in a tsunami-like manner, and impacts a spherical $17\,000\,M_{\odot}$, $r_{\rm cl}=50\,{\rm pc}$ cloud. Given the properties of the shock, we can assume that its distance from the nearest edge of the cloud is $R_{\rm c}=\infty$. Formally therefore, according to equation (1.14) this set-up falls in the *small cloud regime.* In the second study (Chapter 4), the idealised shock is replaced by a realistic supernova event that is also introduced in scenarios when the cloud is still atomic and when the cloud has formed a two-phase medium due to the TI. The distance of the blast origin from the nearest cloud edge is $R_{\rm c}\approx 50\,{\rm pc}$ in the scenario when the cloud is atomic, and $R_{\rm c}\approx 70\,{\rm pc}$ when the cloud has developed a two-phase medium. According to equation (1.16) therefore, this places both of these scenarios in the *large cloud regime.*

In Chapter 5, we perform a Fourier analysis of all of the models studied and derive power spectra for velocity, density and density logarithm. We take advantage of the fact that the physics of the interactions was understood in the previous two chapters, and make connections between the behaviour of the spectra to the behaviour of the clouds. We specifically look for any turbulence-like signatures in the spectra.

Finally, in Chapter 6 we summarise the main results and present our concluding remarks.

Chapter 2

Methods

2.1 Introduction

This chapter provides an overview of the methods used to study the problem in this Thesis. An introduction to gas dynamics is presented first, followed by computational details of the MG code used in this work.

2.2 Gas Dynamics

If in a system of particles the mean free path for particle collisions is significantly smaller than the size over which bulk variations occur, then the system can be modelled as a continuous medium. An equation of state then determines whether the medium is a solid, liquid, gas, or anything else. An example is the model of the ideal gas. This approximation asserts that particles collide often and elastically, resulting in Maxwellian velocity distributions. The gas properties can then be described by average thermodynamic quantities such as pressure, temperature, density and mean velocity, with changes to these quantities governed by mass, momentum and energy conservation.

If all the quantities describing the gas state are allowed to vary in space and time, then in a 3D Cartesian geometry, an ideal, inviscid, non-conducting compressible fluid obeys the Euler equations of gas dynamics:

$$\frac{\partial \mathbf{U}}{\partial t} + \frac{\partial \mathbf{F}}{\partial x} + \frac{\partial \mathbf{G}}{\partial y} + \frac{\partial \mathbf{H}}{\partial z} = 0. \tag{2.1}$$

Here,

$$\mathbf{U} = (\rho, \rho u, \rho v, \rho w, E)^{\mathrm{T}} \tag{2.2}$$

is vector of parameters (Roe, 1981) giving the conserved variables of mass density ($\mathbf{U}_1$), x–z components of momentum density ($\mathbf{U}_{2-4}$) and total energy density (thermal + kinetic) ($\mathbf{U}_5$) given by

$$E = \frac{p}{(\gamma - 1)} + \frac{1}{2}\rho\left(u^2 + v^2 + w^2\right). \tag{2.3}$$

The subscripts refer to the matrix entry in (2.2) in which T in denotes the transpose. In equation (2.3), γ is the ratio for specific heats and is chosen to be fixed at 5/3 corresponding to a monoatomic gas. Note that this is also appropriate for molecules at low temperatures as they cannot access their rotational and vibrational degrees of freedom, effectively acting as monoatomic for the purpose of the dynamics (see Krumholz *et al.*, 2007).

$$\mathbf{F} = \begin{pmatrix} \rho u \\ \rho u^2 + p \\ \rho uv \\ \rho uw \\ u(E+p) \end{pmatrix}, \ \mathbf{G} = \begin{pmatrix} \rho v \\ \rho vu \\ \rho v^2 + p \\ \rho vw \\ v(E+p) \end{pmatrix}, \ \mathbf{H} = \begin{pmatrix} \rho w \\ \rho wu \\ \rho wv \\ \rho w^2 + p \\ w(E+p) \end{pmatrix} \tag{2.4}$$

are then vectors of the fluxes of the quantities in (2.2).

The equations are very amenable for extension to include more complex physics, as has been done in this project with the inclusion of a source term, modifying (2.1) as

$$\frac{\partial \mathbf{U}}{\partial t} + \frac{\partial \mathbf{F}}{\partial x} + \frac{\partial \mathbf{G}}{\partial y} + \frac{\partial \mathbf{H}}{\partial z} = \mathbf{S} \; . \tag{2.5}$$

Here, the mass source $\mathbf{S}_1$ is zero, $\mathbf{S}_{2\text{-}4}$ corresponds to x–z components of a momentum source due to self-gravity, and $\mathbf{S}_5$ is an energy source approximating radiative heating/cooling processes. The work done by the gravitational force is also accounted for in $\mathbf{S}_5$. We will discuss the sources in more detail in Section 2.4. Extensions to these equations can also be done to include magnetic fields, dust (multi-fluid), and relativist physics, to name a few, however these are beyond the scope of this work.

Physically, the equations state that any rate of change in the density of a conserved quantity at any location is due to a net flux and source at that location.

This can also be expressed in integral form. Consider (2.1) in compact form

$$\frac{\partial \overline{\mathbf{U}}}{\partial t} + \nabla \cdot \overline{\mathbf{F}} = \overline{\mathbf{S}} \tag{2.6}$$

where

$$\overline{\mathbf{U}} = \begin{pmatrix} \rho \\ \rho \mathbf{u} \\ E \end{pmatrix} \quad \text{and} \quad \overline{\mathbf{F}} = \begin{pmatrix} \rho \mathbf{u} \\ \rho \mathbf{u} \otimes \mathbf{u} + p\mathbb{I} \\ \mathbf{u}(E+p) \end{pmatrix} \; . \tag{2.7}$$

Here, $\overline{\mathbf{U}}$ is a more compact version of (2.2) and $\overline{\mathbf{F}} = \mathbf{F}\hat{x} + \mathbf{G}\hat{y} + \mathbf{H}\hat{z}$ is a compact version of (2.4). $\overline{\mathbf{S}}$ is compacted to match the number of parameter vectors in $\overline{\mathbf{U}}$ and $\overline{\mathbf{F}}$. For an arbitrary fixed volume V, (2.6) can be integrated as

$$\int_V \left(\frac{\partial \overline{\mathbf{U}}}{\partial t} + \nabla \cdot \overline{\mathbf{F}} - \overline{\mathbf{S}} \right) \mathrm{d}V = 0 \; . \tag{2.8}$$

Evaluating each term individually, the first term becomes

$$\int_V \frac{\partial \overline{\mathbf{U}}}{\partial t} \mathrm{d}V = \frac{\partial}{\partial t} \int_V \overline{\mathbf{U}} \mathrm{d}V = \frac{\partial}{\partial t} \int_V \left(\begin{array}{c} \rho \\ \rho \mathbf{u} \\ E \end{array} \right) dV \equiv \frac{\partial}{\partial t} \left(\begin{array}{c} m \\ m\mathbf{u} \\ E_{\mathrm{tot}} \end{array} \right) = \frac{\partial \mathbf{Q}}{\partial t} , \quad (2.9)$$

which describes the time rate of change of total of the conserved quantities $\mathbf{Q}$.

Using the divergence theorem, the second term in (2.8) becomes

$$\int_V \left(\nabla \cdot \overline{\mathbf{F}} \right) \mathrm{d}V = \int_A \overline{\mathbf{F}} \cdot \mathrm{d}\mathbf{A} , \quad (2.10)$$

where $\mathrm{d}\mathbf{A}$ is the vector area element of the surface bounding V.
Keeping the source term as it is, (2.9) and (2.10) together state that

$$\int_V \frac{\partial \overline{\mathbf{U}}}{\partial t} \mathrm{d}V = - \int_A \overline{\mathbf{F}} \cdot \mathrm{d}\mathbf{A} + \int_V \overline{\mathbf{S}} \mathrm{d}V \equiv \frac{\partial \mathbf{Q}}{\partial t} , \quad (2.11)$$

meaning that the time rate of change of the conserved quantities in the volume is given by the flux through the surface bounding the volume, with any additional changes arising due to sources or sinks in the volume.

The equations above describe motion in a fixed coordinate system. Analogous Lagrangian equations describing the motion in a frame moving with the flow exist, however we focus the Eulerian formulation due to its compatibility with simulating fluid flows using the finite-volume method employed in MG. Note that detailed derivations of both the Eulerian and Lagrangian equations can be found in almost any Fluid Dynamics textbook. For the Euler equations and the associated numerical methods, we recommend Toro (2009).

2.2.1 Rankine-Hugoniot jump conditions

The Euler equations admit a variety of behaviour. Of interest is when the local velocity is greater than the sound speed ahead of the flow, resulting in a shock wave. It is possible to relate the state of the fluid on either side of the shock by a set of equations known as the Rankine-Hugoniot jump conditions (e.g. Courant & Friedrichs, 1999). In 1D these read as

$$\begin{aligned} \rho_1 u_1 &= \rho_2 u_2 \ , \\ p_1 + \rho_1 u_1^2 &= p_2 + \rho_2 u_2^2 \ , \\ u_1^2 + \frac{2}{\gamma - 1} c_1^2 &= u_2^2 + \frac{2}{\gamma - 1} c_2^2 \ , \end{aligned} \tag{2.12}$$

where c^2 is the square of the adiabatic sound speed $\partial \mathrm{p}/\partial \rho = \gamma \mathrm{P}/\rho$. Note that the above apply to a reference frame moving with the shock. If the shock is moving with a velocity $\mathbf{v}_s$ relative to the Eulerian frame, the appropriate transformation is made by $\mathbf{u}^{'} = \mathbf{u} - \mathbf{v}_s$. The relations express the conservation of mass, momentum and energy.

It is possible to express these relations in terms of the upstream Mach number

$$M_1 \equiv \frac{u_1}{c_1} = \left(\frac{\rho_1 u_1^2}{\gamma P_1} \right)^{1/2} \tag{2.13}$$

to produce

$$\begin{aligned} \frac{\rho_2}{\rho_1} &= \frac{u_1}{u_2} = \frac{(\gamma + 1) M_1^2}{(\gamma - 1) M_1^2 + 2} \\ \frac{P_2}{P_1} &= \frac{2\gamma M_1^2 - (\gamma - 1)}{\gamma + 1} \\ \frac{T_2}{T_1} &= \frac{[(\gamma - 1) M_1^2 + 2][2\gamma M_1^2 - (\gamma - 1)]}{(\gamma + 1)^2 M_1^2} . \end{aligned} \tag{2.14}$$

For a strong adiabatic shock with $\gamma = 5/3$ and $M_1 \gg 1$, the limiting behaviour of (2.14) can be derived, yielding

$$\begin{aligned} \frac{\rho_2}{\rho_1} &= \frac{u_1}{u_2} = 4 \\ P_2 &= \frac{3}{4}\rho_1 u_1^2 \\ T_2 &= \frac{3}{16}\frac{\mu m}{k}u_1^2. \end{aligned} \tag{2.15}$$

Here μ is the mean molecular weight, and m is the particle mass. We see that for an adiabatic shock, the pre-shock density can increase across the shock maximum by a factor ~ 4, whilst the post-shock pressure and temperature have no theoretical limit. Note that the thermal pressure behind the shock is approximately the ram pressure of the upstream gas.

If radiative cooling becomes efficient, isothermal shocks can emerge where

$$\begin{aligned} \frac{\rho_2}{\rho_1} &= \frac{u_1}{u_2} = \left(\frac{u_1}{c_T}\right)^2 = M_T^2 \\ T_2 &= T_1. \end{aligned} \tag{2.16}$$

Here, $c_T = (kT/\mu m)^{1/2}$ is the isothermal sound speed. In theory therefore, the compression of gas in an isothermal shock can result in arbitrarily high densities.

2.3 MG numerical scheme

In order to obtain numerical solutions to the Euler equations, appropriate discretisation and integration procedures must be followed, where both the differential and integral forms of the equations can be used. If a Finite-Difference (FD) method is used, the functions that describe the fluid spatially are evaluated at individual locations, and the time integration algorithms are constructed using the differential form of the Euler equations. When derivatives are large or undefined, as is the case for shocks, such a method will break down. This is not the case with a Finite-Volume (FV) method where the time integration algorithm is constructed from the integral form of the Euler equations. Here, a grid is defined such that a discrete cell with centre i, j, k occupies the region

$$\begin{aligned}(i-1/2)\Delta x \leq x \leq (i+1/2)\Delta x\\(j-1/2)\Delta y \leq y \leq (j+1/2)\Delta y\\(k-1/2)\Delta z \leq z \leq (k+1/2)\Delta z\end{aligned} \tag{2.17}$$

where $\Delta x = \Delta y = \Delta z$ is the grid spacing in all spatial dimensions. A discrete timestep of Δt is then also adopted. Equation (2.6) is integrated and subsequently averaged over a cell volume and timestep as

$$\frac{1}{V\Delta t}\int_{dt}\int_{V}\frac{\partial\overline{\mathbf{U}}}{\partial t}\mathrm{d}V\mathrm{d}t = -\frac{1}{V\Delta t}\int_{dt}\int_{A}\overline{\mathbf{F}}\cdot\mathrm{d}\mathbf{A}\mathrm{d}t + \frac{1}{V\Delta t}\int_{dt}\int_{V}\overline{\mathbf{S}}\mathrm{d}V\mathrm{d}t\ , \tag{2.18}$$

where $\Delta V = \Delta x\Delta y\Delta z$, and the substitution (2.10) has been made for the divergence term. Supposing we know the solution at the discrete time coordinate $\mathrm{t} = \mathrm{t}^{n}$ and we wish to calculate it at $\mathrm{t} = \mathrm{t}^{n+1}$, (2.18) is integrated over cell i, j, k and over $\Delta\mathrm{t}$ = $\mathrm{t} = \mathrm{t}^{n+1}$ - t^{n} to get the following expression for the updated solution

$$\begin{aligned}\mathbf{U}_{ijk}^{n+1} &=\\ \mathbf{U}_{ijk}^{n} &- \frac{\Delta t}{\Delta x}\left(\mathbf{F}_{i+\frac{1}{2}jk}^{n} - \mathbf{F}_{i-\frac{1}{2}jk}^{n}\right)\\ &- \frac{\Delta t}{\Delta y}\left(\mathbf{G}_{ij+\frac{1}{2}k}^{n} - \mathbf{G}_{ij-\frac{1}{2}k}^{n}\right)\\ &- \frac{\Delta t}{\Delta z}\left(\mathbf{H}_{ijk+\frac{1}{2}}^{n} - \mathbf{H}_{ijk-\frac{1}{2}}^{n}\right)\\ &+ \Delta t\mathbf{S}_{ijk}^{n}\ ,\end{aligned} \tag{2.19}$$

were we drop the over-line as we have expanded the compacted terms. Here

$$\mathbf{U}_{ijk}^{n} = \frac{1}{V}\int_{V}\mathbf{U}\left(x, y, z, t^{n}\right)\mathrm{d}V \tag{2.20}$$

is the mean value of $\mathbf{U}$ in cell i, j, k at t^{n} and

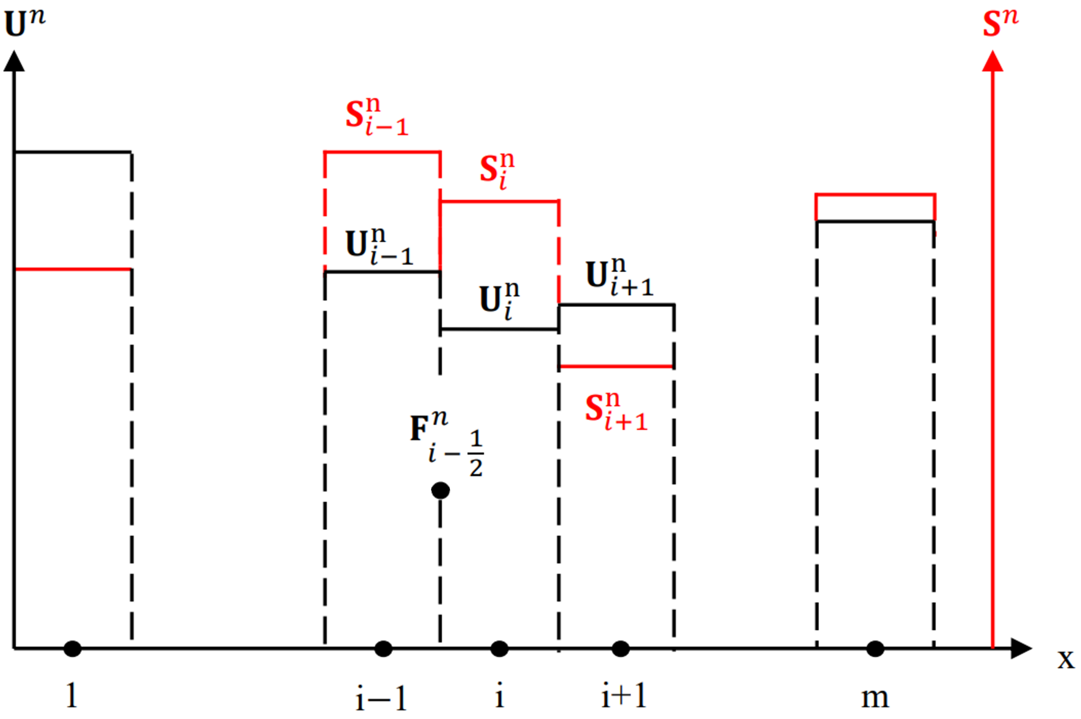

Figure 2.1: A schematic showing a 1D grid with m cells populated by a piecewise constant solution $\mathbf{U}$. The superscript n corresponds to the discrete time coordinate t^n and the subscript i to the cell index. The flux evaluated at the interface $i - \frac{1}{2}$ is shown as well as the source term (red).

$$
\begin{aligned}
\mathbf{F}^n_{i\pm\frac{1}{2}jk} &= \frac{1}{A\Delta t}\int_{\Delta t}\int_{A_{i\pm\frac{1}{2}}} \mathbf{F}\left[\left(i\pm\frac{1}{2}\right)\Delta x, y, z, t\right] \mathrm{d}A\mathrm{d}t \\
\mathbf{G}^n_{ij\pm\frac{1}{2}k} &= \frac{1}{A\Delta t}\int_{\Delta t}\int_{A_{j\pm\frac{1}{2}}} \mathbf{G}\left[x, \left(j\pm\frac{1}{2}\right)\Delta y, z, t\right] \mathrm{d}A\mathrm{d}t \\
\mathbf{H}^n_{ijk\pm\frac{1}{2}} &= \frac{1}{A\Delta t}\int_{\Delta t}\int_{A_{k\pm\frac{1}{2}}} \mathbf{H}\left[x, y, \left(k\pm\frac{1}{2}\right)\Delta z, t\right] \mathrm{d}A\mathrm{d}t
\end{aligned}
\tag{2.21}
$$

are the fluxes averaged over time and the cell interfaces. Figure 2.1 shows a 1D schematic of what the solution in a populated grid looks like.

$$
\mathbf{S}^n_{ijk} = \frac{1}{V\Delta t}\int_{\Delta t}\int_{V_{ijk}} \mathbf{S}(x, y, z, t)\mathrm{d}V\mathrm{d}t \tag{2.22}
$$

is the source term averaged over Δt and the cell volume V_{ijk}.

Equation (2.19) is still exact and forms the basis of all conservative schemes for the Euler equations. It is the way that quantities with the half-integer suffixes are approximated that distinguishes one scheme from another.

2.3.1 Calculating the intercell flux

The intercell fluxes are calculated from the solution to a so-called Riemann problem. Consider the following initial value problem (IVP)

$$\begin{aligned} \text{PDE:} \qquad & u_t + (au)_x = 0 \\ \text{IC:} \qquad & u(x,0) = u^0(x) = \begin{cases} u_{\mathrm{L}} & \text{if } x < 0 \\ u_{\mathrm{R}} & \text{if } x > 0 \end{cases} \end{aligned} \tag{2.23}$$

for a function with constant left (u_{L}) and right (u_{R}) states where $u_{\mathrm{L}} \neq u_{\mathrm{R}}$. This is the linear advection equation (LAE) written in conservative form, it is the simplest conservative PDE of hyperbolic type. It is also the simplest example of a Riemann problem, that is, an IVP for a function of two discontinuous data states that subsequently evolves according to some PDE. A solution to any Riemann problem is then a full description of what the function looks like at $\mathrm{t} > 0$, where its value can be evaluated at any point (x, t).

This is very useful for a numerical scheme like in MG, i.e. one that involves a grid of discontinuous data states. Here, a set of Riemann problems analogous to (2.23) can be defined at every cell interface, where the PDEs are the Euler equations and the initial condition is the fluid state on either side of the interface - forming the basis of the Godunov scheme (Godunov, 1959).

For the Euler equations, the solution to the Riemann problem is rather involved and is covered in more detail in the next section. Presently it can be said however that once the solution is known, the fluid state can be determined at the interface, making it possible to evaluate the intercell fluxes and update the solution in time. Only a 1D problem needs to be considered for a single interface, with the final solution being the sum of solutions for all the interfaces bounding a cell. This reduces (2.19) to

$$\mathbf{U}_i^{n+1} = \mathbf{U}_i^n - \frac{\Delta t}{\Delta x}\left(\mathbf{F}^{*n}_{\mathrm{i}+\frac{1}{2}} - \mathbf{F}^{*n}_{\mathrm{i}-\frac{1}{2}}\right), \tag{2.24}$$

where the term in the brackets is computed once for 1D, twice for 2D and three times for 3D. The source term is then subsequently added once the flux terms have been calculated. From a single solution, the intercell flux vector $\mathbf{F}^*$ is constructed as

$$\mathbf{F}^* = \begin{pmatrix} \rho^* u^* \\ \rho^* u^{*2} + p* \\ \rho^* u^* v^* \\ \rho^* u^* w^* \\ u^*(E^* + p^*) \end{pmatrix}. \tag{2.25}$$

The above form of $\mathbf{F}^*$ is the x-split 1D flux appropriate for a 3D grid. Reducing the number of dimension reduces the number of equations, and thus the number of transverse components $(\rho uv, \rho uw)$. The other terms remain the same.

2.3.2 Solution to the Riemann Problem

For any hyperbolic system of the form $\mathbf{U}_t + \mathbf{F}(\mathbf{U})_x = 0$, the characteristic polynomial $|\mathbf{A}(\mathbf{U}) - \lambda\mathbb{I}|$ yields a set of m real eigenvalues λ_m with corresponding m linearly independent right eigenvectors $\mathbf{r}_m$. Here m is the number of equations and $\mathbf{A}(\mathbf{U})$ is the Jacobian matrix $\partial\mathbf{F}(\mathbf{U})/\partial\mathbf{U}$. Physically, the eigenvalues represent speeds of propagating information, or *characteristic* speeds.

The system (2.23) has $m = 1$, $\mathbf{F}(\mathbf{U}) = au$ and $\mathbf{A}(\mathbf{U}) = a$, resulting in a single characteristic speed $\lambda_1 = a$. For the LAE, signals propagating with the speed a represent constant values of u i.e. $u(x,t) = u^0(x_0, 0) = u^0(x - at)$, giving a closed form solution such that the value of the function can be computed at any point

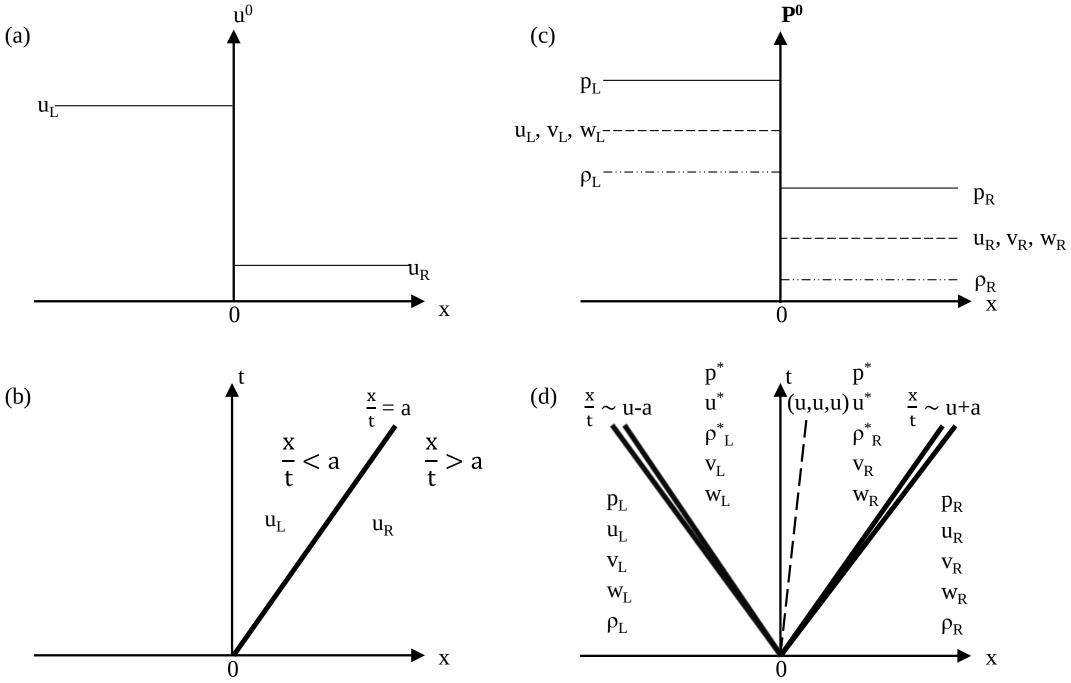

Figure 2.2: Initial conditions (a and c) and characteristic representations of the solution (b and d) for a Riemann problem for the linear advection equation (a and b) and the Euler equations (c and d). The single ray in (b) corresponds to the single characteristic at the initial discontinuity, with the field of characteristics to the left of the discontinuity not shown. The double rays in (d) correspond to characteristics of unknown type which can either be a shock or a rarefaction, and are dependent on the exact values of $\mathbf{P_L}$ and $\mathbf{P_R}$. The dashed characteristic in (d) is always a contact discontinuity.

at any time. For the system (2.23), this can be expressed as

$$u(x,t) = u^0\left(x - at\right) = \begin{cases} u_{\mathrm{L}} & \text{if } x < at \\ u_{\mathrm{R}} & \text{if } x > at \end{cases} \tag{2.26}$$

which can be illustrated in an $x - t$ plane by a set of characteristic curves $x(t) = x_0 + at$. Figure 2.2(a–b) shows a possible initial condition, and the characteristic for the discontinuity at $x_0 = 0$, i.e. $x(t) = at$.

For the Euler equations, the situation is a little trickier. It is often convenient to make use of the vector $\mathbf{P} = \left(\rho, u, v, w, p\right)^T$ of primitive variables, rather than the vector $\mathbf{U}$ of conserved variables, with density ρ, particle velocities u, v, w in the x, y, z directions, and pressure p. Input states for the Riemann problem are then $\mathbf{P_L}$ and $\mathbf{P_R}$, and obey the following equation for $\mathbf{P}$:

$$\frac{\partial \mathbf{P}}{\partial t} + \mathbf{A}\frac{\partial \mathbf{P}}{\partial x} = 0 \tag{2.27}$$

where the matrix $\mathbf{A}$ is given by

$$\mathbf{A} = \begin{pmatrix} u & \rho & 0 & 0 & 0 \\ 0 & u & 0 & 0 & 1/\rho \\ 0 & 0 & u & 0 & 0 \\ 0 & 0 & 0 & u & 0 \\ 0 & \rho a^2 & 0 & 0 & u \end{pmatrix} \tag{2.28}$$

with the eigenvalues of $\mathbf{A}$ being

$$\lambda_1 = u - a, \lambda_2 = \lambda_3 = \lambda_4 = u, \lambda_5 = u + a\ . \tag{2.29}$$

Here, a is the adiabatic sound speed $(\gamma p/\rho)^{\frac{1}{2}}$. The initial condition for this system is shown in Figure 2.2(c), with the resulting characteristic pattern shown in panel (d).

In general, the discontinuous states do not satisfy the Rankine-Hugoniot jump conditions. At $t > 0$, a nearly centered wave system thus develops to connect the two states. Their wavespeeds are not in general the characteristic speeds given by the eigenvalues, but instead are *associated* with them. Typically, the waves consist of a rarefaction wave, a contact discontinuity and a shock wave, e.g. typical waves seen in a *shock-tube problem* (Sod, 1978). Evolution for $t > 0$ is thus three waves separating four constant states which from left to right read $\mathbf{P}_{\mathrm{L}}$, $\mathbf{P}^*_{\mathrm{L}}$, $\mathbf{P}^*_{\mathrm{R}}$ and $\mathbf{P}_{\mathrm{R}}$. In Figure 2.2(d), the double rays represent characteristics of unknown type, as they can be either a shock wave or a rarefaction, and separate the inner starred region from the outer initial data. The middle wave separating the starred states is always a contact discontinuity, across which the pressure p^* and velocity u^* do not change. The density changes across all of the waves, and the transverse velocity components v and w are passively advected, simply switching from the left to right states across the contact discontinuity.

To compute the solution, one must consider two cases: one in which $u^* > 0$ and one in which $u^* < 0$. Each case has 5 sub-cases, giving a total of 10 realisations of the wave patterns (see fig. 6.5 in in Toro, 2009). The sampling of the solution is taken at $x = 0$ in the local frame of the Riemann problem, and all ten possible wave patterns must be taken into account for the sampling procedure. No closed form of the solution like that in (2.26) exists, however an exact solution can be derived for every portion of the flow by taking advantage of the constancy of p^* and u^* and applying the Rankine-Hugoniot relations across the waves. The resultant algebraic equations describing the regions are implicit, and thus an iterative procedure must be used to evaluate the solution at any desired location, $x = 0$ in our case. Such a procedure forms the basis of exact Riemann solvers, which can require intense computational effort.

2.3.3 First-order version of the scheme

The simplest way to solve the Riemann problem for the Euler equations, and that used in MG, is to construct an approximate solution by instead solving the linear problem

$$\frac{\partial \mathbf{P}}{\partial t} + \overline{\mathbf{A}}\frac{\partial \mathbf{P}}{\partial x} = 0 \tag{2.30}$$

where $\overline{\mathbf{A}}(\mathbf{P}_{\mathrm{L}},\mathbf{P}_{\mathrm{R}})$ is some mean matrix. In MG this is chosen to be

$$\overline{\mathbf{A}}(\mathbf{P}_{\mathrm{L}},\mathbf{P}_{\mathrm{R}}) = \mathbf{A}\left[\frac{1}{2}(\mathbf{P}_{\mathrm{L}}+\mathbf{P}_{\mathrm{R}})\right]. \tag{2.31}$$

The approximate solution to the Riemann problem satisfying (2.30) at x = 0 can then be given by

$$\begin{aligned}\mathbf{P}^* &= \mathbf{P}_{\mathrm{L}} + \sum_{\overline{\lambda}_i<0} \frac{\bar{\mathbf{l}}_i\cdot(\mathbf{P}_{\mathrm{R}}-\mathbf{P}_{\mathrm{L}})}{(\bar{\mathbf{l}}_i\cdot\bar{\mathbf{r}}_i)} \\ &= \mathbf{P}_{\mathrm{R}} - \sum_{\overline{\lambda}_i,>0} \frac{\bar{\mathbf{l}}_i\cdot(\mathbf{P}_{\mathrm{R}}-\mathbf{P}_{\mathrm{L}})}{(\bar{\mathbf{l}}_i\cdot\bar{\mathbf{r}}_i)}\end{aligned} \tag{2.32}$$

where $\overline{\lambda}_i$, $\bar{\mathbf{r}}_i$, $\bar{\mathbf{l}}_i$ are the eigenvalues and right and left eigenvectors of $\overline{\mathbf{A}}$ (Falle *et al.*, 1998). The fluxes can then be computed directly from $\mathbf{P}^*$ according to (2.25), with the fluid state updated according to (2.24). Note that for a first-order scheme, the maximum possible number of Riemann problems required for each cell is 6, corresponding to a 3D grid.

2.3.4 Second-order version of the scheme

To achieve second-order accuracy in space and time, piece-wise linear cell interpolation and a predictor-corrector method is used.

Firstly, the first-order version of the scheme (2.24) is used to obtain the conservative update, $\mathbf{U}_{\mathrm{ijk}}^{n+\frac{1}{2}}$ at half a timestep. The conserved variables are then converted into primitive variables $\mathbf{P}_{\mathrm{ijk}}^{n+\frac{1}{2}}$ and used to compute average gradients in each cell. For the x-direction, this is computed as

$$\left(\frac{\partial \mathbf{P}}{\partial x}\right)_{\mathrm{ijk}}^{n+\frac{1}{2}} = \frac{1}{\Delta x}\,\mathrm{av}\left(\mathbf{P}_{\mathrm{ijk}}^{n+\frac{1}{2}} - \mathbf{P}_{\mathrm{i-1jk}}^{n+\frac{1}{2}}, \mathbf{P}_{\mathrm{i+1jk}}^{n+\frac{1}{2}} - \mathbf{P}_{\mathrm{ijk}}^{n+\frac{1}{2}}\right), \tag{2.33}$$

where av(a,b) is an averaging function defined in Section 2.3.5. Next, the gradients are used to construct the left and right states immediately to the left and right of the interface as

$$\begin{aligned}
\mathbf{P}_{\mathrm{L}}^{\mathrm{n}+\frac{1}{2}} &= \mathbf{P}_{\mathrm{ijk}}^{n+\frac{1}{2}} + \frac{1}{2}\Delta x \left(\frac{\partial \mathbf{P}}{\partial x}\right)_{\mathrm{ijk}}^{n+\frac{1}{2}}, \\
\mathbf{P}_{\mathrm{R}}^{\mathrm{n}+\frac{1}{2}} &= \mathbf{P}_{\mathrm{i+1jk}}^{n+\frac{1}{2}} - \frac{1}{2}\Delta x \left(\frac{\partial \mathbf{P}}{\partial x}\right)_{\mathrm{i+1jk}}^{n+\frac{1}{2}},
\end{aligned} \tag{2.34}$$

with analogous expressions for y and z directions, together forming the basis of the "prediction" step.

For the "correction" step, the primitive variables from (2.34) are used as input states for a subsequent Riemann Problem, allowing us to use (2.32) to calculate more accurate intercell primitive variables and thus (2.25) for the half-timestep fluxes $\mathbf{F}^{*n+\frac{1}{2}}$. The final second-order time update then proceeds as

$$\mathbf{U}_i^{n+1} = \mathbf{U}_i^{n+\frac{1}{2}} - \frac{\Delta t}{2\Delta x}\left(\mathbf{F}_{\mathrm{i}+\frac{1}{2}}^{*n+\frac{1}{2}} - \mathbf{F}_{\mathrm{i}-\frac{1}{2}}^{*n+\frac{1}{2}}\right) \tag{2.35}$$

where again the term in the brackets is computed twice for 2D and three times for 3D, resulting in a maximum of 12 Riemann problems required for the second-order scheme. Note that the source terms are treated in the same way as the first-order scheme - with half-timestep contributions added after each of the two full iterations of the second-order update of $\mathbf{U}_i$.

2.3.5 Averaging function

We briefly comment on the function av(a,b) seen in equation (2.33). This is a non-linear averaging function with the goal of reducing the scheme to first order in the neighbourhood of discontinuities to ensure monotonicity and stability, and maintain second order everywhere else; see Godunov's theorem (Godunov, 1959).

The averaging function must therefore have the following properties

$$\begin{aligned}\mathrm{av}(a,b) &= \frac{1}{2}(a+b) && \text{as } a \to b \\ &= 0 && \text{if } ab < 0 \\ &\to a && \text{as } |a|/|b| \to 0 \\ &\to b && \text{as } |b|/|a| \to 0\end{aligned} \tag{2.36}$$

MG adopts the following prescription (Van Leer, 1977)

$$\begin{aligned}av(a,b) &= \frac{a^2b+ab^2}{a^2+b^2} \ \text{if } a^2+b^2 \neq 0 \text{ and } ab > 0\ , \\ &= 0 \qquad\qquad \text{otherwise}\ ,\end{aligned} \tag{2.37}$$

indeed satisfying the requirements.

2.3.6 Stability

The criterion for stability is known as the Courant-Friedrichs-Lewy (CFL) condition (Courant *et al.*, 1967) which sets a limit on the size of the timestep Δt. It reads as

$$\Delta t = \frac{C_{\mathrm{cfl}}\Delta x}{S^n_{max}}\ , \tag{2.38}$$

where $\mathrm{C_{cfl}}$ is the Courant, or CFL coefficient satisfying $0 < \mathrm{C_{cfl}} \leq 1$. S^n_{max} is the largest wave speed present throughout the domain at time level n, such that no wave present in the solution of all Riemann problems is allowed to travel more than a distance Δx in time Δt. This includes waves formed at the boundaries.

2.3.7 Scaling

In this work, the cgs system of units is used. As we are dealing with Astrophysical scenarios, quantities of interest take on extremely large ($\mathcal{O}(20)$) and extremely small ($\mathcal{O}(-20)$) values, making such a system of units incompatible with computation. To avoid array overflows or rounding errors, we can choose a set of reference values to construct scaling factors to normalise our quantities with, allowing us to express them in a more computationally amenable form. Once normalised, the computational values can be expressed back in cgs units by being multiplied by their scaling factors. Any reference values can be chosen, providing the dimensions are preserved so that the physics remains the same.

For our model, the reference values used are the length of a parsec $L_0\,[\mathrm{cm}]$, hydrogen mass $m_{\mathrm{H}}\,[\mathrm{g}]$, and the Boltzmann constant $\mathrm{k}\,[\mathrm{g\,cm^2\,s^{-2}\,K^{-1}}]$; all containing the four basis dimensions of length [L], time [T], mass [M] and temperature [K]. As a combination of these can give the dimensions of all other quantities in our work, we can construct the scaling factors as follows. The scaling factor for the length is chosen to be one of the reference values itself, that is, the length of a parsec, resulting in

$$1\,\text{code length [L]} \;=\; L_0\,[\mathrm{cm}] \;=\; 3.09\times 10^{18}\,[\mathrm{cm}]\ . \tag{2.39}$$

The scaling for the time is constructed using the Boltzmann constant k, hydrogen mass m_{H} and temperature T as $(kT/m_{\mathrm{H}})^{0.5}$ to obtain the velocity scaling factor V_0, which is used to evaluate V_0/L_0 giving

$$1\,\text{code time [T]} \;=\; T_0\,[\mathrm{s}] \;=\; 3.71992\times 10^{14}\,[\mathrm{s}]\ . \tag{2.40}$$

The scaling for mass is constructed using the scaled hydrogen number density

$n_{\rm H}\,[\mathrm{cm}^{-3}]$, multiplying it by $m_{\rm H}$ and a the scaled volume L_0^3, giving

$$1\,\text{code mass [M]} \;=\; M_0\,[\mathrm{g}] \;=\; 5.9\times10^{31}\,[\mathrm{g}]\ . \tag{2.41}$$

The temperature scaling is unchanged. From these values, pressure, energy, magnetic field strength and the gravitational constant can be determined in a similar fashion.

Additional to the normalisation of the cgs values into code units, it is possible to scale the spatial and temporal resolution to model systems at different scales. In MG this is done by scaling the length and timescale by a parameter called *rat*. This redefines the length and time values as

$$1\ rat\ \times\ \text{code length [L]} = rat \times L_0\,[\mathrm{cm}] = rat \times 3.09\times10^{18}\,[\mathrm{cm}] \tag{2.42}$$

$$1\ rat\ \times\ \text{code time [T]} = rat \times T_0\,[\mathrm{s}] = rat \times 3.71992\times10^{14}\,[\mathrm{s}]\ . \tag{2.43}$$

It then becomes possible to scale all the other quantities with appropriate substitutions of the above scaling. Note that the temperature and density remain unchanged. The latter of these therefore implies that mass transforms as

$$1\,rat^3\ \times\ \text{code mass [M]} = rat^3\ \times\ M_0\,[g]\ =\ rat^3\ \times\ 5.9\times10^{31}\,[g]\ . \tag{2.44}$$

2.4 Source terms

In non-cartesian coodtinates, one has to be careful with evaluating sources (Falle, 1991). However, for Cartesian grids, if the source term depends only on $\mathbf{U}$, the first order approximation is just

$$\mathbf{S}^n_{\rm ijk} = \mathbf{S}(\mathbf{U}^n_{\rm ijk})\ . \tag{2.45}$$

For second order, the source terms are additionally evaluated with the state $\mathbf{U}^{n+\frac{1}{2}}_{\mathrm{ijk}}$ constructed at half a timestep. As the sources give rates per unit volume, the addition to the conservative update in a cell is evaluated as

$$\mathbf{S}^{n}_{\mathrm{ijk}}\Delta t \ . \tag{2.46}$$

2.4.1 Heating and cooling

Depending on what conditions the ISM finds itself in, a diverse range of atomic processes will be permitted to take place. Consequently, photons of different wavelengths are absorbed and released at different rates, resulting in local contributions to energy losses and gains. Changes resulting from these processes can have dynamical significance, and therefore must be carefully considered when modelling ISM systems.

One method of approximating these processes is by including a source term of the form $\rho\mathcal{L}(\rho, T)$ in the energy equation, as has been done in this work. The function

$$\mathcal{L}(\rho, T) = \frac{1}{m_{\mathrm{H}}}\Gamma - \frac{\rho}{m^2_{\mathrm{H}}}\Lambda(T) \tag{2.47}$$

is a heat-loss function where Γ is a constant heating rate set in this work to $= 2\times10^{-26}\,\mathrm{erg\,s^{-1}}$, and $\Lambda(T)$ is a temperature dependent cooling coefficient with units $\mathrm{erg\,cm^3\,s^{-1}}$. Our temperatures of interest span a wide range up to $10^9\,\mathrm{K}$, which in reality considers material composed of molecular gas at low temperatures, and plasma at high temperatures. Thus our cooling coefficient has been developed using data for 3 separate temperature regimes (Wareing *et al.*, 2016a), with the following contributions to the cooling coefficient being used.

For lower temperatures ($\mathrm{T} \leq 10^4\,\mathrm{K}$), the contribution is that of a corrected fit to the data in Koyama & Inutsuka (2000). They consider both calculations from Wolfire *et al.* (1995) for $\mathrm{n} < 10^3\,\mathrm{cm^{-3}}$, and their own non-equilibrium cal-

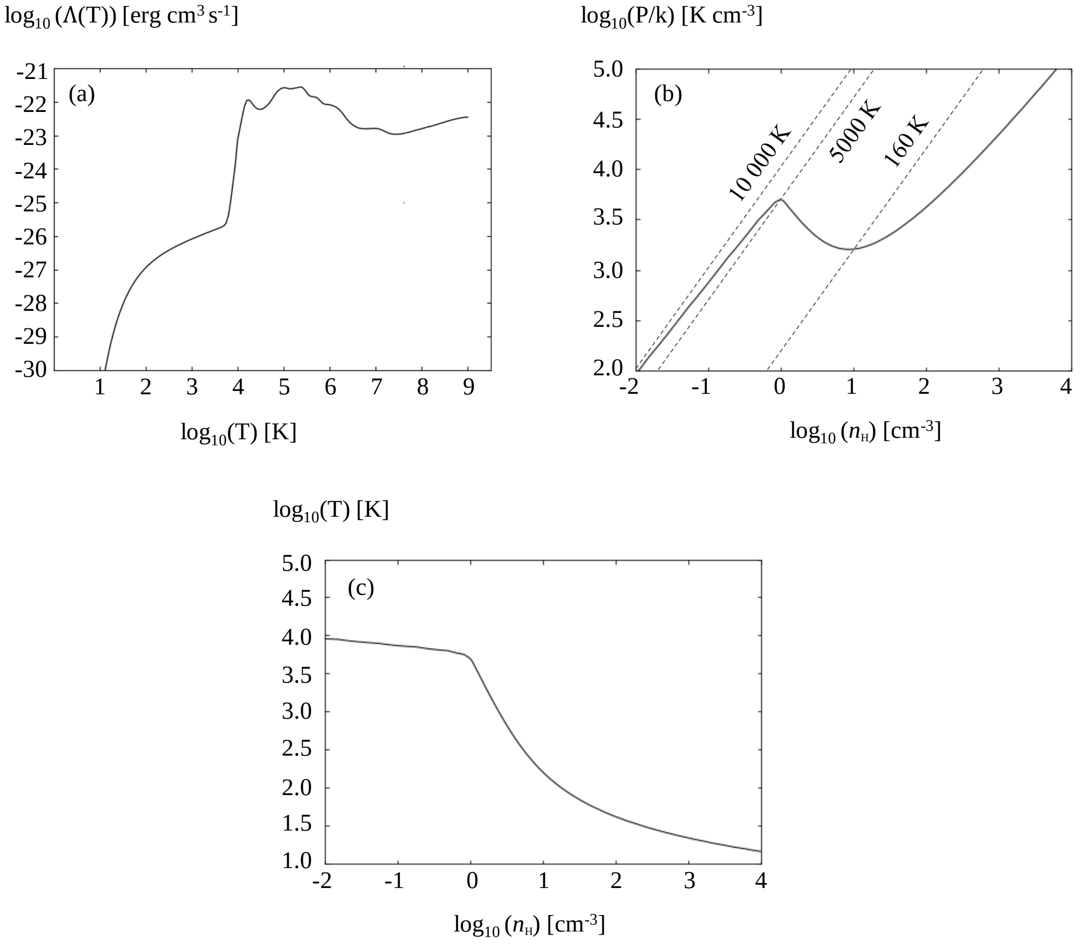

Figure 2.3: (a) Cooling coefficients consisting of contributions due to Koyama & Inutsuka (2002) ($\mathrm{T} < 10^4\,\mathrm{K}$), CLOUDY ($10^4 < \mathrm{T} < 10^{7.6}\,\mathrm{K}$), and MEKAL ($10^{7.6} < \mathrm{T} < 10^9\,\mathrm{K}$). (b) Equilibrium pressure ($\mathcal{L}(\rho, T) = 0$) in pressure-density space. (c) Equilibrium temperature ($\mathcal{L}(\rho, T) = 0$) in temperature-density space.

culations for $10^3 < \mathrm{n} < 10^6\,\mathrm{cm}^{-3}$. The original fit to these processes was done by Koyama & Inutsuka (2002) however contained two typographical errors, and was subsequently corrected by Vázquez-Semadeni *et al.* (2007) to give

$$\frac{\Lambda}{\Gamma} = 10^7 \exp\left(\frac{-1.184 \times 10^5}{T + 1000}\right) + 1.4 \times 10^{-2} T^{1/2} \exp\left(\frac{-92}{T}\right) \tag{2.48}$$

where the same value of Γ is used as our work.

Between $10^4 < \mathrm{T} < 10^{7.6}\,\mathrm{K}$, data for the contributions is taken from Gnat & Ferland (2012). The calculations of Gnat & Ferland (2012) were performed using CLOUDY v10.00 (Ferland *et al.*, 1998) whose full capabilities can be found detailed in Osterbrock & Ferland (2006). For temperatures in the range $10^{7.6} < \mathrm{T} < 10^9\,\mathrm{K}$ the plasma emission code MEKAL was used (Kaastra, 1992; Mewe *et al.*, 1992, as distributed in XSPEC v11.2.0). Its capabilities and developments from the previous version of the code MEKA are outlined in Mewe *et al.* (1992)

The resultant form of the cooling coefficient up to the maximum temperature $\mathrm{T} = 10^9$ is shown in Fig 2.3(a). The region where $\mathcal{L}(\rho, T) = 0$, i.e. $\frac{1}{m_{\mathrm{H}}}\Gamma = \frac{\rho}{m_{\mathrm{H}}^2}\Lambda(T)$ is shown in pressure-density space in Fig. 2.3(b) and temperature-density space in Fig. 2.3(c), respectively representing the equilibrium pressure and temperature. As mentioned in Section 1.2.2, where $dP/dn < 0$ the gas is thermally unstable to isobaric perturbations, and is stable where $dP/dn > 0$. Thus, two thermally stable phases can coexist in pressure equilibrium within the pressure range $P_{\mathrm{min}} < \mathrm{P} < P_{\mathrm{max}}$. At pressures greater than $P_{\mathrm{max}} = 10^{3.69}\,\mathrm{K\,cm}^{-3}$, only the cold phase (CNM) can exist and below $P_{\mathrm{min}} = 10^{3.19}\,\mathrm{K\,cm}^{-3}$ only the warm phase (WNM) can exist. The CNM begins at the cold temperature minimum ($dP/dn = 0$) at $\mathrm{T} = 160\,\mathrm{K}$, and the WNM begins at the warm temperature maximum lying at $\mathrm{T} = 5000\,\mathrm{K}$, which are both marked on Fig 2.3(b). The isotherm that brackets the hot phase (HIM) from the WNM is also shown at $\mathrm{T} = 10\,000\,\mathrm{K}$, where only non-equilibrium material is permitted to exist.

Numerically, once the cooling rate has been calculated for a cell located at x_{ijk}, the source term is evaluated as $\rho_{\mathrm{ijk}}\mathcal{L}(\rho_{\mathrm{ijk}}, T_{\mathrm{ijk}})$ giving an energy rate per unit volume as expected. This contribution to the energy is then updated according to equation (2.46).

2.4.2 Gravity

The existence of mass in space necessarily results in a gravitational field that defines a potential obeying the Poisson equation

$$\nabla^2\phi = 4\pi G\rho\,. \tag{2.49}$$

In Astrophysical scenarios where the timescales of interest are much shorter than the gravitational free-fall time, its effects can be ignored. When the timescales are comparable, gravity must be included in order to elucidate its effects on the dynamics. In the equations of hydrodynamics, this is done by including the solution to (2.49) as a momentum source $-\rho\nabla\phi$, and including an appropriate contribution to the total energy.

There are many techniques to treat the Poisson equation numerically. As it is an equation of elliptic type, these techniques differ from methods for hyperbolic problems. The technique used in MG is the multigrid method. This method relies on a relaxation technique that takes the discretised Laplacian operator $\mathbf{L}$, and calculates a residual error r_0 as

$$\mathbf{L}\phi_0 - 4\pi G\rho = r_0 \tag{2.50}$$

where ϕ_0 is an initial guess for the value of the potential. The residual error is then used to update the potential, and a subsequent iteration is calculated as

$$\mathbf{L}(\phi_0 + \phi_1) - 4\pi G\rho = r_1 \tag{2.51}$$

with ϕ_1 being a correction to the potential and r_1 being a new residual. This then continues for n iterations as

$$\mathbf{L}\sum_{n} \phi_{\mathrm{n}} - 4\pi G\rho = r_{\mathrm{n}} \tag{2.52}$$

and is stopped once the residual error reaches a certain threshold, typically $\sim \mathcal{O}(10^{-4} - 10^{-6})$. It can then be said that the approximation of the potential resembles the value of the true potential. Note that care must be taken with what boundary conditions are used with MG by default assuming a value of the potential of 0 at the boundaries.

The complete technique used in MG is known as the full-approximation multigrid, and the interested reader on multigrid techniques, how boundary conditions are treated, and how these methods are implemented in parallel on an adaptive grid is referred to Briggs *et al.* (2000).

2.5 Adaptive mesh refinement

When modelling flows at high resolution, it is often appropriate to limit it to regions that really require it. This is beneficial as it is often the case that many regions of the flow vary smoothly, and an increase in resolution would not result in higher accuracy of the solution. On finite volume grids this can be done using Adaptive Mesh Refinment (AMR).

The basic idea of AMR is to increase the resolution of the grid in regions that require it, and decrease it in regions that do not. To control where in the flow this happens, an appropriate criterion must be chosen based on the solution of the flow and in this way, the grid can evolve as the solution evolves. In MG, this is done by initialising the domain with a hierarchy of grids G_0 ... $G_{\text{N-1}}$ where N is the number of levels chosen for the simulation. Levels G_0 and G_1 are initialised by default and cover the whole domain. The fractional difference between solutions within a cell and its parent is used to control refinement, and on a cell-by-cell basis finer cells are created in regions that exceed a given error tolerance. When the error in refined cells falls below that tolerance, they are subsequently removed. A cell on G_0 has size Δx and timestep Δt and has size $\Delta x/2^{\text{N-1}}$ and timestep $\Delta t/2^{\text{N-1}}$ on the N^{th} level in order to ensure the fluid step is synchronised at coarse and fine boundaries. Such a grid structure improves the efficiency of the code.

2.6 Parallelisation

The capabilities of a program are limited by the capabilities of the computer it is executed on, in particular the memory and processing power. The memory dictates how much data can be processed at any given time, and the processing power dictates how fast this can take place. For three-dimensional simulations like ours, the number of grid cells ($n_{\text{cells}} \sim \mathcal{O}(10^6)$), joins ($n_{\text{joins}} \approx 6n_{\text{cells}}$)) and the data structures containing the fluid variables typically require $\sim 50-100$ GB RAM and ~ 100 cores in order to have a total simulation run-time of less than 100 hours. It would be impossible to perform such simulations on a typical single-CPU machine.

A way around this problem is to optimise the code for execution on parallel processors. This can be done quite easily for simple programs with a few lines of code, however it is more involved if one wishes to extend the capabilities of the code for larger problems. One way of doing this is by decomposing the computational domain into sub-domains, and distributing them across a number of processors. Each processor then deals with one or more of the sub-domains, and communication between sub-domains takes place within a perimeter of ghost cells that contain copies of the boundary values of each neighbouring sub-domain. In MG, the parallelisation has been implemented according to the message-passing paradigm using the Message Passing Interface (MPI) standard. For details on the MPI library, and how this can be implemented into a hydrodynamical code please consult chapter 3 of Wareing (2005).

Chapter 3

Shock-cloud interactions in the small cloud regime

The content of this chapter has been published in the paper titled “Interactions of a shock with a molecular cloud at various stages of its evolution due to thermal instability and gravity” (Kupilas *et al.*, 2021).

3.1 Introduction

Stars form in cold and dense cores, themselves embedded in giant molecular clouds (GMCs). GMCs are clumpy and filamentary (André *et al.*, 2014) and are understood to be characterised by a turbulent velocity field (Larson, 1981). This dynamical state of GMCs must be partly driven and maintained by physical processes that form them and their substructures, however what physics dominates at different stages is not fully understood.

In the ISM, density inhomogeneities can partly be attributed to thermal phase transitions due to inherent instabilities resulting from the balance of heating and cooling processes (Parker, 1953; Field, 1965; Field *et al.*, 1969; Wolfire *et al.*, 1995, 2003). This thermal instability (TI) can develop in association with other processes, however it has been demonstrated that even in isolation, the TI is an effective mechanism for converting warm diffuse gas into cold and dense material, generating conditions for star formation, and driving large scale flows that result in turbulence-like velocity characteristics (Wareing *et al.*, 2016a, 2019, 2021, hereafter WPFVL16, WFP19, WPF21).

To study the TI in isolation, WPFVL16 performed 3D simulations of a quiescent 17 000 $\mathrm{M}_{\odot}$ cloud seeded with $\pm\,10$ per cent density perturbations around an equilibrium state of $n = 1.1\,\mathrm{cm}^{-3}$ in the warm unstable phase, reflecting a possible resultant/intermediate state of gas after the passage of e.g. a spiral arm shock. The simulations performed involved successive increases in complexity by including gravity and magnetic fields of different strengths, neglecting any additional mechanisms such as driven turbulence, converging flows or feedback. They found that after $\sim 20\,$Myrs of evolution the growth of the density perturbations formed clumps (and in the magnetic field scenarios, filaments) with properties that connected well with observations of molecular clouds. A higher resolution hydrodynamic (HD) study by WFP19 of a more massive cloud explored the interplay between gravity and the TI and found that realistic clump masses, sizes, velocity dispersions and power spectra could be achieved without resorting to additional driving mechanisms. Additionally, the clumps were connected by $0.3-0.5\,$pc width filaments that continuously fed material to the clumps and as the original cloud had $8\times$ the mass of WPFVL16, the clumps were able to gather enough mass to collapse under gravity and conclude the star formation process. Most recently, a higher resolution study by WPF21 including TI, magnetic fields and gravity now also provides possible explanations for the origins of features such as striations (Goldsmith *et al.*, 2008), hour glass magnetic fields (Pattle *et al.*, 2017) and the integral shaped filament (ISF) in the Orion A molecular cloud (Stutz & Gould, 2016; Stutz *et al.*, 2018).

The studies of WPFVL16/WFP19 were highly idealised. It is now appropriate therefore to incrementally introduce extra dynamical ingredients. For example, as the timescales of evolution of the models in WPFVL16 are long and the clouds were evolved for a free-fall time of $\approx 50\,$Myrs, it is likely that in reality a cloud like this would experience one or more shocks.

As discussed in Chapter 1, interaction of shocks with clouds is a ubiquitous problem already studied by many authors so the basic physics of the interaction is well understood.

In the literature, many works mainly focus on the effects of different physics on the particulars of the cloud destruction. However, the compression due to a shock can also be an effective mechanism for generating cold dense clouds out of warm diffuse gas, triggering the thermal instability and in the process generating the conditions for star formation (e.g. Inoue & Inutsuka, 2009; Aota *et al.*, 2013; Inoue & Omukai, 2015).

For example, Van Loo *et al.* (2007, 2010) explored in both 2D and 3D the effects of a shock interacting with diffuse atomic clouds initially in a warm stable state with a density of $n = 0.45\,\mathrm{cm}^{-3}$. They included an adapted cooling function and magnetic fields, and found that depending on the magnetic field orientation relative to the shock normal, magnetically dominated clouds formed with properties that resembled those of molecular clouds and low-density HI clouds. Since the effects of heating and cooling were also included, the transmitted fast mode shocks demonstrated an ability to trigger the TI. Similar results were found by Heitsch *et al.* (2009) which affirmed the utility of shock-cloud interactions in creating conditions ideal for the formation of dense molecular clumps. However, as gravity was not included, and their resolution was too low to fully resolve the cooling length, it was not possible to elucidate the importance of the TI and witness the formation of clumps and cores.

In this chapter we build on the work of WPFVL16 which included gravity and sufficient resolution to track the behaviour of the TI, by introducing a shock. We thus present a self consistent HD model of molecular cloud formation due to the TI, gravity and shocks. We track the evolution of a cloud from initially quiescent atomic gas, to the formation of clumps that eventually collapse under gravity, demonstrating the ability of the clouds to form stars. During their evolution we explore the relative importance of the physical processes driving their behaviour. In Section 3.2 we present the numerical method and the models studied. In Section 3.4 we present the results and discussion, and in Section 3.3 we provide a summary and conclusion.

3.2 Setup

3.2.1 Numerical Method

In this chapter we present 3D hydrodynamic simulations of the interaction of a shock with a cloud that is evolving due to the thermal instability and gravity. All calculations were performed using the adaptive mesh refinement (AMR) code MG (Falle, 1991, 2005; Hubber *et al.*, 2013). The details of how the code works has been discussed in Chapter 2 and we refer the reader there.

3.2.2 Model

The model used for this work is similar to the set-up used in scenario 3 in WPFVL16. Namely, we initialise 17 000 $M_\odot$ of diffuse material within a spherical cloud with a 50 pc radius. The cloud lies at the center of a uniform Cartesian domain with numerical dimensions of $-3 < xyz < 3$ thus with corresponding physical dimensions of 300 pc on each side . The cloud is seeded on the grid scale with ± 10 per cent random density variations around an equilibrium state of $n_{\rm cl} = 1.1$ cm^{-3}, with a pressure set according to the unstable equilibrium of heating and cooling at $P_{\rm eq}/k = 4800 \pm 300$ K cm^{-3}. We assume a mean particle mass of 2.0×10^{-24} g. The initial condition at $t = 0$ and the dependence of the equilibrium pressure on

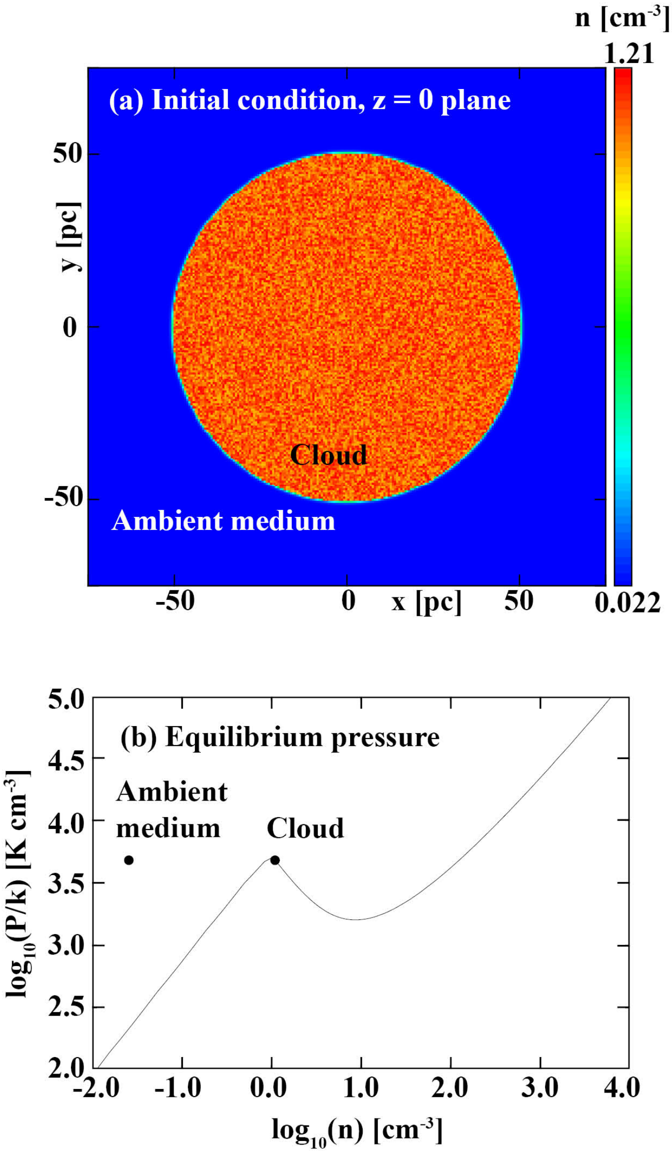

Figure 3.1: (a): Initial condition showing density perturbations in a density slice through $z = 0$. (b): Equilibrium pressure against density for the warm, unstable and cold ISM. The initial condition of the cloud and ambient gas with $\chi = 50$ are marked on the plot.

the density with the cloud and ambient state are shown in Fig. 3.1.

The cloud is embedded in a lower density medium with a density contrast $\chi = 50$ ($\chi = n_{\rm cl}/n_{\rm amb}$) thus setting the ambient density as $n_{\rm amb} = 0.022$ cm^{-3}. In order to keep the cloud confined, the surroundings are set with an equivalent pressure of $P/k = 4800$ K cm^{-3}, without the fluctuations, resulting in a temperature of 218 000 K. Gas in the ISM with these temperatures has a short cooling time of $\sim$ 0.2 Myrs, which is significantly lower than the dynamical timescale characterised by the free-fall time $t_{\rm ff}$ defined as

$$t_{\rm ff} = \sqrt{\frac{3\pi}{32G\rho}}, \tag{3.1}$$

which for $n = 1.1$ cm^{-3} is 45 Myrs. For this reason, the heating and cooling are switched off in the ambient medium to keep the cloud confined during its quiescent (shock-less) evolution. The heating and cooling is controlled via an advected scalar α that is set to 1 in the cloud and 0 everywhere else, and heating and cooling is switched on only in regions where $\alpha > 0.9$. It is possible to confine the cloud in a lower density medium where $t_{\rm cool} > t_{\rm ff}$, however this raises the temperature and shortens the timestep, thus a choice of $\chi = 50$ ensures the simulations are not too computationally expensive. When the shock is introduced, the ambient medium is reset to $n = 0.0022$ cm^{-3} ($\chi = 500$) which adjusts the temperature to $T \approx$ 2 182 000 K, and heating and cooling are switched on everywhere in the domain. Additionally, to prevent any numerical errors from developing due to sharp edges and large density contrasts, and since clouds in the ISM are unlikely to have sharp edges (e.g. see discussion in Nakamura *et al.*, 2006), we smooth out the cloud interface over $\sim$ 5 cells. Note that for our resolution, our clouds have $\sim$ 170 cells per radius, and so the smooth edges will not have a significant impact on the growth rate of dynamical instabilities (Pittard *et al.*, 2009).

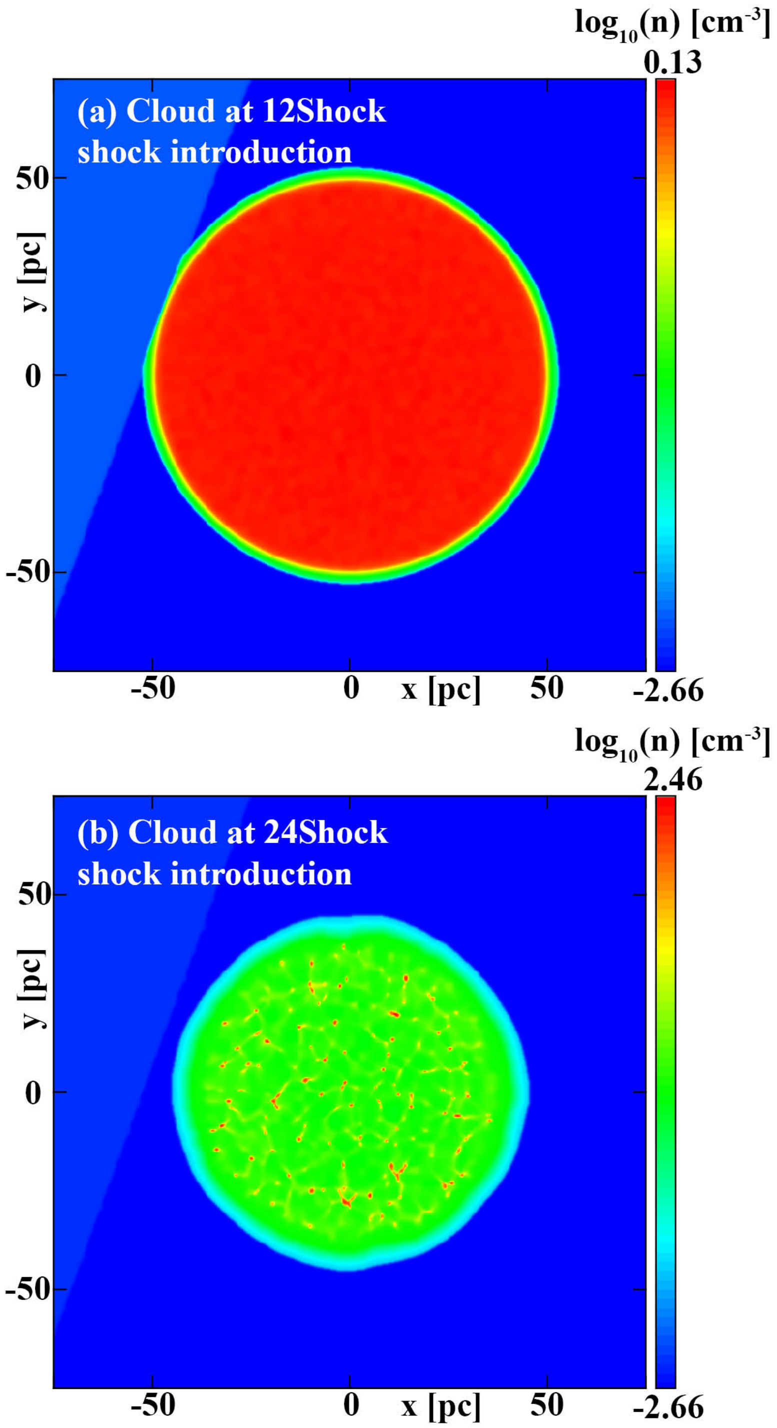

Figure 3.2: (a): Cloud at shock introduction for *12Shock* scenario after 11.78 Myrs of evolution. (b): Cloud at shock introduction for *24Shock* scenario after 23.58 Myrs of evolution.

3.2.2.1 Resolution and thermal instability

The model employs 8 levels of AMR where the coarsest grid, G_0, was set with a small number of cells (8^3) to ensure fast convergence of the multigrid solver. This meant that if fully populated, the finest grid G_7 would employ 1024^3 cells resulting in an effective resolution of 0.29 pc. Note that the shocked simulations also include a further single level of AMR for the *12Shock* scenario and two extra levels of AMR for the *24Shock* scenario towards their final stages, as they reach the resolution limit quickly.

Koyama & Inutsuka (2004) assert that for simulations of the TI to converge, one must include thermal conduction and resolve the Field length by at least 3 cells, which they call the “Field condition”: we do neither of those things. According to their equation (11) the Field length for our initial unperturbed density is 0.0587 pc. We note however that their equation (11) is incorrect, and a more appropriate expression for the Field length was derived by Falle *et al.* (2020) and is included in the appendices of KWPF21 and WPF21. This expression gives a Field length of 0.594 pc for our unperturbed density, so we would require closer to 20 cells. In any case, to satisfy this we would require excessive computational resources. However, Falle *et al.* (2020) showed that with thermal conduction for our initial density $n = 1.1$ cm^{-3}, rather than being narrowly peaked, the growth rate has a rather broad maximum between the Field length and the thermal length located at $\lambda = 8.95$ pc. Thus the TI does not depend strongly on increases in resolution within this range. In all of our simulations, perturbations grow initially at the grid scale but rapidly increase beyond that scale to large clumps. Although we exclude thermal conduction, these are nevertheless separated by length scales roughly corresponding to the wavelength with the maximum growth rate which is in common with various other authors who, despite insufficient resolution for the Field length, recover the properties of a thermally bistable medium – it is accepted that such properties as the mass function of cold clumps and the power spectra of velocity and density are known to converge on large scale (Gazol *et al.*, 2005; Vázquez-Semadeni *et al.*, 2006; Hennebelle & Audit, 2007; Inoue & Omukai, 2015). Since our intention is to examine the large-scale interaction of a shock with a cloud, we argue that it is sufficiently resolved in this Chapter. This is explored further and accompanied by resolution tests for both HD and MHD cases respectively in the appendices of KWPF21 and WPF21.

Our grid is set up so that 3 levels fully populate the domain and 8 levels fully populate the cloud region. This is in contrast to WPFVL16 who employed 5 fully populated levels with the remaining 3 refining and de-refining dynamically. Our choice is so that we are able to track all of the dynamics within the cloud when the shock is introduced and for numerical consistency, we keep this setting on throughout all of the cloud's evolution. It also allows us to extend the size of the domain from the $-1.5 < xyz < 1.5$ used in WPFVL16 at little computational cost; placing the grid boundaries further from the cloud reduces the possibility of the cloud advecting off the grid and being affected by any shock induced reflected waves at the boundaries. It is important to note that fully refining the cloud does affect the initial behaviour of the TI, and so our evolution deviates slightly from WPFVL16. As the refinement of their highest 3 levels was not fixed, it resulted in their AMR grid de-refining to the 5th level as the density variations seeded in the initial condition smoothed out. As our inital perturbations smooth out, our grid does not de-refine and thus the growth rate at our highest level is larger than theirs and the TI develops earlier. This results in a difference in evolution timescales, where their model experiences a delayed phase transition when compared to ours, and is seen to evolve for approximately a full analytical free-fall time of $\sim$ 50 Myrs before reaching the state that we do at $\sim$ 35 Myrs. We stress again however that while the timescales are different, the final established state of the TI in terms of number, mass distribution and separation of clumps, is unaffected by this.

3.2.3 Scenarios

There are three scenarios studied in this work. The first scenario *NoShock*, follows the evolution of the quiescent cloud described in the previous section. This is left to evolve for a free-fall time and used to compare against scenarios with shocks. In the second scenario *12Shock*, the quiescent cloud is evolved for ~ 12 Myrs and then a shock is introduced, we refer to the cloud as being in a "pre-TI" state. In the third scenario *24Shock*, the quiescent cloud is left to evolve for ~ 24 Myrs into a "post-TI" state before a shock is added. Note that the *NoShock* scenario is evolved using the Godunov solver until the gradients become too large; it is then changed to Kurganov-Tadmor which is more diffusive and smears out the sharp gradients. This has a small effect on the mass distribution, however it eventually gets reconciled and it does not effect the global evolution of the cloud. For the shocked scenarios we switch to Kurganov-Tadmor immediately prior to shock introduction, as the gradients introduced by the shock require a more diffusive solver.

The shock is artificially imposed on the grid by setting the values of cells to the left of the shock front according to the Rankine-Hugoniot relations. The shock then propagates from left to right. Note that cells that lie on the boundary in the post shock region are also set to the post-shock values. The shock front is defined by the normal vector which lies at $\mathbf{r} = 1.05\hat{r}$ and $\theta = 160^\circ$ where $\mathbf{r}$ is the radial vector from the origin (where unit length $= 50\,\mathrm{pc}$) and θ is the angle counterclockwise from the positive x-axis. This angle was chosen as simulations with the shock propagating directly along the x-axis saw the formation of artificial structures. This was due to the Quirk instability (carbuncle phoenomenon)

(Quirk, 1997) which commonly arises in upwind schemes when the angle between the flow and grid axes is small. After the shock has been imposed it is evolved for a few short time-steps in order for the AMR grid to refine to the finest level at the shock front in regions where it is not fully refined. Following this, it is reimposed tangent to the cloud. In both scenarios, the shock has a Mach number of $M = 1.5$, where $M = v_{\rm s}/c$ for a shock with velocity $v_{\rm s}$ moving into a stationary material with a sound speed c. The associated clouds at those times are shown in Fig. 3.2, which can be considered as the initial conditions for the shocked scenarios. The simulations are then evolved for a further 5.16 Myrs and then stopped as densities reach values that are beyond the resolution limit set by the Truelove criterion (Truelove *et al.*, 1997). The resolution is then increased by allowing additional grid levels and the simulation is evolved for an additional 1.5 Myrs.

As mentioned in Chapter 1, we approximate the shock as planar and assume that the post-shock state is time-independent. This makes it the simplest approximation of a more complex interaction, e.g. between a cloud and a supernova remnant in the Sedov-Taylor stage. Recall from section 1.2.5.2, an approximation like this requires that the distance of the blast origin and the closest cloud edge $R_{\rm c}$ be much larger than the cloud radius $r_{\rm cl}$, i.e. $r_{\rm cl} \ll R_{\rm blast}$. This is so that the blast is far enough to remove any shock curvature locally to the cloud, and for the post-shock pressure to not change on timescales under consideration, characterised by a large pressure variation timescale $t_{\rm P}$. In our models, we are assuming $R_{\rm c} = t_{\rm P} = \infty$, thus studying the models in the *small cloud regime* as introduced in Klein *et al.* (1994) (see equation 1.14 in Chapter 1).

Even though the clouds at 12 and 24 Myrs are very different from one another, it is useful to consider their evolution in terms the established theoretical timescales presented in Section 1.2.5.1 (Klein *et al.*, 1994), which we recapitulate here. For a cloud with radius $r_{\rm cl}$ and an external shock with velocity $v_{\rm s}$, the time taken for the external shock to sweep across the cloud, the *shock crossing* timescale, is defined as

$$t_{\rm sc} \equiv \frac{2r_{\rm cl}}{v_{\rm s}}. \tag{3.2}$$

During this period, a shock is driven into the cloud which propagates approximately with a velocity

$$v_{\rm s,cl} \equiv \frac{v_{\rm s}}{\chi^{1/2}}. \tag{3.3}$$

The characteristic time for the cloud to be crushed by the transmitted shock, i.e the *cloud crushing timescale*, can now be defined as $r_{\rm cl}/v_{\rm s,cl}$, or as

$$t_{\rm cc} \equiv \frac{\chi^{1/2} r_{\rm cl}}{v_{\rm s}}. \tag{3.4}$$

These are the basic timescales governing the evolution of the shocked cloud. For our models with $\chi = 500$, $M = 1.5$ and $r_{\rm cl} = 50$ pc, we have $v_{\rm s} = 240$ km s^{-1}, $t_{\rm sc} = 0.41$ Myrs, $v_{\rm s,cl} = 10.7$ km s^{-1} and $t_{\rm cc} = 4.6$ Myrs.

It is important to note that these values are approximate and are derived for an adiabatic shock in a uniform cloud. While our shock is adiabatic in the ambient medium, inside the cloud it is radiative, and for model *24Shock* there is structure inside the cloud. Nevertheless we find that the shock in our models still propagates on this timescale. This is in line with other works who comment on the validity of this approximate timescale in describing fractal clouds with large density contrasts (Banda-Barragán *et al.*, 2019), where $t_{\rm cc}$ is understood as an average value of a distribution of cloud-crushing times intrinsic to the gas density distribution.

3.3 Results and discussion

In this section we first present the evolution of the *NoShock* scenario. Following that, the evolution of the *12Shock* and *24Shock* scenarios are described. For the *NoShock* scenario the times quoted are since $t = 0$. For the shocked scenarios the first times quoted are those elapsed since shock introduction, t - $t_{\rm shock}$, and the corresponding times since $t = 0$ are quoted in brackets.

3.3.1 Scenario 1 - *NoShock*

Fig. 3.3 shows the evolution of the *NoShock* scenario in density slices in the $x-y$ plane (slice through $z = 0$). Prior to Fig. 3.3(a) at 10.32 Myrs the cloud remains effectively unchanged with all gas initially found in the thermally unstable phase. The instability is seeded by the pressure variation across the cloud which grows initially on the smallest scales. The material in the cloud must then evolve into a thermally stable phase, where either it condenses into a cold, dense phase or evaporates into a warm diffuse phase. This results in the characteristic two-phase medium of Field *et al.* (1969) which is seen to develop here. Fig. 3.3(a – d) capture the first moments of the phase transition from the initially quiescent cloud. As there are no external influences on the cloud, the long period of quiescence up to this point reflects the growth rate of the TI at this resolution, which is relatively long but nevertheless shorter than the gravitational timescale.

Number densities of $\sim$ 100 cm^{-3} are first seen around 18 Myrs, which are complemented with drops in temperature by nearly 2 orders of magnitude from $\sim$ 4000 K to 100 K. Fig. 3.3(e) shows the first instance where a small number of higher density locations have emerged with clear, lower density structures spread throughout the cloud. These inhomogeneities are seen to develop into clumps at different rates, with some clumps clearly growing in mass and size faster than others. By 21.37 Myrs (Fig. 3.3f) there are a large number of clumps

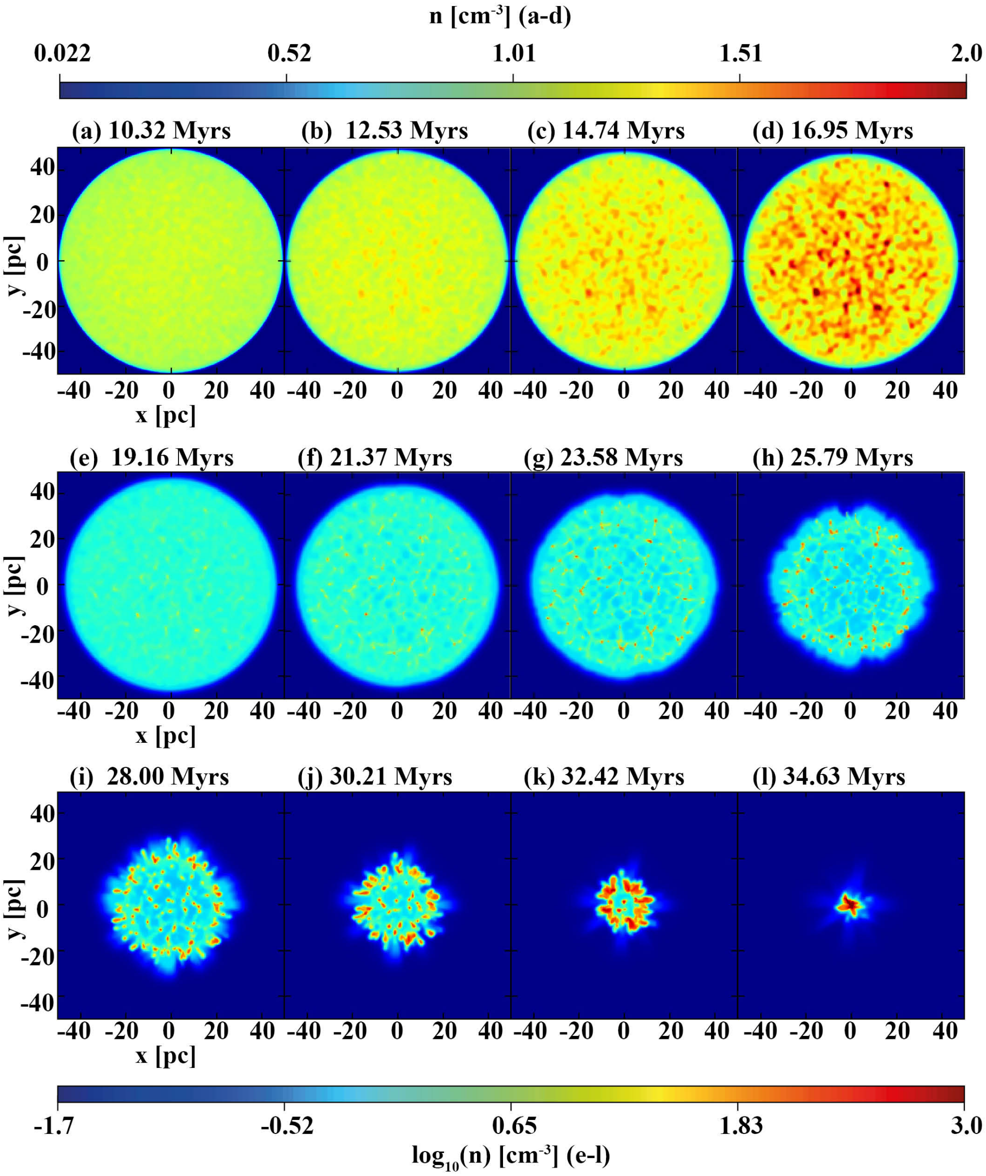

Figure 3.3: Slices through $z=0$ of the *Noshock* simulation evolving over a period of ~ 15 Myrs. Minimal change is seen in the cloud from $t=0$ to 10.32 Myrs and hence these snapshots are not shown. Snapshots highlight the onset of the instability (a−d), its development into a two-phase medium (e−h), and the final collapse of the cloud (i−l).

visible which are approximately separated at distances of 10 – 15 pc. The average separation decreases to $\sim 5 - 10$ pc as more condensations form out of the material transitioning from the thermally unstable phase to the cold phase. This is the typical length scale of the TI-driven large-scale stable structures. By 23.58 Myrs (Fig. 3.3g) the cloud has settled to a state that is typical of a two-phase medium formed due to the TI, which is seen to form in all hydrodynamic scenarios in WPFVL16. It is important to note that this spatial distribution and growth rate of clumps are characteristics of the TI, which are not affected by the spherical nature of the cloud or any edge effects. Isolating only the cloud material on the grid and analysing the total mass fraction of gas occupying the different thermodynamic regimes reveals that at 23.58 Myrs approximately $\sim 60\%$ of the material is in cold and dense clumps ($T < 160\,\mathrm{K}$) with ~ 35 % of the material still unstable ($160 < T < 5000\,\mathrm{K}$) located in a thin layer around the clumps. The majority of the volume is occupied by warm gas ($5000\,\mathrm{K} < T < 10\,000\,\mathrm{K}$), however this accounts for only $\sim 5\%$ of the mass.

Panels (i – l) in Fig. 3.3 show the final evolutionary stages of the collapse. By 28 Myrs the cloud has shrunk to a radius $\sim 20\,\mathrm{pc}$. At this point, gravity is dominating over the TI in the evolution of the internal structures as the cloud is now accelerating rapidly at the edges, and as it collapses the outer clumps collide and merge with many of the inner clumps. This accelerates the growth of the maximum density which exceeds $1000\,\mathrm{cm}^{-3}$ by 30 Myrs. By 32.42 Myrs (Fig. 3.3k) there is residue of the thermal instability formed clumps near the centre of the cloud, and the now 10pc radius cloud contains a cold and dense canopy all around the edges. This period is very short lived as by ~ 35 Myrs (Fig. 3.3l) the whole cloud has collapsed to a single core with radius 5pc containing $\sim 17\,000\ \mathrm{M}_\odot$ of material.

Fig. 3.4 shows snapshots of the evolution of the pressure-density mass dis-

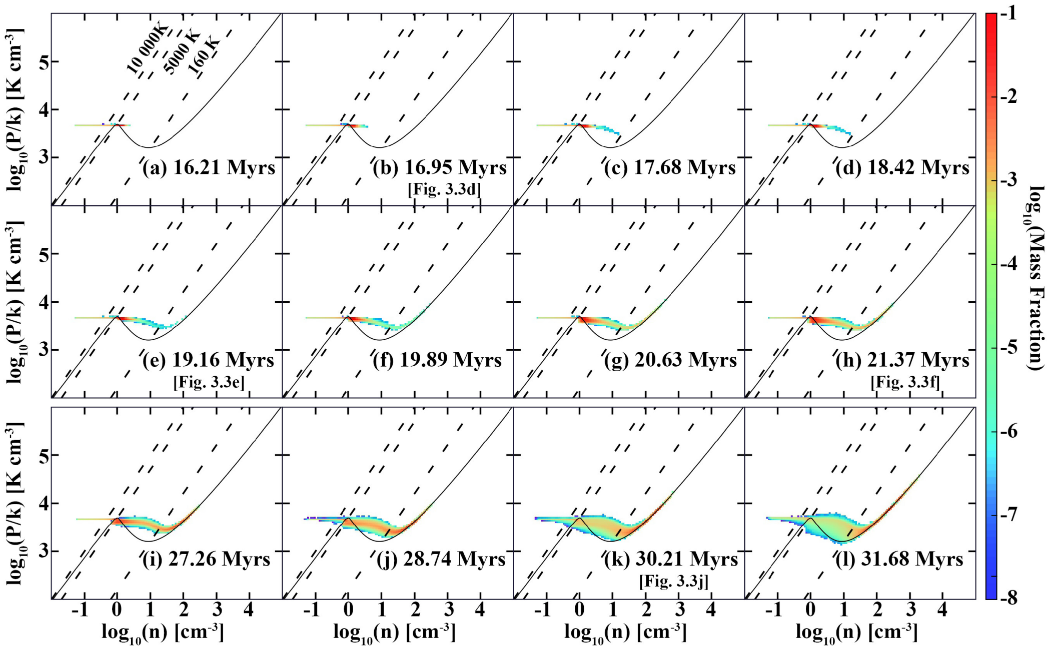

Figure 3.4: Mass distribution in pressure-density space from the moment of phase transition to a two-phase medium. Panels (i−l) show the final stages of evolution as the cloud experiences global gravitational collapse. Temperatures that distinguish the different equilibrium phases with isotherms that mark the hot phase (10 000 K $<$ T), warm phase (5000 K $<T<$ 10 000 K), unstable phase (160 K $<T<$ 5000 K) and cold phase (T $<$ 160 K). The corresponding panels in Fig. 3.3 are referenced in square brackets where applicable.

tribution imposed over the pressure equilibrium curve. Isotherms are shown to distinguish between the hot, warm, unstable and cold phases. It is important to note that only material lying on the equilibrium curve can be considered to belong to a phase, otherwise it is simply transitioning within a regime or between phases. Any gas that does not lie on the equilibrium curve but is found in a temperature regime is explicitly referred to as that regime's material, e.g. unstable *material*, which lies in the unstable temperature range but is not on the equilibrium curve.

Little change is seen in the gas state between $t = 0$ (Fig. 3.1b) and 16 Myrs (Fig. 3.4a) where we can see the majority of the gas in the cloud is still located in the unstable phase. Note that we have a smoothed cloud interface, which is responsible for the distribution of material seen in Fig. 3.4(a). On this timescale however, even clouds that start off with sharp edges develop a smoothed edge due to the solver distributing discontinuities over a number of grid cells. Although little change since $t = 0$ is seen in Fig. 3.4(a), it does capture the first hints of the phase transition due to the TI. In Fig. 3.4(a – c) material is seen to migrate across the phase diagram and by 18.42 Myrs there is a fraction of cold material settling into the cold phase. This is reflective of the timescale of the TI and the formation of the first clump. Following this we see the migration of more unstable material into the cold phase, which manifests as an increase in the number of clumps and mass in individual clumps. This behaviour continues throughout the cloud until $t \approx 29$ Myrs. Fig. 3.4(k) is when we start to observe the effects of the merging and coalescence increasing the maximum density, with gravity keeping the structures bound together. At $t \approx 32$ Myrs (Fig. 3.4l), 95% of mass is now contained in the cold phase with remaining material being warm and unstable, the gravitational collapse of the whole cloud follows.

Two behaviours are important to note from the phase diagrams. The first is the migration of the unstable material into the cold phase as seen in Fig. 3.4(a –

c). This type of transition is the precise signature of the TI when viewed on a pressure-density phase diagram. If a shock is introduced into a simulation prior to this, and shocked gas cools into the unstable phase it is then susceptible to the TI (e.g. Van Loo *et al.*, 2010). If it consequently follows this trajectory, one can conclude that the shock has successfully triggered the TI (e.g. Inoue & Inutsuka, 2009, 2016). The second thing to note is that in isolation with no other influences, the final state of the TI from this initial condition can produce maximum cold densities of $100\,\mathrm{cm}^{-3}$. Gravity and cooling changes these slightly, however the persistence of the mass distribution as seen in Fig. 3.4(h,i) represents what can be considered the final established state of the TI. We briefly highlight the spread of the distribution seen first to occur between Fig. 3.4(h/i). This is partly due to the changing of the Riemann solver from Godunov to Kurganov-Tadmor, which temporarily reduces the maximum density on the grid and diffuses the sharply peaked density profiles of the clumps. The two-phase structure is not strongly affected by this, however large deviations from this distribution means the development of a different environment that may not closely resemble a two-phase medium. The existence and deviations of such behaviour are some of the things examined in our shock-cloud interactions, which we now turn to.

3.3.2 Scenario 2 - *12Shock*

3.3.2.1 Dynamics and Morphology

The evolution of the cloud in the *12Shock* scenario is illustrated with density slices in the $x-y$ ($z=0$) plane in Fig. 3.5.

Immediately prior to introducing the shock, the cloud has not experienced any significant changes. It has not yet contracted, its density, pressure and temperature are almost uniform and almost all of the gas is in the thermally unstable phase where it would have remained for another 4 Myrs if undisturbed (as seen

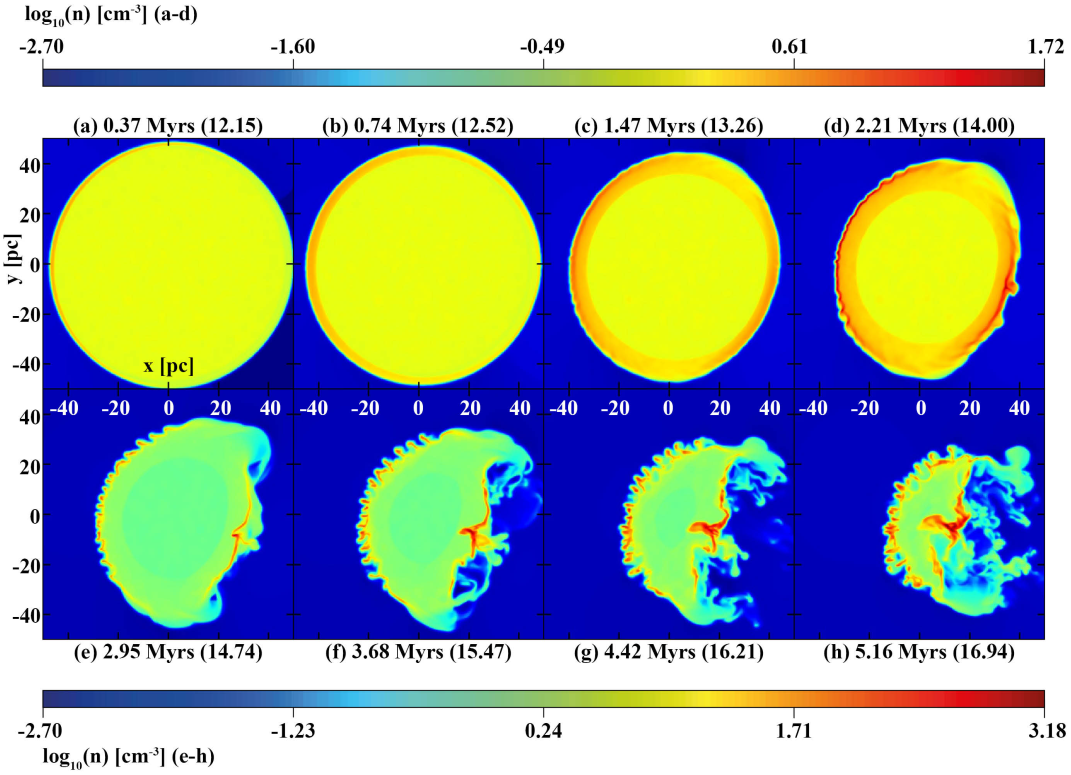

Figure 3.5: Slices through $z = 0$ of model *12Shock* evolving over a period of 5.16 Myrs taken every 0.74 Myrs. The logarithm of the number density is shown with a separate colour scale for panels a-d and e-h. The time shown first is the time elapsed since shock introduction, t - t_{shock} ($t_{\mathrm{shock}} = 11.78$ Myrs), and the time shown in brackets is the time since $t = 0$.

in Fig. 3.4a). Initially, therefore, the behaviour has characteristics common to the shock-cloud interactions seen in many works and can be effectively described as having a constant density contrast of 500 and an analytical cloud crushing timescale $t_{\rm cc} \approx 4.6$ Myrs. Note that while the transmitted shock cools and therefore slows down, it is seen to converge in the cloud centre prior to the snapshot at 5.16 Myrs (Fig. 3.5h), which is of the order of the analytically calculated value of $t_{\rm cc}$.

The external shock has a velocity of 240 $\rm km\,s^{-1}$ and crosses the cloud in less than 0.45 Myrs. During the passage of the external shock, a bow wave is reflected back into the external medium and a shock is transmitted into the cloud. In this scenario, $t_{\rm cc}/t_{\rm sc} \sim 10$ so the transmitted shock propagates much slower than the external shock. The external shock is diffracted as it sweeps over the cloud causing it to lose strength. Swept up material is therefore raised to a lower pressure. This results in a weaker transmitted shock further down the cloud which can be seen in the decrease of the initial density jump on the sides in Fig. 3.5(b) when compared to the initial density jump on the front face of the cloud in Fig. 3.5(a). Consequently, the cloud size is mainly reduced in the direction parallel to the distant upstream flow velocity. The ram pressure of the external flow accelerates this process. When the external shock converges on the symmetry axis behind the cloud, a strong pressure increase occurs which drives a shock into the back of the cloud. The consequences of this are seen after 1.5 Myrs in Fig. 3.5(c) where the transmitted shock is clearly visible within the entire cloud with higher densities at the back and front when compared to the sides. This results in a cloud that is increasingly oblate.

At the front of the cloud, the transmitted post-shock gas cools on the order of a cooling timescale ($t_{\rm cool} \approx 1.5$ Myr) forming a dense shell near the cloud interface. As the shell's internal energy is radiated away, its pressure drops and so it is further compressed making it susceptible to various dynamical instabilities. For example, the acceleration of the cloud by the post-shock gas triggers the Rayleigh-Taylor (RT) and Kelvin-Helmholtz (KH) instabilities. The RT instability in general arises as a consequences of pressure and density differences between colliding flows or within static stratified media, and hence here is most disruptive on the front face of the cloud. At 2.21 Myrs (Fig. 3.5d), regions in the shell are seen to accelerate at different rates resulting in larger, more distinct perturbations. These grow to resemble RT "fingers" which distort the shell and make it susceptible to more unstable behaviour. Between 3 – 4 Myrs (Fig. 3.5e – f) these distortions have grown so large that the instability now resembles the Vishniac instability (Vishniac, 1983; Michaut *et al.*, 2012), strikingly similar to what was witnessed by Pittard *et al.* (2003) in an expanding SNR in an AGN environment.

The KH instability is most disruptive in regions with large velocity shear, which in this work is on the edges of the cloud. Where there is shear, small scale perturbations are amplified to lateral and vertical motions that form locally circulating eddies that disrupt the cloud. At the rear of the cloud, the velocity shear results in the formation of a powerful poloidal flow with a low pressure core, which redirects the external stream adjacent to the cloud towards the back of the cloud. This results in a vortex ring with a complex velocity field that traps hot circulating low density gas and induces strong turbulent motions causing mixing of cloud and ambient material. This flow warps the outer edges of the rear-facing shell and amplifies the compression of the already convergent flow. This strongly affects the morphology of the shell which in the density slices is seen as a winged-like structure with a protruding needle at the centre, where the flow is most focused. The growth of this structure is seen most clearly in Fig. 3.5(e – h) where the strong pressure jump and converging flow induces velocities of up to 13 $\mathrm{km\,s^{-1}}$ in the needle, forcing it to grow in contrary motion to the 1.8

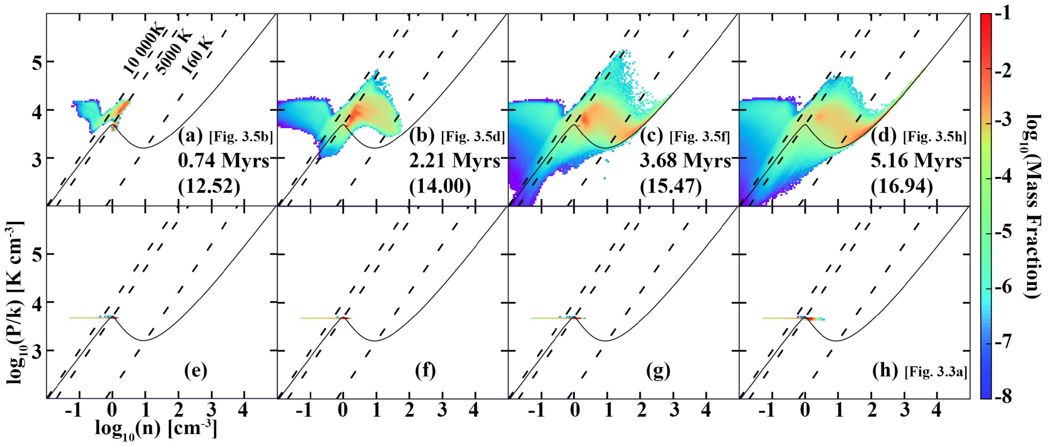

Figure 3.6: Top panels: Phase diagrams for model *12Shock* over a period of 5.16 Myrs taken every 1.48 Myrs. Bottom panels: Phase diagrams for the corresponding snapshots in model *NoShock*. Logarithmic mass-weighted mass fractions are shown. The first time shown corresponds to elapsed time since shock introduction, t - t_{shock} ($t_{\text{shock}} = 11.78$ Myrs), and the time in brackets is since $t = 0$. The corresponding density slices in Fig. 3.5 (Fig. 3.3 where applicable) are referenced in the square brackets. Isotherms delineating the hot (10 000 K $<$ T), warm (5000 K $< T <$ 10 000 K), unstable (160 K $< T <$ 5000 K) and cold ($T <$ 160 K) regimes are shown.

km s^{-1} motion of the centre of mass of the cloud. This is also faster than the transmitted shock velocity of 10.6 km s^{-1} and while not apparent in the colour scale used here, the needle overshoots the transmitted shock by Fig. 3.5(g). By Fig. 3.5(h) the cloud appears hemispheric with a curved front and a flattened back. The exterior contains multiple clumps and dense structures with a needle like protrusion nested at the rear. The base of the needle contains a high density core with $n = 1.51 \times 10^3$ cm^{-3}.

3.3.2.2 Phase evolution

The evolution of the mass weighted pressure-density distributions are shown in Fig. 3.6. Panels (a – d) show the distributions for the *12Shock* scenario which are contrasted against the distributions of the *NoShock* scenario in panels (e – h) for the same instances in time. The rich complexity of the interaction is indeed reflected in the plots. Initially gas is seen to be shocked off the equilibrium curve increasing the amount of warm gas in the cloud. The full range of compression is captured, reflecting the variation of the strength of the transmitted shock across the cloud. The peak of the compression corresponds to regions in the front of the cloud where the transmitted shock is the strongest and gas cools the fastest. This gas loses much of its internal energy and thus is susceptible to further compression. This causes a significant fraction of unstable material to transition to the cold regime.

One focus of this work is to examine the interplay between the shock-dominated effects and the TI. In this scenario, two things are important to highlight. When the shock is first transmitted, it compresses the material such that it begins to cool rapidly. This results in rapid compression and material is seen to completely pass through the unstable regime. During this transition, it is not actually evolving due to the TI but radiative cooling. As mentioned in Section 3.1, the trajectory of the TI across the equilibrium curve is very distinct and evolves almost isobarically, which is not the case in this simulation. There does appear to be a possibility of re-triggering the TI, with some shocked gas transitioning, or remaining close to the unstable equilibrium curve. If this material was to settle in the unstable phase, it would again become subject to the TI. However following the convergence of the transmitted shock at the centre of the cloud on the cloud crushing timescale (Fig. 3.5f – h), all gas in the unstable phase gets shocked out of equilibrium. This gas is found where the transmitted shock was the weakest on the edges of the cloud. Therefore a weaker shock and a delayed cloud crushing would aid the development of the TI. A weaker shock could be achieved if the initial Mach number is lower, or if magnetic fields are present (e.g. Van Loo *et al.*, 2010). A larger cloud like that of WFP19 would delay cloud-crushing. The most effective shocks in triggering the thermal instability are those where the density of the final state is on the unstable part of the equilibrium curve. For an initial upstream density of $n = 0.1$ cm^{-3}, Falle *et al.* (2020) show the path of an oblique MHD fast shock in their fig. 7 which achieves precisely this. See also discussion in their section 3.3 and further examples of such shocks in their table 1.

Densities greater than 1000 cm^{-3} are seen 4.42 Myrs into the evolution of *12Shock*. Contrasting this with the values seen in *NoShock*, densities greater than 1000 cm^{-3} are first seen $\sim$ 28 Myrs into the evolution and $\sim$ 15 Myrs later than in the *12Shock* scenario. Note that since the state of the cloud in model *NoShock* is effectively the same over the first 15 Myrs of evolution, introducing a shock at any time during this period will result in the same interaction as *12Shock*. This means that densities of $\sim$ 1000 cm^{-3} could have been witnessed as much as 25 Myrs prior to what is seen in the *NoShock* scenario had we decided to introduce the shock at $t = 0$, for example. This long period of quiescence means that the likelihood of this type of interaction taking place in the ISM is therefore relatively high. In this scenario, the TI does not play as much of a role as the shock and gravity do. However, the cooling processes responsible for the TI are fundamental in this interaction.

3.3.2.3 Local and global collapse of 12Shock

We now discuss the state of the clumps that have formed in the context of star formation, compare this to what we see in the unshocked scenario *NoShock*, and present evidence for local gravitational collapse. The evolution presented in the previous section ran to its resolution limit and to study any further evolution would require additional levels of AMR. WFP19 performed higher resolution simulations of a smaller portion of a larger cloud, one of which was focused on the gravitational collapse of an individual clump. This clump witnessed a

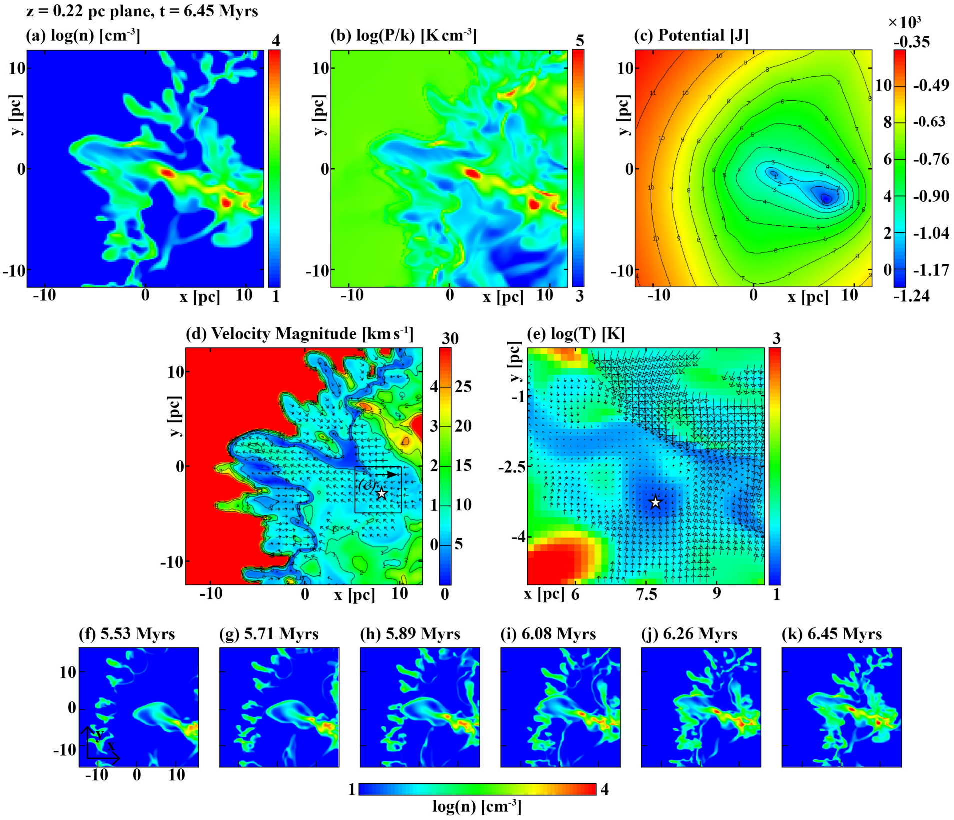

Figure 3.7: Shown are snapshots of a collapsing clump in the *12Shock* scenario at $t = 6.45$ Myrs. The slice is through the region of maximum density ($z = 0.22$ pc). Shown are (a) density, (b) pressure and (c) gravitational potential. Panel (d) shows magnitude of velocity. Velocity vectors are shown only for gas in the cold ($T < 160\,\mathrm{K}$) regime scaled to $v = 10.84$ km s^{-1}, the highest velocity in the region constrained by the temperature. Panel (e) shows a region zoomed in on the collapsing core with velocity vectors in the frame of the clump for the coldest ($T < 50\,\mathrm{K}$) regions showing a converging velocity field. Velocity vectors are scaled by the largest velocity in this region which is $v = 6.12$ km s^{-1}. Panels (f−k) show the density evolution up to that point.

rise of density and pressure by two orders of magnitude in $\sim 10^5$ years. To track the entirety of this behaviour in our shocked clouds, would require at least an additional 4 levels of AMR to increase the resolution from $\Delta x = 0.29$ pc to $\Delta x = 0.018$ pc as was done to capture the final collapse in WFP19. This would be extremely computationally intensive, so we choose to only add a single extra level of AMR and evolve slightly further. To discuss the differences between the structures that form, we follow the definitions summarised in table 1 of Bergin & Tafalla (2007) unless stated otherwise.

Prior to a cloud-crushing timescale of $t_{\rm cc} \approx 4.6$ Myrs, the cloud has formed a hemispheric, turbulent-like exterior which at the front face of the cloud fragments into structures that experience a density increase from $n = 1.1$ cm^{-3} to $\sim 200-1000$ cm^{-3}. In terms of mean density, size and velocity extent, these have properties typical of Bergin & Tafalla clouds. They do however fall on the lower end of the range of cloud sizes, with most structures having radii of $\sim 1-4$ pc, which falls closer to Bergin & Tafalla clumps. Their temperatures, crossing times and masses also agree with this definition. The larger clumps contain various substructures and appear to be coalescing with their neighbours. However their densities fail to grow much further beyond 1000 cm^{-3} and the clumps are not seen to collapse under gravity.

At 6.63 Myrs we find densities greater than 10^4 cm^{-3} and turn our attention to the structures containing them. The origin of these structures is witnessed earlier of course, as they are located at the base of the protrusion shown in Fig. 3.5(f). In terms of sizes, masses and velocities, these structures continue to have properties that can be characterised as clumps. They now also fit the clump category according to their mean density, although the highest densities suggest that they are evolving into cores. In Fig. 3.7 we show a snapshot of two of the clumps at this instance in time, 1.3 Myrs of evolution after Fig. 3.5(h).

Evolution of this region up to this point is shown in Fig. 3.7 panels (f−k). The slices presented are through the plane $z = 0.22$ pc which cut through the location of maximum density which is $n = 1.34 \times 10^4$ cm^{-3} in the final snapshot; it is marked with a star on the velocity plot in Fig. 3.7(d). We zoom in on this region in the temperature plot in Fig. 3.7(e) and show locally converging velocity vectors in the frame of the collapsing clump. Note that velocity vectors in Fig. 3.7(d) are shown for cold material ($T < 160\,$K), whilst in Fig. 3.7(e) we only show them for the coldest ($T < 50\,$K) regions.

From the evolution snapshots in Fig. 3.7(e−j), we see that the clumps are contained within the protrusion-like structure which is moving upstream at ~ 8 km s^{-1} against the 90 km s^{-1} post shock flow. One clump follows the motion of the needle and is seen to develop a local potential minimum. The second clump remains confined at the base of the potential well, but is accelerated upstream by the converging flow along with the material at the back and sides of the cloud. Its center of mass has a velocity of 6.4 km s^{-1} and its internal velocity dispersion is ~ 1.4 km s^{-1}. At the front of the protrusion, a bow shock has formed which punctures through the front shell in Fig. 3.7(k) and disrupts structures contained in the shell. While we notice regions get compressed and become over-pressured, on these timescales and at this resolution, this interaction does not cause any structures in the shell to collapse.

We focus therefore on the fastest collapsing clump marked by the star. Williams *et al.* (1995) found that in the Rosette Molecular Cloud, CO traced clumps have an average H_2 number density of $n \approx 220\,\mathrm{cm}^{-3}$, excitation temperatures $T < 20\,$K and thermal gas pressures $P/k \approx 2500\,\mathrm{K\,cm}^{-3}$. For our analysis we therefore isolate a spherical region centered on the maximum density with a radius set by inspection, and only trace material for $n > 220\,\mathrm{cm}^{-3}$, $P/k > 2500\,\mathrm{K\,cm}^{-3}$ and $T < 20\,$K. For the clump under consideration, our radius of choice is 0.75 pc, which traces slightly over the total volume of the clump, and the other constraints ensure that effectively only molecular material is considered. We note that due to the low resolution, the location of the potential minimum, maximum density and the centre of mass of the core are all displaced by only a few cells, thus a decision to use any of them as the centre around which to define our region would effectively yield identical results.

We find that the clump contains $\sim$ 140 $\mathrm{M}_\odot$ of material and has a mean density of $n \approx 2.8 \times 10^3$ cm^{-3}. It has central temperatures of $\sim$ 12 K and is over-pressurised with respect to the surroundings by almost 2 orders of magnitude. In the frame of reference of the clump, the surrounding velocities are converging and an energy analysis reveals it to be Jeans unstable ($|E_{\mathrm{grav}}| > 2E_{\mathrm{therm}}$) and gravitationally bound ($E_{\mathrm{grav}} + E_{\mathrm{kin}} + E_{\mathrm{therm}} < 0$). The density threshold for star particle creation as set by Truelove criterion is 1.1×10^4 cm^{-3}. As this has been exceeded and the usual tests for star particle algorithms have been passed (e.g. Federrath *et al.*, 2010), the clump could now have been converted to a star.

Since densities typical of molecular clouds were seen $\sim$ 2 Myrs into the simulation, we conclude that the lifetime of our starless cloud, and therefore timescale for star formation, determined by the first signs of gravitational collapse is $\sim 3-5$ Myrs. The application of a robust star particle algorithm to fully determine the star formation rates and efficiencies, and to study the feedback of those stars into these clouds, will be left for future work.

3.3.3 Scenario 3 - *24Shock*

3.3.3.1 Dynamics and Morphology

The evolution of the cloud in the *24Shock* scenario is illustrated with density slices in the $x-y$ $(z=0)$ plane in Fig. 3.8(a$-$h). Contrasted against the entirety of *NoShock* we show the maximum density in Fig. 3.10(a) and the fractions of

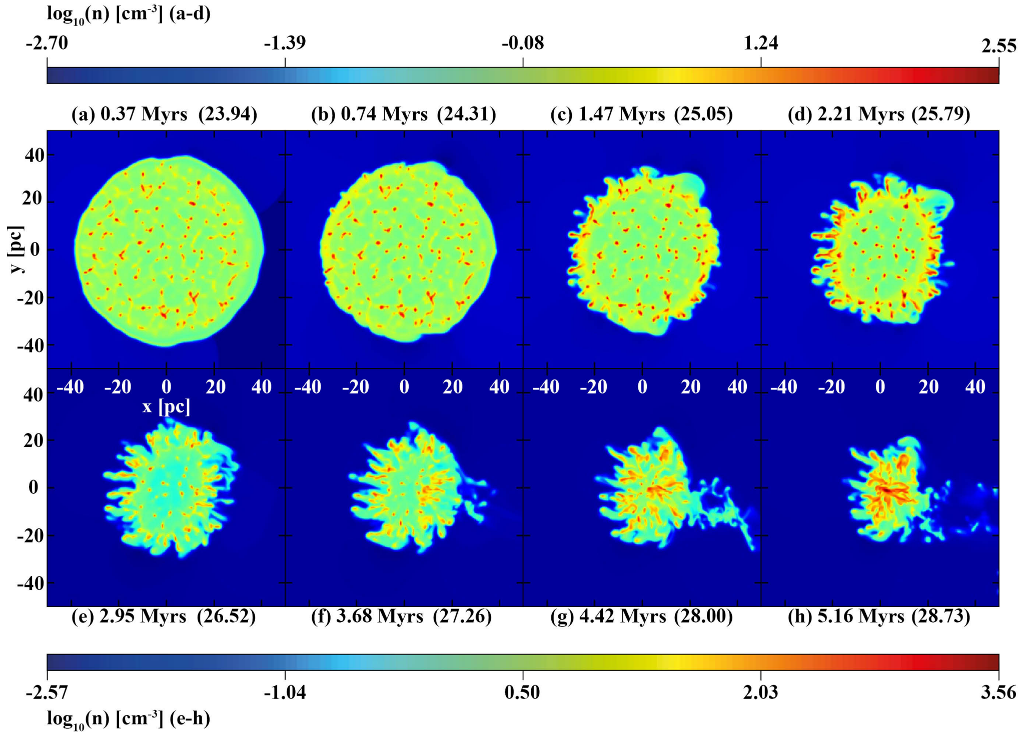

Figure 3.8: Shown are slices through the $x-y$ $(z=0)$ plane of model *24Shock* evolving over a period of 5.16 Myrs taken every 0.74 Myrs. The logarithm of the number density is shown with a separate colour scale for panels a–d and e–h. The time shown first is the time elapsed since shock introduction, t - t_{shock} ($t_{\text{shock}} = 23.58$ Myrs), and the time shown in brackets is the time since $t = 0$.

material in the different regimes in Fig. 3.10(b) where the numbers account for both equilibrium and out of equilibrium material. In this scenario the cloud has been allowed to evolve undisturbed for 23.58 Myrs. Over this period it has formed a two-phase medium due to the effects of the TI, namely a complex of cold and dense clumps embedded in a warm diffuse inter-clump gas, which is itself embedded in a hot rarefied medium. The nature of the interaction is very different to *12Shock*. Now each dense clump acts like its own individual cloud, effectively resulting in multiple shock-cloud interactions. The global interaction is dominated by the sum of these. This means that the global evolution deviates strongly from a typical shock cloud interaction as the transmitted shock is distorted by the clumps and the development of the Vishniac, RT and KH instabilities are suppressed. These instabilities would likely be present on the individual clumps but they are not adequately resolved in these simulations.

In Fig. 3.8(a) the shock has swept over most the cloud and a transmitted shock is faintly seen. As there are no clumps exactly on the edges of the cloud (i.e all clumps are surrounded by an envelope of warm gas) the shock that they initially interact with is not the external shock, but the transmitted inter-clump shock. The interactions are different from clump to clump, as the transmitted shock enters regions of varying density and density contrasts between the clump and interclump gas. The subsequent structure of the shock is then affected, as it loses energy as it propagates through the cloud and is distorted by the previous clumps it interacts with.

The cloud experiences considerable disruption much earlier than the one in *12Shock*. As the cloud is more porous, the shock moves more rapidly through the low density inter-clump material and accelerates the clumps as it does. The denser clumps are more resistant and are accelerated more slowly. As a result, they get left behind and become entrained in the low density external flow. The shocked inter-clump material cools and forms a dense shell, with dense hubs occupied by the pre-existing clumps. Some clumps are seen to break off as early as ~ 1.5 Myrs (Fig. 3.8c) and become entrained in the external flow. Inner clumps then become entrained in the shocked inter-clump flow, and all embedded clumps form elongated tails that are directed radially inward. The tails of the clumps inside the cloud become exaggerated when the external flow channels the lower density inter-clump material further into the cloud, exposing more inner clumps to the external flow.

As clumps are accelerated less than the inter-clump gas, channels form from all sides of the cloud which play an increasingly important role in redirecting the external flow. Since the inter-clump gas is less resistant to the flow, and the initial cloud is smaller than *12Shock* at shock introduction, the shock can propagate faster through the cloud than in the *12Shock* scenario. As a result, the cloud-crushing timescale is shorter, and the transmitted shock converges at the centre of the cloud ~ 3.7 Myrs into the interaction (Fig. 3.8f). Overall this results in turbulent-like dynamics. However, there is still large-scale order to the flow.

Flow meeting the cloud at the sides now gets redirected upstream and meets the flow coming in from the rear. This flow is better able to accelerate the high density clumps with some accelerating directly along a collision path. Such collisions result in the formation of an over-dense region in Fig. 3.8(g) which becomes the location of the highest density in the cloud. This region continues to gain bulk momentum and in Fig. 3.8(h) it is seen to be confined to a clump at the centre of the cloud. Densities in excess of $\sim 3000\,\mathrm{cm}^{-3}$ are now located in this clump meaning that gravity is taking over its evolution.

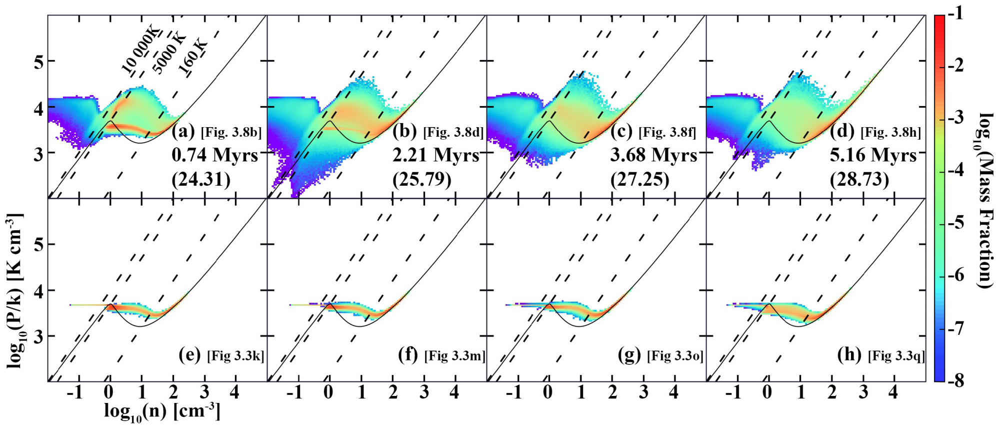

Figure 3.9: (a – d): Phase diagrams for model *24Shock* over a period of 5.16 Myrs taken every 1.48 Myrs. (e – h): Phase diagrams for the corresponding snapshots in model *NoShock*. Logarithmic mass-weighted mass fraction are shown. The first time shown corresponds to elapsed time since shock introduction, $t - t_{\text{shock}}$ ($t_{\text{shock}} = 23.58\,\text{Myrs}$), and the time in brackets is since $t = 0$. The corresponding density slices in Fig. 3.8 (/3.3) are referenced in the square brackets. Isotherms delineating the hot ($T > 10\,000\,\text{K}$), warm ($5000\,\text{K} < T < 10\,000\,\text{K}$), unstable ($160\,\text{K} < T < 5000\,\text{K}$) and cold regimes ($T < 160\,\text{K}$) are shown.

3.3.3.2 Phase evolution

Fig. 3.9 shows the evolution of the mass weighted pressure-density distributions, where panels (a – d) show the distributions for the *24Shock* scenario and (e – h) for the *NoShock* scenario for the same instances in time. From Fig. 3.9(a) the first thing to note is that material with densities $n \approx 1.1\,\mathrm{cm}^{-3}$ respond the strongest to the introduction of the shock. This corresponds to the shocking of the interclump material, and the distribution reflects the full range of compression it initially experiences. When out of equilibrium, the material subsequently behaves very similarly to the *12Shock* scenario as it migrates from the unstable regime to the cold phase. This reflects the formation of the interclump shell that connects the outermost clumps. Compared to *12Shock*, shocked material is much more widely distributed within the regimes, with most of it out of equilibrium and cooling to the cold phase. This distribution of material is aided by the shocking of the thermally unstable layers on the edges of clumps, which significantly disrupts the distribution of the characteristic two-phase medium seen to prevail in the *NoShock* scenario.

By 3.68 Myrs (Fig. 3.9c), this distribution has disappeared completely due to the transmitted shock converging at the centre of the cloud, and almost all material is out of equilibrium and cooling into the cold phase. By Fig. 3.9(d), most of the material is concentrated in the cold phase and the maximum density is approaching $n = 10^4\,\mathrm{cm}^{-3}$ reflecting the gravity dominated evolution resulting from the collision of structures near the rear of the cloud.

3.3.3.3 Local and global collapse of 24Shock

The maximum density in the cloud at the time of shock introduction is $n = 332$ cm^{-3}. The free-fall collapse timescale for this value is $\sim$ 2.6 Myrs. Local structures do eventually collapse, though on a longer timescale of $\sim$ 5 Myrs. Note

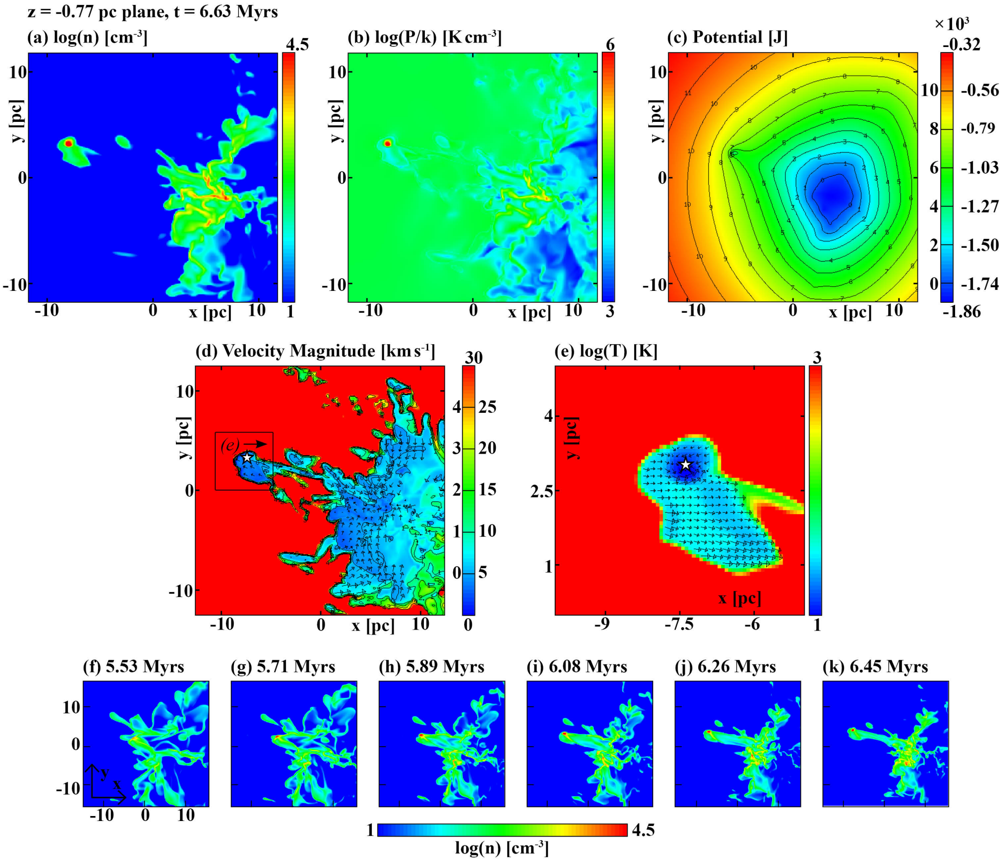

Figure 3.10: Shown are snapshots of a collapsing clump in the *24Shock* scenario shown at t - $t_{\rm shock} = 6.63$ Myrs ($t_{\rm shock} = 23.58$ Myrs). The slice is through the region of maximum density (z = -0.77 pc). Shown are (a) the density, (b) pressure, (c) gravitational potential. Panel (d) shows the magnitude of velocity with velocity vectors for gas in the cold ($T < 160$ K) regime scaled by $v = 10.31$ km s^{-1}, the highest velocity in the highlighted regions. Panel (e) zooms in on the collapsing core and shows velocity vectors in the frame of the clump for the coldest ($T < 50$ K) regions. The vectors are scaled by $v = 8.52$ km s^{-1} and show a converging velocity field. Panels (f−k) show the density evolution up to that point.

that similar behaviour was seen in WPFVL16 and WPF19, where an extended period of $\sim$ 15 Myrs was seen prior to any collapse, in spite of a free-fall time of $\sim$ 5 Myrs for $n = 100$ cm^{-3}.

From the last snapshot shown in Fig. 3.8(h), we continue the simulations with an additional 2 levels of AMR for a further 1.5 Myrs. Fig. 3.10 shows the final snapshot at 6.63 Myrs where the slices are through the $z =$-0.77 pc plane and cuts through the fastest collapsing object marked by a star on the velocity and temperature plot in panels (d) and (e) respectively. Velocity vectors and the density evolution are shown as in Section 3.2.3. There continues to be a strong asymmetry between the momentum transferred from the front of the cloud when compared to the back and sides. Flow meeting the cloud at the sides is re-directed towards the centre by pre-existing structures where it picks up an upstream velocity component due to the interaction with the converging flow originating from the rear.

We again analyse the fastest collapsing clump, which is located slightly off the central plane at the head of the most protruding structure in the cloud. We analyse material using the same criteria as in Section 3.2.3 and find that the object contains 160 $\mathrm{M}_{\odot}$ of material with a mean density of $1.47 \times 10^{4}\,\mathrm{cm}^{-3}$. It has bulk velocities $\sim 4\ \mathrm{km\,s}^{-3}$ in the ambient frame and an internal velocity dispersion of $\sim$ 1.38 km s^{-1}. Fig. 3.10(b) shows that it contains pressures in excess of $10^{5}\,\mathrm{K\,cm}^{-3}$ which are $\sim$ 1.5 orders of magnitude greater than the surroundings. With a developed local potential minimum and temperatures below 15 K, this shows clear evidence of gravitational collapse. An energy analysis additionally reveals it to be Jeans unstable ($|E_{\mathrm{grav}}| > 2E_{\mathrm{therm}}$) and gravitationally bound ($E_{\mathrm{grav}} + E_{\mathrm{kin}} + E_{\mathrm{therm}} < 0$). The density threshold for star particle creation as set by Truelove criterion in the cell with the highest density is $3.48 \times 10^{4}\,\mathrm{cm}^{-3}$ for this resolution. The maximum density in this object is $n = 7.9 \times 10^{5}\,\mathrm{cm}^{-3}$, and so this object satisfies star particle formation criteria.

The lifetime for this cloud prior to star formation is slightly longer than in *12Shock*, as we are also considering the period that established the two-phase medium due to the TI. Densities in excess of $220\,\mathrm{cm}^{-3}$ were seen $\sim$ 18 Myrs into the *NoShock* model. Since the shock was introduced at $\sim$ 24 Myrs and collapse happened 6 Myrs after that, the lifetime of the starless molecular cloud, and therefore the timescale for star-formation, is $\sim$ 12 Myrs.

3.4 Conclusion

In this chapter we present a self-consistent model of the formation of a molecular cloud out of a diffuse atomic medium evolving due to the thermal instability, gravity, and shock impact. The interactions are studied in the *small cloud regime*, such that the shock is planar and time-independent throughout the simulation. Two different times are considered for the shock introduction: when the cloud is in a “pre-TI” warm atomic state, and a “post-TI” state where cold and dense clumps have formed. The cloud is subsequently evolved until the first instances of local gravitational collapse are seen and during its evolution we study the relative importance of the shock, thermal instability and gravity. We note the following outcomes:

1. Both shock scenarios show early and sustained evidence of local gravitational collapse, successfully demonstrating their capacity for star formation. Local collapse was not seen in the unshocked clouds as in our *NoShock* scenario or WPFVL16, though more massive clouds do show local collapse in WFP19.

2. Introducing the shock whilst the cloud is atomic prevents the development of the thermal instability. Gas is shocked into the thermally unstable regime,

but cools directly to the cold phase.

3. Radiative post shock material cools to form a dense shell which fragments due to dynamical instabilities. Some fragments eventually collapse due to gravity.

4. While the transmitted shock can potentially trigger the thermal instability, this is prevented because the post shock gas that cools back to the unstable phase is repeatedly shocked on a cloud-crushing timescale. A shock interacting with a much larger cloud, like that of WFP19, would be a better candidate for witnessing shock triggered thermal instability.

5. Thermal instability formed clumps are important in determining the structure of the velocity field as external flows are directed via low density interclump channels. Inspecting the velocity field visually shows it to appear turbulent-like (see Chapter 5), with lots of un-ordered regions of flow. However, there is still some larger scale order to the flow as the majority of it is directed through the channels to the centre of the cloud and back upstream against the cloud drag.

6. When structure is already present in the cloud, the shock substantially increases the probability of clump-clump interactions. These occurrences are largely responsible for the first instances of gravitational collapse.

7. In our models the shocked molecular clouds remain starless for ~ 5 Myrs in the *12Shock* scenario and ~ 15 Myrs in the *24Shock* scenario, thus reflecting the possible lifetimes of molecular clouds prior to star formation.

In the next chapter, we perform similar studies to those in the current chapter, however now consider the *large cloud regime.*

Chapter 4

Supernova-cloud interactions in the large cloud regime

The content of this chapter is in the in-press publication titled "Shocking interactions of supernova remnants with atomic and molecular clouds - the interplay between shocks, thermal instability and gravity in the large cloud regime" (Kupilas *et al.*, 2022).

4.1 Introduction

In the previous chapter we looked at an extension of the 3D hydrodynamical scenarios in Wareing *et al.* (2016a, hereafter WPFVL16) by including a shock. The simulations were set up as a plane-parallel shock-cloud system in the *small cloud regime*, as commonly seen in the literature (e.g. Klein *et al.*, 1994; Nakamura *et al.*, 2006; Van Loo *et al.*, 2007; Pittard *et al.*, 2009; Pittard, 2011; Kinoshita *et al.*, 2021). The relative importance of the TI, gravity and the shock impact was then explored. Two shock-cloud scenarios were studied, consisting of a shock-cloud interaction with a "pre-TI" warm atomic cloud, and a "post-TI" molecular cloud consisting of cold and dense ($T \sim 50 - 160\,\mathrm{K}$, $n \sim 100 - 1000\,\mathrm{cm^{-3}}$) clumps embedded in a warm and diffuse ($T \sim 1000\,\mathrm{K}$, $n \approx 0.8\,\mathrm{cm^{-3}}$) interclump gas. In both cases, the constant impact due to the post-shock flow compressed the cloud significantly and accelerated the global gravitational collapse of the cloud. Evidence of local gravitational collapse was seen also, occurring on a $\sim 5\,\mathrm{Myr}$ timescale in both scenarios.

Positioning the shock source away from the cloud edge at $R_{\mathrm{c}} = \infty$ such that upon impact it can be approximated as time-independent and planar is characteristic of the *small cloud regime* (see Section 1.2.5.2). It is prudent therefore to investigate what happens when the shock is time-dependent and has curvature, such as characteristic of shocks in the *large cloud regime*. We do this here by replacing the shock with a supernova explosion, so that condition $r_{\mathrm{cl}} > 0.05 R_{\mathrm{c}}$ is satisfied (equation 1.16). We have $r_{\mathrm{cl}} \approx 50\,\mathrm{pc}$ and $R_{\mathrm{c}} = 50$ (pre-TI) and 70 (post-TI), placing our models firmly in the *large cloud regime*. To our knowledge, a systematic comparison between the physical behaviour of an idealised shock-cloud and supernova-cloud set-up has not yet been performed. In Section 4.2 we present details of the model, the specific scenarios studied and the computational details. In Section 4.3 we present our results, and we conclude our work in Section 4.4.

4.2 Methods

4.2.1 Numerical method

This work presents 3D hydrodynamical simulations of the interaction of a supernova remnant with a cloud in the *large cloud regime*, with the cloud initially evolving due to the thermal instability and gravity. The interactions are then compared to their analogous planar shock-cloud scenarios in the *small cloud regime* and the un-shocked scenario studied in Chapter 3. All calculations were performed using the finite-volume adaptive mesh refinement (AMR) code MG (Falle, 1991, 2005; Hubber *et al.*, 2013). The code solves the Euler equations of hydrodynamics with free boundary conditions, is second order in space and time, employs a hybrid cooling function and treats gravity by solving the Poisson equation using the full-approximation multigrid technique. For the reader interested in the details of the numerical scheme, they can be found in Falle (1991), WPFVL16 and Chapter 3. We note however that in Chapter 3 the simulations were initially ran with the Godunov (GOD) Riemann solver (Godunov, 1959) until the gradients in the domain were too high for the simulations to continue. At that point the solver was switched to Kurganov-Tadmor (KT) (Kurganov & Tadmor, 2000). In the current chapter, the KT solver is chosen from the beginning.

4.2.2 Model

In this chapter we adopt the same initial model as scenario 3 in WPFVL16 and that in Chapter 3. Namely, $17\,000\,\mathrm{M}_\odot$ of diffuse material is initialised in a sphere with radius $r = 50\,\mathrm{pc}$, which we refer to as the cloud (see figure 3.1 in Chapter 3). The cloud lies at the origin of a Cartesian domain with a numerical extent of $-3 < xyz < 3$. In our model a unit length corresponds to 50 pc, resulting in a domain with 300 pc extent on each side. 8 levels of AMR are used, with the grid fixed to maximum resolution within a sphere with radius $r = 75\,\mathrm{pc}$ centered at the origin to accurately capture the behaviour of the TI. The grid refines and de-refines dynamically outside this region, with level 5 chosen as the minimum base level. For the supernova scenarios, the region outside $r = 75\mathrm{pc}$ is then forced to be resolved down to the 5th level to manage the computational cost associated with the grid creating levels and cells as the remnant expands into regions that are of no interest to the interaction. Note that for a fully refined grid, the maximum number of grid cells would be 1024^3, however due to the AMR, $\lesssim 10$ per cent of this is used. The maximum resolution on the finest grid is $\Delta x = 0.29\,\mathrm{pc}$. A discussion of the dependence of the thermal instability on the grid resolution and our arguments as to why it is acceptably resolved in our simulations are presented in the appendix of Chapter 3 and Wareing *et al.* (2021).

The cloud is seeded on the grid scale with ± 10 per cent random density variations around $n_{\mathrm{cl}} = 1.1\,\mathrm{cm}^{-3}$ in the thermally unstable phase. The pressure for this is then $P_{\mathrm{eq}}/k = 4800 \pm 300\,\mathrm{K\,cm}^{-3}$. We note that we assume a mean particle mass of $2.0 \times 10^{-24}\,\mathrm{g}$. Just like in Chapter 3, all material in the domain is initially quiescent and the cloud is embedded in a medium with a density contrast $\chi = 50$ ($\chi = n_{\mathrm{cl}}/n_{\mathrm{amb}}$) setting the ambient medium $n_{\mathrm{amb}} = 0.022\,\mathrm{cm}^{-3}$. An advected scalar α is set to 1 in the cloud and 0 everywhere else, and heating and cooling is switched on only in regions where $\alpha > 0.9$. The value of the scalar and all the other fluid states transition monotonically between the cloud and ambient values over an interface region with thickness of ~ 5 cells. At the moment of supernova/shock injection, the surroundings are remapped to have $n_{\mathrm{amb}} = 0.0022$ and $T_{\mathrm{amb}} = 2.19 \times 10^{6}\,\mathrm{K}$ ($\chi = 500$) so that the energy source term can be switched on in the whole domain whilst the surroundings remain adiabatic due to the large cooling times of the order of $t_{\mathrm{cool}} \gtrsim 100\,\mathrm{Myr}$ at such temperatures.

4.2.2.1 Scenarios

Five scenarios are considered in this chapter: *NoShock*, *S1*, *S2*, *SN1*, *SN2*. The first three, *NoShock*, *S1* and *S2* are effectively the cases presented in Chapter 3. For self-consistency, the data from Chapter 3 was not used and instead the models were re-simulated using the KT solver for accurate comparisons to the new *SN1* and *SN2* scenarios. Just like in Chapter 3, the *NoShock* scenario follows the evolution of the initial cloud for a free-fall timescale of $t \approx 35\,\mathrm{Myr}$ without any additional disturbances. *S1* is then the *12Shock* analog, where a planar shock is introduced at 11.78 Myr into the evolution of *NoShock*. *SN1* then corresponds directly to *S1*, with the idealised planar shock being replaced by a supernova explosion introduced at the exact same time. *S2* is then the *24Shock* analog, however this time a shock is introduced at 26.5 Myr into the evolution

Table 4.1: Summary of all the scenarios studied in this chapter. The columns show the scenario name, the source of impact onto the cloud, the distance from the blast origin to the nearest cloud edge R_c, the Mach number (M) of the disturbance shock immediately upon impact, and the injection time (t_inj) of the disturbance. Scenarios *NoShock*, *S1* and *S2* are effectively *NoShock*, *12Shock* and *24Shock* from Chapter 3 which have been re-simulated for this study for self-consistent comparisons. Scenarios *SN1* and *SN2* introduce supernova explosions at the same time as the shock in *S1/S2*.

Scenario	Disturbance	R_c [pc]	M (impact)	t_inj [Myr]
NoShock	None	*N/A*	N/A	N/A
S1	Shock	∞	1.5	11.78
SN1	Supernova	50	$\approx 7^*$	11.78
S2	Shock	∞	1.5	26.5
SN2	Supernova	70	$\approx 7^*$	26.5

Due to a $10\,\mathrm{M}_\odot$ and 10^{51} erg explosion located at the polar coordinate $(r,\ \theta) = (100\,\mathrm{pc},\ 160°)$ in the $z = 0$ plane. θ is measured from the positive x axis.

of *NoShock* instead of 24 Myr. The reason for this later injection time is due to the KT solver being more diffusive than the GOD solver, causing the thermal instability to take longer to trigger in the re-simulated *NoShock* scenario. This causes the phase transition to occur ~ 2 Myr later than in Chapter 3, and as such we choose a later time for shock/supernova injection in the *S2/SN2* scenarios.

For the *S1*/*S2* scenarios, an $M = 1.5$ shock is artificially imposed on the grid and boundary cells lying within the post-shock region are fixed to the post-shock values. The shock front is located at the polar coordinate of $(r,\ \theta) = (50\,\mathrm{pc},\ 160°)$ in the $z = 0$ plane, placing the shock immediately on the cloud's edge. The angle is measured counterclockwise from the positive x-axis, and is chosen to minimise the effects of the Quirk instability, or the so-called *carbuncle phenomenon*, that can cause perturbations along the shock symmetry axis, with strongest perturbation occurring when aligned with the grid (Quirk, 1997; Elling, 2009). If R_c is the distance from the shock origin to the closest cloud edge, for our choice of parameters, *S1/S2* scenarios can be considered to have $R_\mathrm{c} = \infty$, placing them

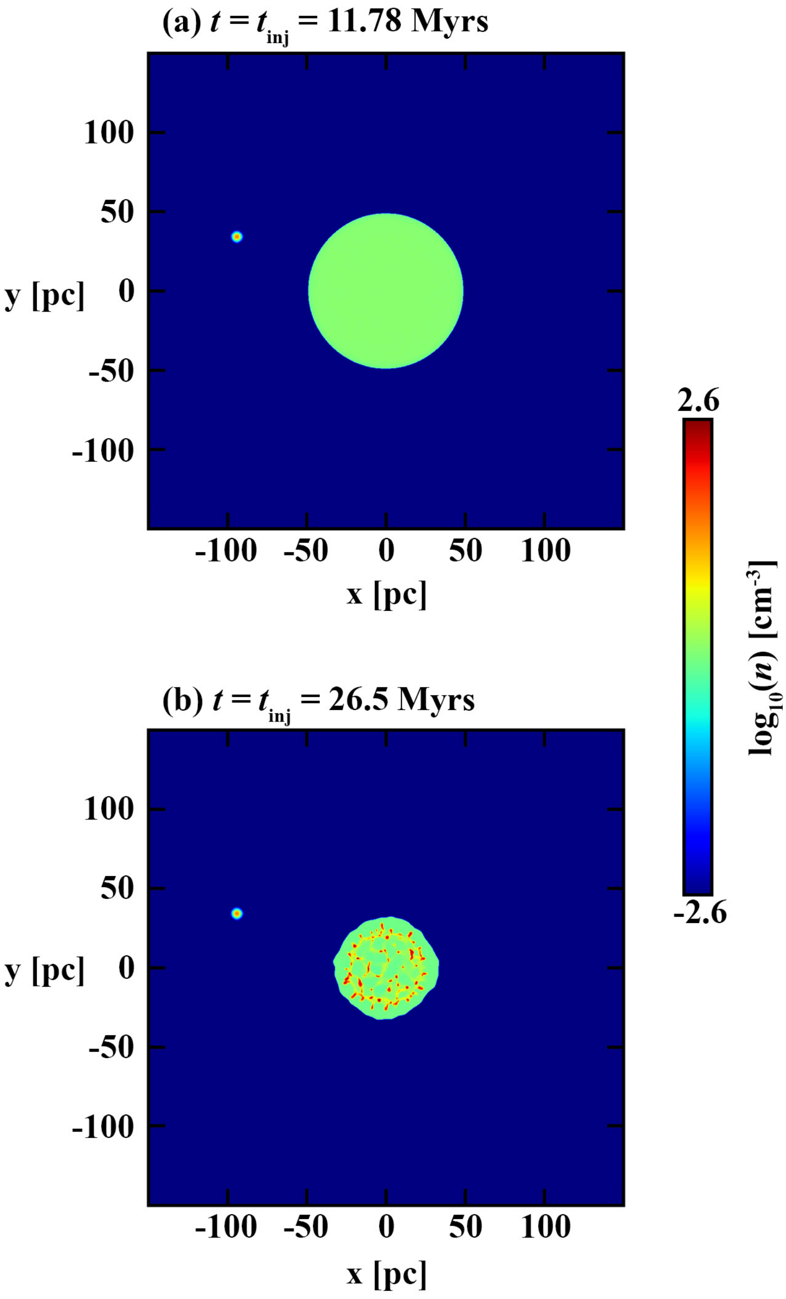

Figure 4.1: Shown are snapshots of the $z = 0$ plane of the density logarithm of (a): The cloud at injection time $t_{\mathrm{inj}} = 11.78$ Myr for *SN1/S1* scenarios and (b): Cloud at injection time $t_{\mathrm{inj}} = 26.5$ Myr for *SN2/S2* scenarios. The location of the explosion can be seen in both snapshots.

in the *small cloud regime* as initially assummed.

For the *SN1/SN2* scenarios, a supernova is injected at the polar coordinate of $(r,\ \theta) = (100\,\mathrm{pc},\ 160°)$ in the $z = 0$ plane on the grid located such that the first impact on the cloud is felt at the same location as the first shock impact in *S1/S2*. The injection volume is artificially refined to the highest AMR level and subsequently chosen to fill a region with a radius of 5 cells, i.e. 1.5 pc, into which $10\,\mathrm{M}_{\odot}$ of mass and 10^{51} erg of thermal energy are injected over a 500 yr period, roughly the time it would take for a remnant to expand to the injection volume. Note that immediately upon impact, the forward shock of the supernova remnant has $M \approx 7$. The clouds at 11.78 Myr and 26.5 Myr are shown in figure 4.1 where the region of supernova injection can also be seen. The condition $r_{\mathrm{cl}} > 0.05 R_{\mathrm{c}}$ (equation 1.16) must be satisfied for a system to qualify for the *large cloud regime*. For *SN1*, $R_{\mathrm{c}} \approx 50\,\mathrm{pc}$ which gives $0.05 R_{\mathrm{c}} = 2.5\,\mathrm{pc}$. As in this scenario $r_{\mathrm{cl}} = 50\,\mathrm{pc}$, it places this model firmly in the *large cloud regime*. For *SN2*, $R_{\mathrm{c}} \approx 70\,\mathrm{pc}$ as the evolution results in the cloud shrinking slightly due to the formation of clumps and gravitational contraction, reducing r_{cl} to a size of 30 pc. Nevertheless, $0.05 R_{\mathrm{c}}$ evaluates to 3.5 pc, also placing this model firmly in the *large cloud regime*. Thus our new models showcase interactions in two contrasting, and very different regimes, with the *large cloud regime* showing a much more realistic interaction. A summary of the model parameters are presented in Table 4.1.

4.3 Results

In this section we present our results. First, we present the *SN1* scenario and discuss the evolution outside the cloud, followed by a discussion of the internal evolution. Secondly, we present the *SN2* scenario by again looking at the external and internal evolution separately.

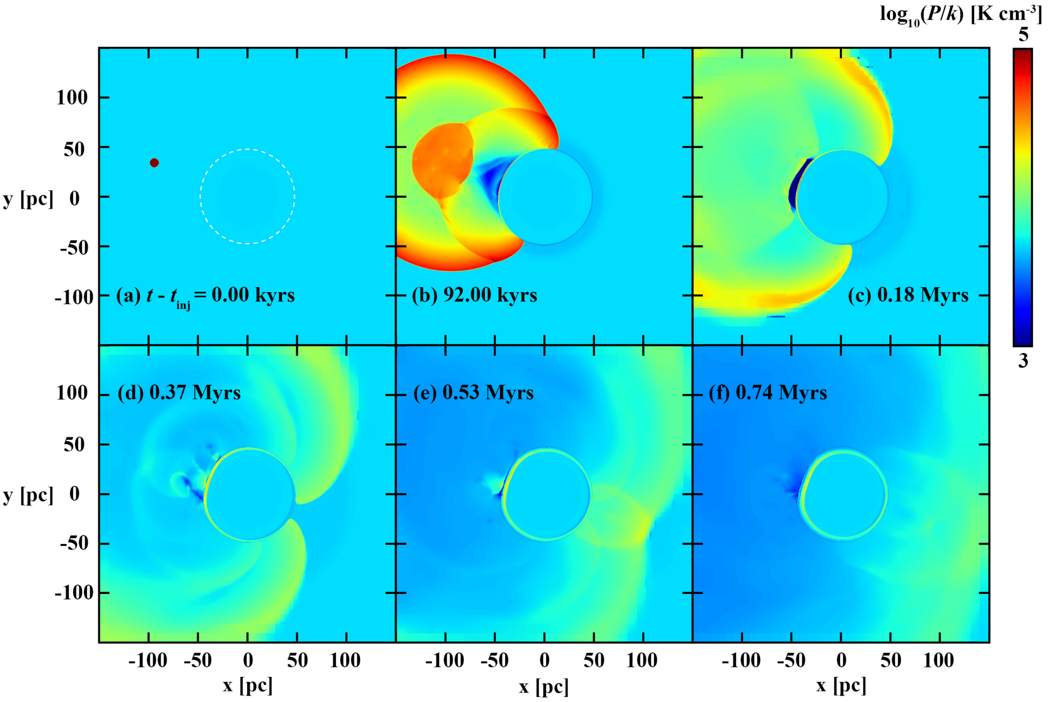

Figure 4.2: Shown are pressure logarithm plots in the $z = 0$ plane of the *SN1* scenario. The cloud edge cannot be seen initially in panel (a) and is thus marked by the white dashed line. The time in each panel corresponds to time since supernova injection $t - t_{\rm inj}$, with $t_{\rm inj} = 11.78$ Myr. The final snapshot shows the moment immediately prior to the primary shock moving off the grid, and at the time the upstream flow around the cloud is being established.

4.3.1 Interaction with atomic cloud - *SN1*

Throughout the discussion, comparisons are made to the planar shock scenario *S1*, whose detailed evolution is presented in Chapter 3. In addition, where appropriate, the *NoShock* scenario is referenced. The 5.16 Myr timescale, where we choose to stop our analysis, corresponds to the time of the first *S1* snapshot that showed evidence of local gravitational collapse.

4.3.1.1 Dynamics outside the cloud

To illustrate the external dynamics we first show in figure 4.2 the pressure profile of the domain in the $z = 0$ plane. The first 0.74 Myr are shown, as the most interesting features in the ambient medium are seen during this timescale. Figure 4.2(a) shows a snapshot immediately post supernova injection. A spherical region with a 50 pc radius centered at the origin contains 17 000 $\mathrm{M}_{\odot}$ of material, whose density is a factor $\chi = 500$ greater than the surroundings with $n_{\mathrm{amb}} = 0.0022\,\mathrm{cm}^{-3}$. A region with a radius $r = 1.5\,\mathrm{pc}$ contains $10\,\mathrm{M}_{\odot}$ and 10^{51} erg of thermal energy, and as such is strongly over-pressured with respect to its surroundings, with internal pressures exceeding $10^{10}\,\mathrm{K\,cm^{-3}}$, 7 orders of magnitude larger than the ambient pressure of approximately $4800\,\mathrm{K\,cm^{-3}}$. A powerful explosion thus follows, accelerating stationary material to speeds exceeding $10^4\,\mathrm{km\,s^{-1}}$.

Before describing the interaction, we highlight a number of noticeable numerical effects. Firstly, the cloud in Fig. 4.2(a) has a radius $r = 50\,\mathrm{pc}$, however only a smaller spherical region with a radius $r \approx 25\,\mathrm{pc}$ can be seen. This corresponds to where the internal pressure has dropped slightly due to the early action of the thermal instability. This behaviour is expected and acceptable, however we would expect to see the whole cloud behave this way. Instead what we see is a numerical effect on the boundary resulting from how the source term was initially set up (i.e. switched off for regions where the scalar $\alpha < 0.9$, with $\alpha = 1$ inside the cloud and $\alpha = 0$ outside). Material below $\alpha < 0.9$ does not cool, and as such a gradient develops starting at the interface (where $\alpha = 0.9$) from the value of the ambient pressure ($P/k \approx 4800\,\mathrm{K\,cm^{-3}}$) to the lowest value of the cloud centre ($P/k \approx 4750\,\mathrm{K\,cm^{-3}}$), and accounts for why the full cloud is not visible in panel (a). Where the edge actually is has been marked with a dashed white line. Whilst this effect is noticeable, it accounts for a maximum of 1 per cent fractional difference in the fluid variables, and does not affect the dynamics. Additionally, an outwardly propagating expansion wave can also be seen at the far side of the cloud, most clearly in panels (b) and (c). This results from the mapping of the ambient medium from $\chi = 50$ to $\chi = 500$, and amounts to a fractional difference in the fluid state of ~ 5 per cent. Again, this has little effect on the dynamics especially since these differences become overwhelmed by the supernova impact shortly thereafter.

The impact with the cloud occurs ~ 40 kyrs after explosion. At this point, $\sim 33\,\mathrm{M_\odot}$ of material has been swept up, approximately $3\times$ the mass of the ejecta, and as such the profile immediately prior to impact is Sedov-Taylor-like. The shock has a speed $v_\mathrm{s} = 1087\,\mathrm{km\,s^{-1}}$ upon impact, and given a pre-shock sound speed $c = 160\,\mathrm{km\,s^{-1}}$, this amounts to an impact shock with Mach number $M = v_\mathrm{s}/c \approx 7$, roughly a factor $\sim 4.5\,\times$ stronger than the $M = 1.5$ planar shock in *S1*. A reverse shock from the blast moves towards the epicentre with $v_\mathrm{rs} = 450\,\mathrm{km\,s^{-1}}$, and a contact discontinuity separates the forward and reverse shocks. Note that a purely analytical Sedov-Taylor profile does not have these two features - it is assummed that all waves have settled into a steady state such that a self-similar analytical solution is appropriate. In our simulations the profile behind the forward shock matches well with the analytical Sedov-Taylor profile.

The profile interacts with the cloud as the remnant passes over it, transmitting a shock into the cloud and reflecting a shock back into the ambient medium. The reflected shock propagates towards the blast epicentre, and leaves behind a low pressure void due to a trailing expansion. Meanwhile, the reverse shock from the initial blast reflects at the epicentre, and as it propagates back outwards, interacts with the cloud-reflected shock, generating an additional set of disturbances. This shock subsequently approaches the cloud and causes a secondary impact. We refer to the cloud edge where this impact occurs as the front of the cloud, the first shock as the primary shock and the second shock as the secondary shock.

Fig. 4.2(b) shows a snapshot at 92 kyrs. The primary shock has passed almost half of the cloud, and a clear distortion in its interior structure is seen in the region that interacts with the reflected shock. The primary shock diffracts around the cloud which further distorts its structure. A low pressure region ahead of the cloud can be seen, which forms due to the expansion of gas behind the reflected primary shock. The gas at the front of the cloud continues to expand during the secondary shock approach, and as such there is a strong and sharp pressure contrast between this region and its surroundings - as evident in Fig. 4.2(c) which shows the moment preceding the secondary impact. By Fig. 4.2(d) the secondary impact has occurred, resulting in turbulent eddies forming at the front of the cloud and a set of reflected waves propagating towards the left x boundary. The level of which this may seed turbulence is left to a future work. Both shocks can now be seen sweeping over the cloud too, and the primary shock has nearly converged at the rear.

By Fig. 4.2(e), the primary shock has converged and the secondary shock is trailing close behind. As the primary shock converges, an interaction region is generated with portions of the resulting waves propagating both downstream and upstream, with the upstream waves interacting with the secondary shock as it sweeps over the cloud. By Fig. 4.2(f) both shocks have passed over the cloud, and are now at the domain edge. The secondary shock has now also converged at the rear, resulting in a secondary set of waves with both downstream and upstream components. Around the edges of the cloud the upstream components generate a flow which then itself converges at the front, exaggerating the compression from the initial impact.

After Fig. 4.2(f), the ambient medium evolves due to existing pressure gradients and the remaining flows on the grid. The ambient pressure in panel (f) can already be seen to be lower than most of the cloud's edge, and this continues to drop as the model evolves. The portions of the cloud that can respond to these changes, i.e. those that have been shocked, gradually expand in an attempt to balance the ambient pressures and the post-shock pressures in the cloud. This is halted however at the front of the cloud due to the ram pressure impact of the flow that converges there. Thus the outer envelope of the cloud expands everywhere but the front, resulting in a lobe-like morphology with the front being pinched inwards.

As early as the first 1 Myr of evolution, considerable differences between the *SN1* and *S1* scenario can be seen. Two main ones can be identified however which exaggerate as the simulations evolve, and account for all of the differences seen between our shock-cloud and supernova-cloud scenarios. Firstly, for an idealised, infinitely extending planar shock, the flow behind it is continuously replenished, resulting in disruption of the cloud throughout its entire evolution. Secondly, after shock passage, the ambient pressure is relatively time-independent, i.e after the medium is shocked and its pressures exceed that of the cloud, it stays that way, and provides continuous compression. These two features are present in all adiabatic, planar shock-cloud systems, and thus a more realistic model like ours can usefully be contrasted against them.

The impact of this in our models can clearly be seen in the last snapshot at 5.16

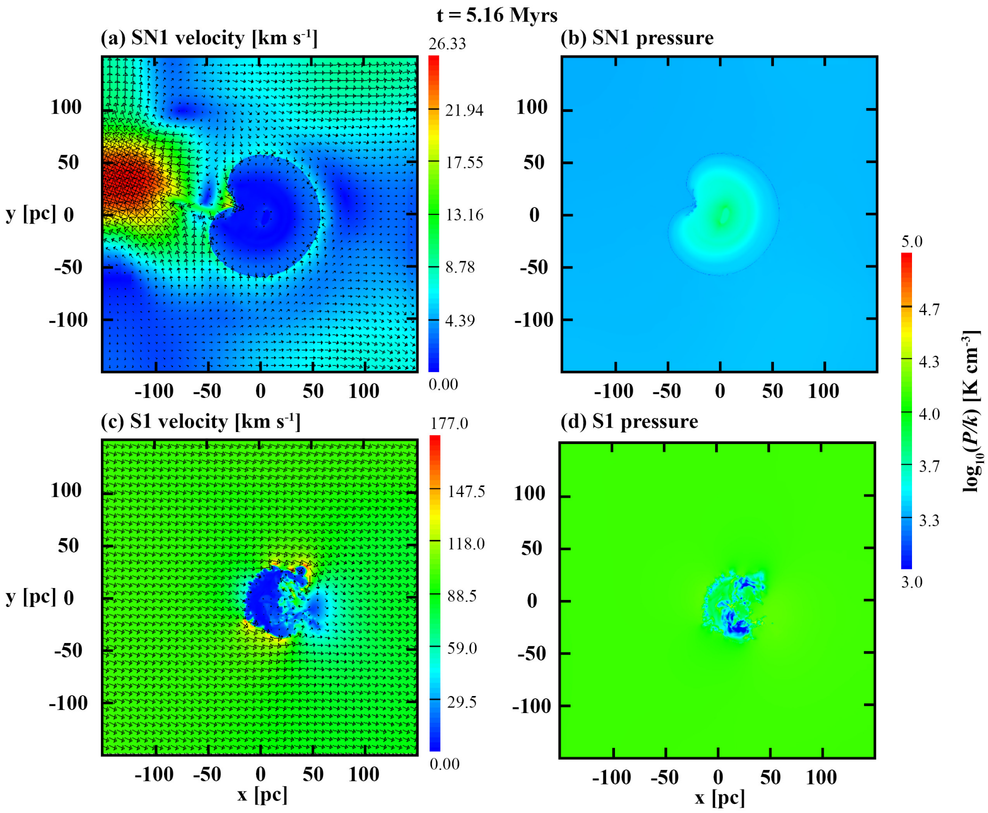

Figure 4.3: Shown are slices in the $z = 0$ plane showing the velocity (panels a and c) and pressure (panels b and d) of *SN1* (panels a and b) and *S1* (panels c and d) at $t = 5.16$ Myrs - the final snapshot presented in this work and the timescale at which the *S1* scenario witnessed local gravitational collapse.

Myrs in figure 4.3 which shows the pressure and velocity field in the $z = 0$ plane. In Fig. 4.3b the ambient thermal pressure can be seen to have decreased down to $\sim 4000\,\mathrm{K\,cm^{-3}}$, approximately 80 % of its original value of $4800\,\mathrm{K\,cm^{-3}}$. The final *S1* pressure in comparison is $\sim 10^4\,\mathrm{K\,cm^{-3}}$, a factor of 2.5 larger than the final *SN1* pressure, and has not dropped since the initial shock passage. The velocity difference is even larger, with impact amplitudes on the order of $10\,\mathrm{km\,s^{-1}}$ in *SN1* (Fig. 4.3a) and $100\,\mathrm{km\,s^{-1}}$ in *S1* (Fig. 4.3c), resulting in ram pressure impact that is ~ 100 times greater ($\rho|\mathbf{u}|^2|_{S1}/\rho|\mathbf{u}|^2|_{SN1}$, $|\mathbf{u}|^2 = u_x^2 + u_y^2 + u_z^2$) in *S1* than in *SN1*. Thus in aggregate, the supernova has a profoundly weaker compressive effect on the cloud, and is mainly responsible for creating external conditions that couple strongly to the cloud behaviour and result in cloud expansion.

We note that it is not entirely clear to what extent boundary effects impact the ambient evolution. Many waves are expected due to back and forth reflections within the remnant (e.g. Cioffi *et al.*, 1988). As seen in Fig. 4.2, the shocks move off the grid soon after 0.75 Myrs and so these reflections cannot occur. We would not however expect the fluid state to be significantly altered by their presence, and 1D spherically symmetric tests of supernova explosions with equivalent parameters as our models suggest this to be true. In fact, in our 1D tests, once the reverse shock reflects at the blast epicentre, it is unable to catch up to the forward shock to reflect backwards once more. An additional concern is the $26\,\mathrm{km\,s^{-1}}$ flows near the left x boundary. Boundary effects are likely responsible for these flows as they do not align with the spherical symmetry of the initial blast. However as they are not near the cloud and flowing off the grid, we do not expect them to affect the cloud. Finally, the internal pressure of any supernova remnant drops as it expands. As we see such a pressure drop occur in our models, we are confident that our simulations are representative of what would happen if the whole remnant was captured until the latest times considered.

4.3.1.2 Dynamics inside the cloud

To describe the evolution inside the cloud, we first show snapshots of the logarithm of the density through the $z = 0$ plane in figure 4.4. Additionally, in Fig. 4.4(i – k) we respectively compare the maximum density, fractions of material existing in warm ($10\,000 > T > 5000\,\mathrm{K}$), unstable ($5000 > T > 160\,\mathrm{K}$) and cold ($T < 160\,\mathrm{K}$) thermal regimes, and the energy partition between thermal and kinetic energies. Comparisons are drawn between the *NoShock* (black line), *SN1* (red line) and the *S1* scenarios. Here, only cloud material is traced, i.e. where the passively advected scalar $\alpha > 0.9$. Note that in our discussions, material lying on the equilibrium curve is referred to as belonging to a phase (e.g. thermally unstable phase). When talking about material within a temperature bracket (i.e. *all* material, equilibrium + non-equilibrium), we refer to this as belonging to that particular regime (e.g. thermally unstable regime).

The impact of the primary shock is felt strongest on the cloud front. As the cloud and ambient medium are initially in pressure balance, the transmitted shock has roughly equivalent strength in the cloud as it does in the surroundings, resulting in an $M \approx 7$ shock ($M = v_s/c$ where $v_\mathrm{s} \approx 50\,\mathrm{km\,s^{-1}}$ and $c \approx 7\,\mathrm{km\,s^{-1}}$) travelling into the cloud and thermalising a thin layer of material - as seen in Fig. 4.4(a). Just like for a planar shock, the cloud causes the supernova shock to diffract and reduce its strength, thus reducing the strength of the transmitted shock. Its strength is weakened further as the remnant expansion itself slows down, which is not an effect that occurs with a planar shock due to a continuously driven flow. Thus when the primary shock reconnects at the rear, much of its strength has been lost, with the convergence having little effect on amplifying the shock impact. This is in stark contrast to the *S1* scenario, where the strongest compression was seen at the back of the cloud due to the converging flow.

By Fig. 4.4(b), the shock has travelled over the whole cloud and the transmit-

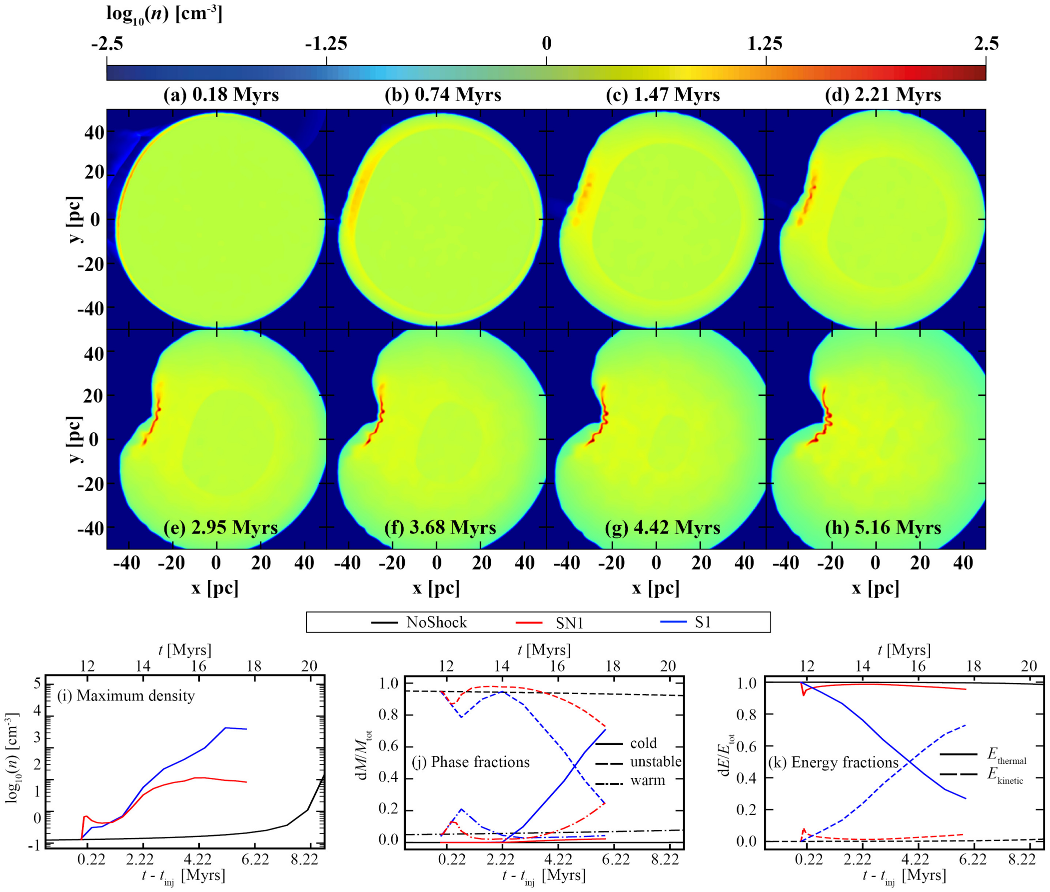

Figure 4.4: Panels (a – h) show density slices in the $z = 0$ plane for the *SN1* scenario. The logarithm of the number density is shown, and the time on each panel corresponds to the time elapsed since supernova injection t - t_{inj}, where $t_{\mathrm{inj}} = 11.78\,\mathrm{Myr}$. Panels (i), (j) and (k) respectively show the maximum density, phase fractions and energy fractions in the cloud, showing data for *SN1* (red lines), *S1* (blue lines) and *NoShock* (black lines) for direct comparison at equivalent times. Panel (j) shows mass fractions in cold ($T < 160\,\mathrm{K}$, solid line), unstable ($160 < T < 5000\,\mathrm{K}$, dashed line) and warm ($5000 < T < 10\,000\,\mathrm{K}$, dot-dashed line) regimes. Panel (k) shows the fractions of the thermal energy E_{thermal} (solid line) and kinetic energy E_{kinetic} (dashed line) out of $E_{\mathrm{tot}} = E_{\mathrm{thermal}} + E_{\mathrm{kinetic}}$ in the cloud. Gravitational energy is ignored.

ted shock is moving inwards from all sides. Where the impact was the strongest, the thermalised state experiences an increase in cooling, causing the material to be compressed by the surroundings as its temperature and pressure drops. This effect is only evident at the front of the cloud, resulting in the formation of the single cap-like structure that after $2-3$ Myrs appears filament-like in the density slices shown. The shape of this structure is distorted by the converging flow, and the pinching of the front causes the structure to accelerate faster at the centre than the sides. This is an effect more vividly seen after ~ 3 Myrs (Fig. 4.4e) and is exaggerated by the expansion of the surrounding envelope. The remaining evolution is gradual, where the cloud continues to expand and the cold structure continues to be distorted by the converging flow. The shock inside the cloud continues to slow down, and by Fig. 4.4(h) it has still not converged at the centre, in contrast to *S1* which saw the cloud shock converge on this timescale.

Many significant differences between the *S1* and *SN1* scenarios can be identified and can all be explained by this fact that the continuously replenished flow in *S1* provides constant ram pressure impact and constant thermal compression, and the remnant does not. Because of this, in *S1* the period between $1-4$ Myrs saw the formation of a cold thin shell spanning most of the cloud's edge which was continuously impacted by the incident flow. This flow distorted the shell, triggering Rayleigh-Taylor and Vishniac instabilities at the front, with the sides being distorted by the Kelvin-Helmholtz instability. Where the flow converged at the rear, the shell became winged-like, with a protruding needle forming in the centre that was subsequently accelerated against the motion of the cloud. The surrounding flow maintained high thermal pressures, and in combination with the strong ram pressure, the cloud was continuously compressed to create conditions where gravity could take over, and collapse individual structures. Whereas here, instead of a cold thin shell forming around the edges, the only cold region is found in the small layer at the front. This forms due to an instantaneous impact with no subsequent continuous flow. As such, the ram pressure is smaller by a factor of ~ 100 and thermal pressure by a factor of ~ 2.5 (see Section 4.3.1.1). None of the hydrodynamical instabilities present in *S1* are triggered, and the continuous drop in pressure means that the cloud expands rather than contracts. The only other source of compression - the secondary shock, has no effect on the material in the cold layer and only somewhat affects the warm material at the interface.

We do not expect to see star formation take place on the same timescales as *S1*. The stronger and more instantaneous impact of the supernova can be seen in the maximum density (Fig. 4.4i), subsequently followed by a rapid decline in the next 200 kyrs. The phase and energy fractions (Fig. 4.4j,k) also show this behaviour, with the kinetic energy specifically showing a rapid decay akin to that observed in the studies of Seifried *et al.* (2018). *S1* overshoots *SN1* in the kinetic energy after ~ 300 kyrs, maximum density after ~ 1 Myr, and cold mass fraction after ~ 2 Myr. The sustained compression and acceleration of material in the *S1* scenario subsequently results in the steady increase of these properties, with the final maximum density growing to values of $\sim 10^4\,\mathrm{cm}^{-3}$, 2 orders of magnitude higher than *SN1*. At $n = 10^4\,\mathrm{cm}^{-3}$, gravity is dominating, and since 70 per cent of the *S1* material is in the cold regime (Fig. 4.4j), the probability of star formation is high. Indeed our results in Chapter 3 showed evidence of local gravitational collapse. At a maximum $n = 100\,\mathrm{cm}^{-3}$ however and with less than 5 per cent of material in the cold regime, clearly in *SN1* the conditions for self-gravity to dominate and cause local gravitational collapse are not created. We note however that the cold mass fraction does appear to increase in Fig. 4.4(j) (although the maximum density decreases) suggesting that the structure is not in the final stage of formation.

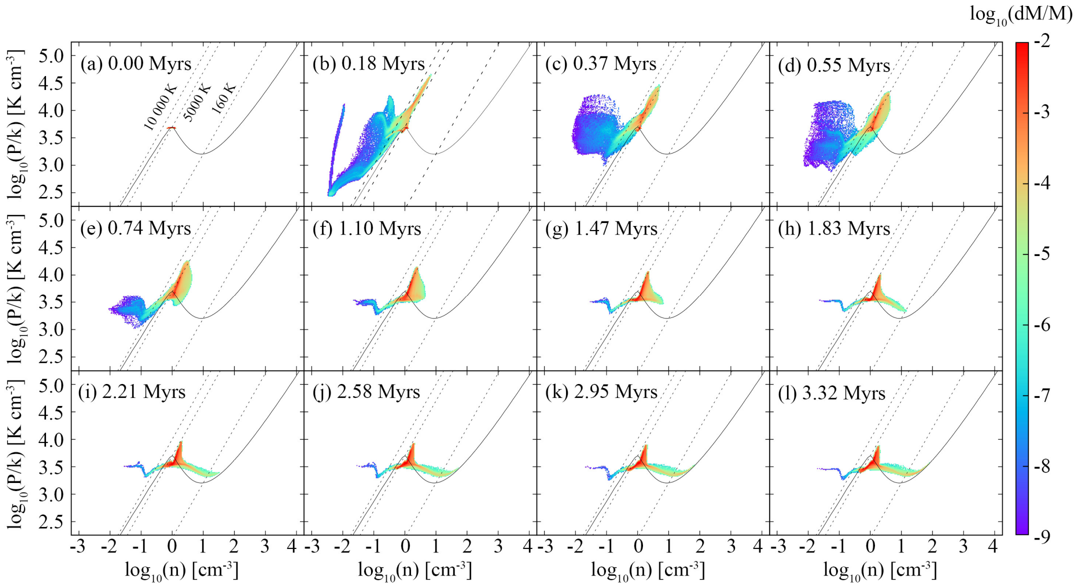

Figure 4.5: Panels (a – l) show the mass distribution of cloud material represented in pressure-density space for the *SN1* scenario. Isotherms differentiating the hot ($T > 10\,000$ K), warm ($10\,000 > T > 5000$ K), unstable ($5000 > T > 160$ K) and cold ($T < 160$ K) thermal regimes are shown on each panel. Presented is a period of 2.95 Myrs from $t_{\mathrm{inj}} = 11.78$ Myrs, after which material settles into a relatively steady state where the cold material evolves primarily due to gravity, and the warm envelope expands into the surroundings.

4.3.1.3 Formation of cold material

Figure 4.5 shows the mass distribution of cloud material in pressure-density space, along with the equilibrium curve and isotherms for the hot ($T > 10\,000$ K), warm ($10\,000 > T > 5000$ K), unstable ($5000 > T > 160$ K) and cold ($T < 160$ K) thermal regimes. Note that the data shown is only for material where the advected scalar $\alpha > 0.9$, i.e. cloud material.

Panel (a) shows the moment before any impact. Note that the remapped material exists where $\alpha < 0.9$, and as such it is not seen in the panel. Panel (b) clearly shows the compression of cloud gas due to the transmitted shock, and the heating of unstable material to the warm regime. The low-pressure, low-density gas that results from the reflection of the primary shock has now mixed with the cloud and is traced by the scalar α, and thus can be seen to exist in the hot regime. In panel (c), a clear rise in pressure and density can be seen with this material, which is an effect that can be credited to the impact of the secondary shock. In the warm regime, a drop in density and a broader pressure distribution can also be seen as material begins to cool towards thermal equilibrium, a pattern that continues in panels (d) and (e).

What is most striking is the behaviour of the gas over the next 1.5 Myr. In the *S1* scenario, post-shock gas is seen to cool from the warm regime directly to the cold phase, completely passing the unstable phase. Here we instead see material cool from the warm regime back to the unstable phase, and then migrate towards the cold phase from the unstable phase - in a fashion that resembles action of the thermal instability. This is exactly what was seen in the *NoShock* scenario presented in Chapter 3 (in particular fig 3.3(a – e)). In *NoShock*, the thermal instability formed cold and dense clumps embedded in warm intercloud gas. We would therefore expect to see such structures form here, which indeed appears to be the case. What looks like a filament in the density slices shown in figure 4.4(c – h) is in fact a cross-section through a broader cap-like structure, with what looks like clumps embedded in a diffuse warm envelope, features better seen in projection.

In Fig. 4.6 we show column density projections at $t = 5.16$ Myr. Two lines-of-sight (LOS) are considered, with the image in panel (a) being a projection perpendicular to the $z = 0$ plane (LOS shown in panel b), and (b) being along the axis of symmetry as determined by the blast (LOS shown in panel a). Here, the length of the lines represent the projection depth, such that only material within the volume as defined by the depth is projected. The axes of the resultant projections are subsequently shown in the centre of mass frame of the cold

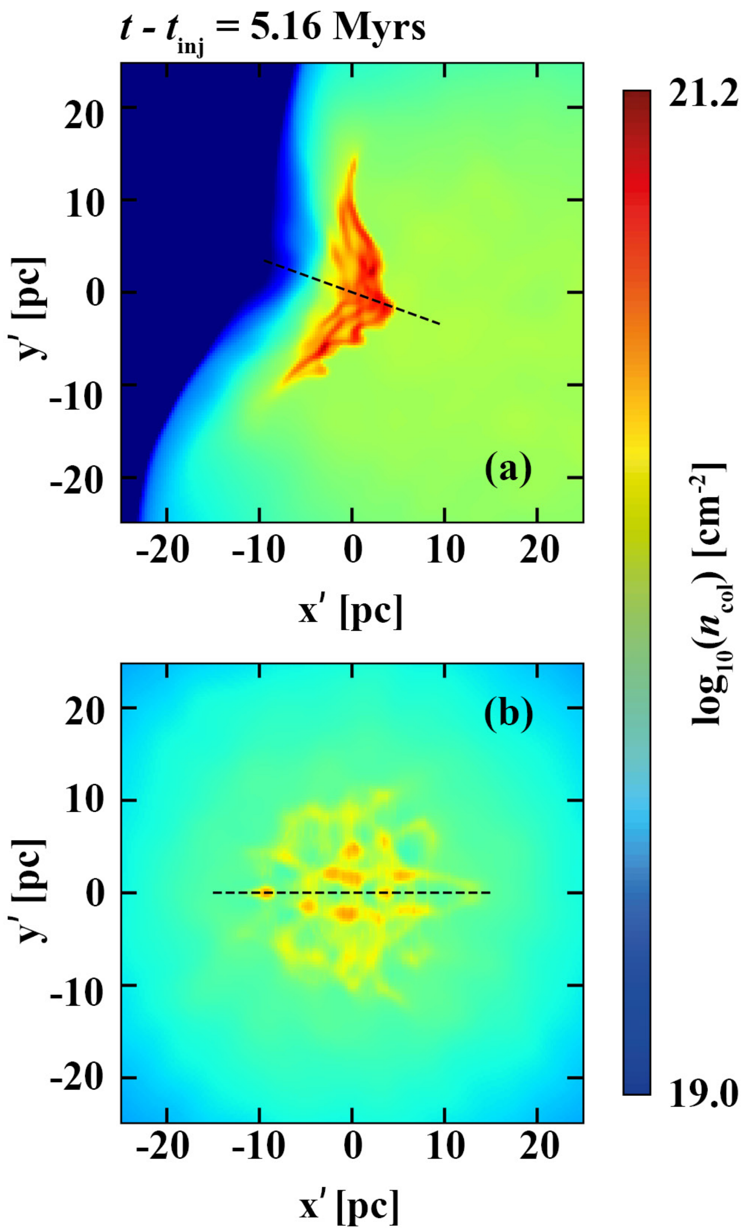

Figure 4.6: Shown are logarithm plots of column density projections along two lines of sight for the *SN1* scenario. The dashed line in panel (a) corresponds to the line of sight for panel (b), and vice versa in panel (b). The length of each line corresponds to the projection depth. Note that the axes in the image do not correspond to the original axes of the simulation, and instead form the axes of the projected image centered on the centre of mass of the cold structure ($T < 160\,\text{K}$).

material.

In a projection perpendicular to the $x-y$ plane (Fig. 4.6a) the singular filamentary-like identity seen in Fig. 4.4 is mostly lost, and the projection reflects a morphology consistent with a conic, cap-like structure that has been shaped by the convergent flow. In the projection shown in Fig. 4.6(b) we see that the filamentary identity is completely lost and within the surface there appears to be a small complex of clumps separated by distances typical of structures created by the thermal instability ($\sim 3-5\,\mathrm{pc}$, see WPFVL16 and Chapter 3). The clumps themselves have average densities $n \approx 80\,\mathrm{cm}^{-3}$, temperatures $T \approx 30-50\,\mathrm{K}$ and sizes $r \approx 1-2\,\mathrm{pc}$. We thus see that the supernova shock has triggered accelerated thermal evolution in the localised area of the 'front' of the cloud, closest to the supernova, and on realistic timescales formed the TI-driven structure expected from such a phase transition (e.g. see Falle *et al.*, 2020). As mentioned, the cold mass fraction is gradually increasing, suggesting that these clumps are not in their final stages of formation, however no star formation is observed. We note that the fragmentation of such post-shock layers has been documented in the literature (e.g. Whitworth *et al.*, 1994; **?**; **?**; Dinnbier *et al.*, 2017), providing more detailed discussions on the potential origins of clumps similar to those seen here.

4.3.2 Interaction with molecular cloud - SN2

Just like *SN1*, we present the *SN2* scenario by focussing first on the dynamics outside the cloud and secondly on the dynamics inside the cloud. Throughout our discussion we compare and contrast this behaviour to the idealised planar shock scenario *S2*, the un-shocked scenario *NoShock*, and the previously presented scenario *SN1*.

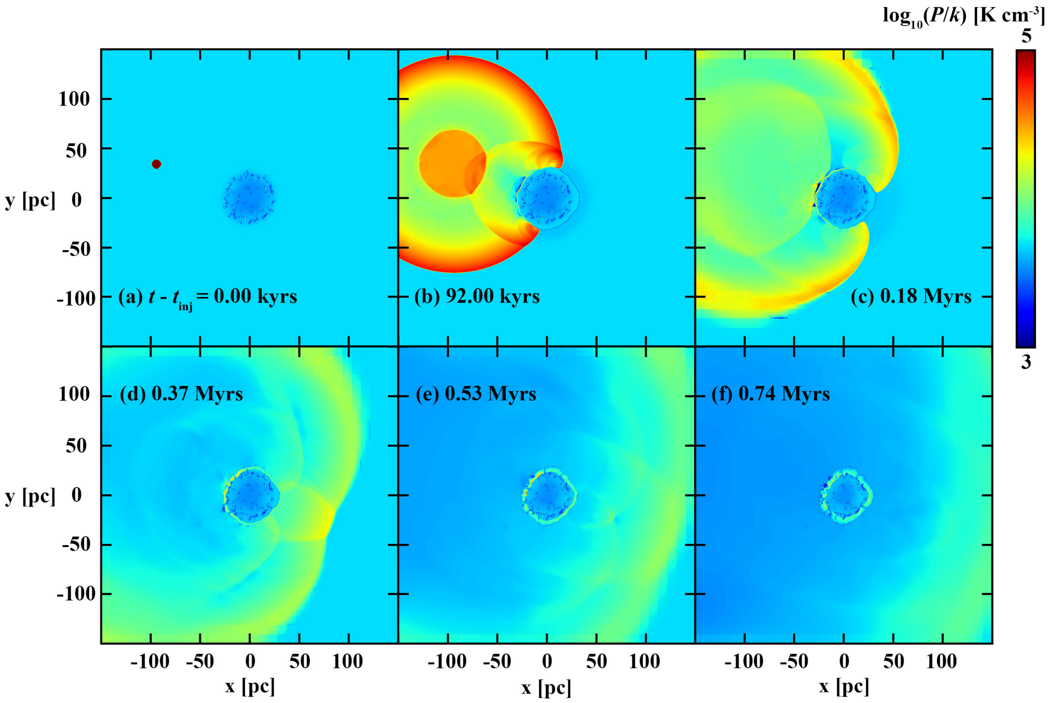

Figure 4.7: Shown are pressure logarithm plots in the $z=0$ plane of the *SN2* scenario. The time in each panel corresponds to the time since supernova injection t-$t_{\rm inj}$, with $t_{\rm inj}=26.5\,$Myr. Just like the *SN1* scenario, the final snapshot shows the moment immediately prior to the primary shock moving off the grid and the development of the upstream flow.

4.3.2.1 Dynamics outside the cloud

We illustrate the external behaviour by again showing snapshots of the pressure logarithm in the $z=0$ plane (figure 4.7) and a snapshot at 5.16 Myrs showing pressure and velocity profiles in the same plane for both *SN2* and *S2* (figure 4.8). The full evolution is presented on the same timescale of 5.16 Myrs which just like for *S1* is the timescale of the first snapshot in *S2* that showed evidence of local gravitational collapse.

Fig. 4.7(a) shows the moment once all of the 10 $M_\odot$ and 10^{51} erg are injected into the domain. A supernova explosion follows, and the remnant propagates out into the surroundings sweeping up mass and thermalising material as it does so. Just like in *SN1*, a Sedov-Taylor-like profile develops with a forward shock, reverse shock, and a contact discontinuity separating the two. The reverse shock then reflects at the blast epicentre, sending a secondary shock propagating back towards the cloud.

The subsequent evolution is very similar to *SN1*, however subtle differences are worth pointing out. Firstly, the cloud no longer has a smooth edge, resulting in multiple wave reflections that distort both the primary and secondary shocks. As the primary shock sweeps over the cloud and interacts with the inhomogeneities, sets of oblique shocks form which distort the profile further. These are seen to persist for up to 180 kyrs (Fig. 4.7c), and are destroyed after the passage of the secondary shock. Secondly, the cloud is smaller than in *SN1*, resulting in shorter timescales for the passage of the shocks. As can be seen in Fig. 4.7(d) - the primary shock has converged, and the panel captures the moment prior to secondary shock convergence. Contrasting this to *SN1* (Fig. 4.2d), the primary shock has yet to converge at this time. In spite of these differences, in the next ~ 4 Myrs the ambient medium behaves almost identically to the *SN1* scenario: a low velocity, laminar upstream flow develops that converges at the front of the cloud, and the thermal pressure drops globally.

The final state of this behaviour is seen in figure 4.8, showing the same order of magnitude differences between the velocity and thermal pressures, giving a thermal pressure difference of a factor ~ 2.5 lower in *SN2* than *S2*, and ram pressure difference a factor ~ 100 lower (on the cloud edge). The most surprising behaviour in this scenario is the state of the *SN2* cloud itself, showing that although the cloud becomes immersed in under-pressured surroundings just like

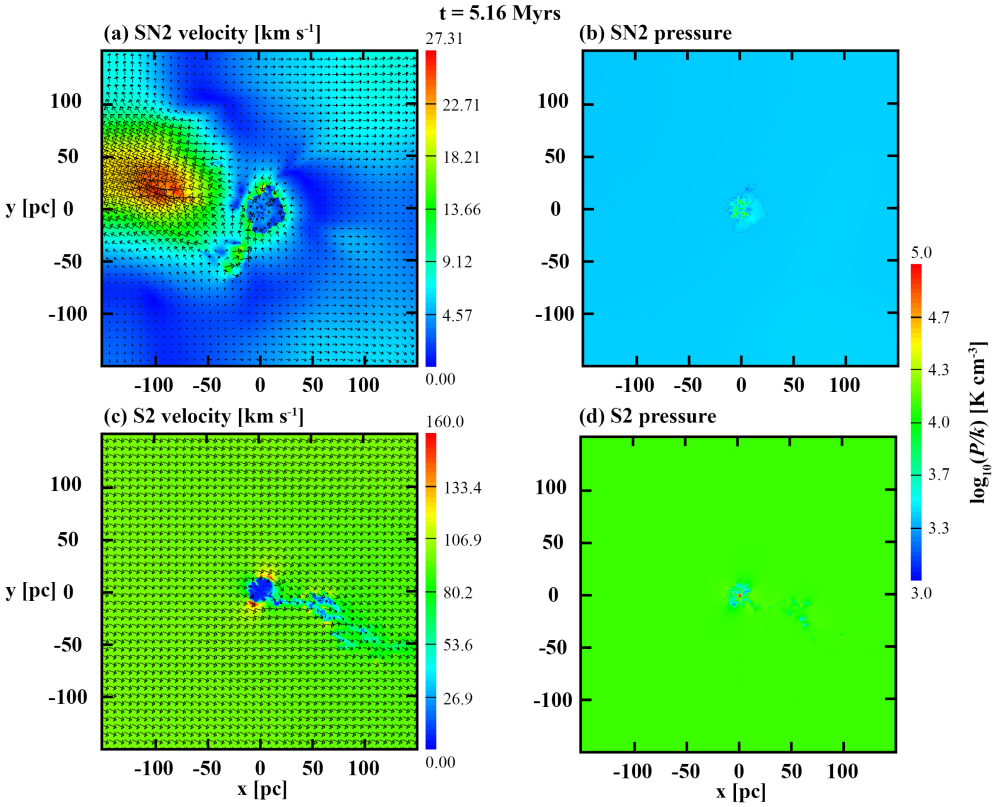

Figure 4.8: Shown are plots in the $z = 0$ plane showing the velocity (panels a and c) and pressure (panels b and d) of *SN2* (panels a and b) and *S2* (panels c and d) at t - $t_{\rm inj} = 5.16$ Myrs - the final snapshot presented in this chapter and the timescale at which the *S2* scenario witnessed local gravitational collapse.

in *SN1*, the cloud has not expanded. The cloud in fact continues to contract (albeit not as fast as *S2*), which is clearly a gravitational effect. In this scenario therefore, the ambient behaviour is only weakly coupled to the cloud.

4.3.2.2 Dynamics inside the cloud

We now discuss the dynamics inside the cloud and refer to the density logarithm snapshots and statistics in figure 4.9. Again we show the maximum density (i), mass fractions in the cold, unstable and warm thermal regimes (j), and the fractions of thermal and kinetic energies (k).

This scenario begins at 26.5 Myr. The evolution of the material inside the cloud has so far been dominated by the effects of the thermal instability which has generated a complex of cold and dense clumps embedded in a warm diffuse gas. The evolution of the thermal instability in the *NoShock* case was covered in section 3.3.1 of Chapter 3. To summarise, the initial grid-scale inhomogeneities initialised around the thermally unstable equilibrium smooth out and seed the instability within the first few thousand years of evolution. The cloud remains quiescent for $\sim 15\,\mathrm{Myr}$, corresponding to a period that sees a growth of the inhomogeneities, enhancing the pressure and density differences within the cloud. A critical point is reached within the next $\sim 5\,\mathrm{Myrs}$ where the cooling rates increase such that cold material cools further, causing it to be further compressed by the over-pressured surroundings. This continues to cool until temperatures reach a stable cold equilibrium, resulting in densities increasing from $n \sim 1\,\mathrm{cm}^{-3}$ to $n > 100\,\mathrm{cm}^{-3}$ in a period of $\sim 3\,\mathrm{Myr}$. Gravity subsequently increases these densities to $\sim 1000\,\mathrm{cm}^{-3}$ prior to the global collapse of the cloud at $\sim 35\,\mathrm{Myr}$.

Following phase transition and prior to the global collapse, the state of the cloud is a complex of cold and dense ($T \sim 50-160\,\mathrm{K}$, $n \sim 100-1000\,\mathrm{cm}^{-3}$) clumps embedded in a warm and diffuse ($T \approx 5000\,\mathrm{K}$, $n \approx 0.8\,\mathrm{cm}^{-3}$) gas. Low-density,

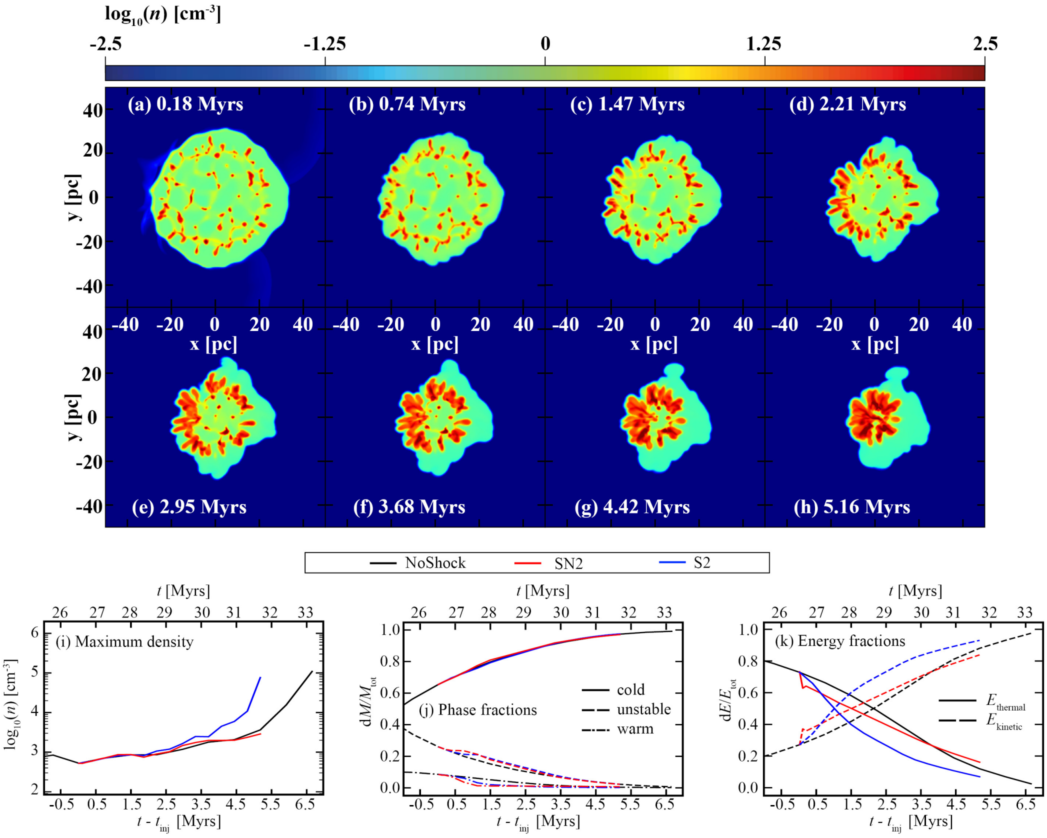

Figure 4.9: Panels (a – h) show density slices in the $z = 0$ plane for the *SN2* scenario. The logarithm of the number density is shown, and the time on each panel corresponds to the time elapsed since supernova injection t - t_{inj}, where $t_{\mathrm{inj}} = 26.5\,\mathrm{Myr}$. Panels (i), (j) and (k) respectively show the maximum density, phase fractions and energy fractions in the cloud, showing data for *SN2* (red lines), *S2* (blue lines) and *NoShock* (black lines) for direct comparison at equivalent times. Panel (j) shows mass fractions in cold ($T < 160\,\mathrm{K}$, solid line), unstable ($160 < T < 5000\,\mathrm{K}$, dashed line) and warm ($5000 < T < 10\,000\,\mathrm{K}$, dot-dashed line) regimes. Panel (k) shows the fractions of the thermal energy E_{thermal} (solid line) and kinetic energy E_{kinetic} (dashed line) out of $E_{\mathrm{tot}} = E_{\mathrm{thermal}} + E_{\mathrm{kinetic}}$ in the cloud. Gravitational energy is ignored.

diffuse ($T \approx 700\,\mathrm{K}$, $n \approx 5\,\mathrm{cm}^{-3}$) structures resulting from thermal flows connect the clumps, and the clumps appear somewhat elongated towards one another, serving as evidence that these clump-connecting structures are possible regions of filament formation (e.g. seen in the high resolution hydrodynamical simulations of Wareing *et al.* (2019)). As mentioned, the first detailed study of this behaviour was conducted by WPFVL16 and for extra details and comparisons between non-gravitational simulations and ones including magnetic fields - we refer the reader there. We now describe the impact of the supernova on material inside the cloud.

Upon impact, the primary shock has an equivalent strength to that in *SN1* with an approach velocity of $\sim 1000\,\mathrm{km\,s^{-1}}$. The interclump material is impacted first and accelerated towards the cloud interior. By Fig. 4.9(b) the shock has interacted with the clumps, and many individual shock-clump interactions ensue. The clumps are accelerated less than their surroundings, thus interclump material is seen to be pushed inwards between the clumps - most apparent in panels (c – d). Note that by panel (d), the upstream flow around the cloud contributes to this effect.

As the shock interacts with individual clumps, they appear to elongate slightly towards the cloud centre and develop tail-like morphologies, an effect due to their outer envelopes being stripped in the direction of the post-shock flow and potentially due to impact with the material swept up by the shock itself (Pittard, 2011). The material connecting the clumps is disturbed also and contributes to this tail-like appearance, again orienting radially towards the centre. Note that the irregular interface and presence of clumps distorts the shock front, and as such its position is not obvious in the panels. However, by panel (d) it is evident that the shock has interacted with outer clumps around all of the cloud's edge, as they all appear to have these elongated morphologies from their stripped envelopes.

Tail-like features were seen both in *NoShock* and *S2*, but to very different extents. In the *NoShock* scenario, material was accelerated radially inwards by gravity only, with clumps accelerated slower than the interclump material. The resulting velocity gradients were quite weak, although large enough to slightly ablate the clump envelopes, resulting in similar, albeit much less pronounced tail-like morphologies compared to *S2/SN2*. This is seen in both Chapter 3 and WPFVL16 (who also observe that equivalent models in 2D exaggerate this effect due to motion being restricted to a plane). In the *S2* scenario, this effect is much more pronounced, as after shock passage the clumps become entrained in a continuous flow. Although the initial impact is weaker than in *SN2*, the post-shock flow is in total much more disruptive, with clump material being continuously ablated. The constant flow results in continuous acceleration of the interclump material, resulting in some clumps breaking away from the cloud. These clumps become fully entrained in the external flow, which further exaggerates the formation of elongated tails, and destroys some clumps completely. In contrast, no clumps are seen to break away from the cloud in the *SN2* scenario.

In addition to seeing clumps elongate, they also appear to increase in size and coalesce into larger cold regions. This appears to be due to their outer envelopes expanding. As the shock enters the cloud, its post shock pressure drops due to the combination of increased cooling in the cloud, gas attempting to match the decreasing external pressure, and gas expansion effects characteristic of Sedov-Taylor-like evolution. Due to these effects, the clumps become embedded in material with lower pressure than the initial interclump material, and their outer envelopes expand, with the remainder of the material bound together by gravity. This pressure profile is illustrated in Fig. 4.10 showing the cloud at 2.21 Myrs. The high pressure discontinuities near the cloud center mark the position of the transmitted shock which can be seen to surround a central region of the cloud not yet disturbed by the shock. The pressure in this region is equivalent to the inter-

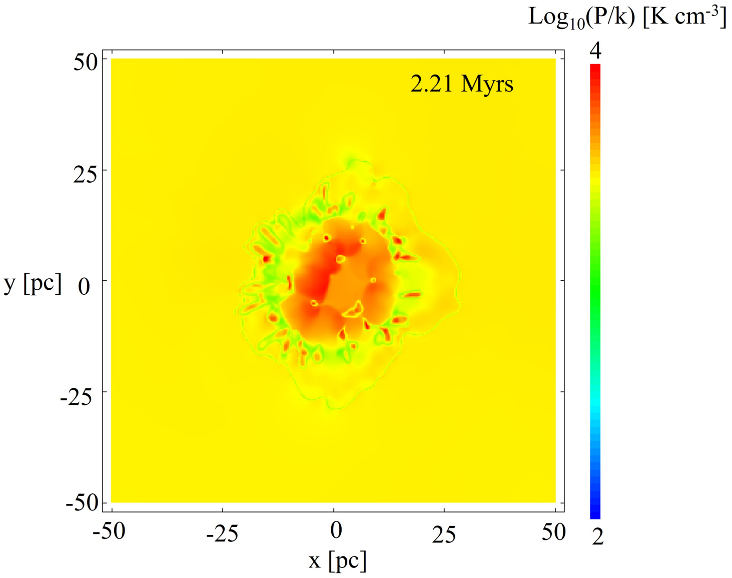

Figure 4.10: Pressure profile in the z = 0 plane for the *SN2* scenario at $t = 2.21$ Myrs. The logarithm of the pressure is shown, and the time of the panel corresponds to the time elapsed since supernova injection $t - t_{\mathrm{inj}}$, where $t_{\mathrm{inj}} = 26.5$ Myr. The equivalent density slice is shown in Fig. 4.9(d)

clump pressure pre-shock passage, which is much higher than the pressures of the gas that the clumps are embedded in (visible in the dark-green pseudo-colour region). The cooling is strongest at the front, and as such we see the majority of clump expansions occur there (see Fig. 4.9d – f). Thus this increase in size is not to be mistaken by a gain in clump mass - also apparent by the lack of deviation from the cold mass fraction *NoShock* (Fig. 4.9j).

Note that what we could also be seeing is thermal-instability induced material forming at the front in a manner similar to *SN1*. However, it is difficult to find explicit evidence that would differentiate this from the individual clump expansion, as the effects of the thermal instability would be seen at the front (similar to *SN1*), which is where the clumps expand the most. In addition, any migration across the phase diagram akin to figure 4.5 is obscured as the existence of the two-phase medium occupies exactly that portion of the diagram. The only possible evidence is a short-lived increase of cold material seen in Fig. 4.9(j) which occurs on the order of the cooling timescale of the post-shock gas. However this is negligible ($\lesssim 1\%$ increase, $\sim 100\,\mathrm{M}_{\odot}$), and returns almost immediately to the *NoShock* fraction. Thus in this scenario we conclude that once the clumps have formed, the supernova impact does not trigger any further thermal instability.

At later stages of evolution, many of the clumps appear to collide and merge. This is interesting, as we would expect this effect to raise the maximum density in the cloud. Inspecting individual clumps shows that densities do increase in merging regions, however these are small and do not exceed the maximum. There does appear to be a slight increase in the maximum density for a brief period (see Fig. 4.9i) however again this returns to *NoShock* values, and eventually decreases further. In *S2*, we can see that at 5.16 Myrs densities are attained that are two orders of magnitude larger ($\sim 10^5\,\mathrm{cm}^{-3}$) than in *SN2* ($\sim 10^3\,\mathrm{cm}^{-3}$). Once again, this can be attributed to the fact that the *S2* cloud was continuously compressed, resulting in local gravitational collapse, and an acceleration of the global collapse of the cloud.

It is interesting therefore to observe that a supernova blast is unable to create such conditions. In fact, looking at the density snapshots, and examining the extracted data from the model - after the first 3.5 Myrs the cloud is almost indistinguishable from the *NoShock* scenario. Once the initial impact of the supernova is seen, the cloud settles into a steadily, globally collapsing state with gravity dominating the evolution. Nevertheless, even with more than 50 per cent of the cloud material being cold and dense (increasing up to ~ 90 per cent), a single supernova event is unable to aid gravity in collapsing individual structures prior to the global collapse of the cloud. Thus we conclude that no extra star formation is to be expected from this interaction. Further work is warranted to see if such behaviour is seen when a supernova interacts with TI formed clouds with different masses, and ones simulated at higher resolution that results in the hydrodynamic formation of filaments (as seen in Wareing *et al.* (2019)).

4.4 Discussion and Conclusion

In this chapter, we study the interaction of a supernova remnant with a cloud that is evolving due to the thermal instability (TI) and gravity, and draw comparisons to idealised shock-cloud scenarios and a scenario without shocks. A total of five 3D hydrodynamical simulations were performed: an un-shocked scenario *NoShock*, two shock-cloud scenarios in the *small cloud regime*, *S1/S2*, respectively analogous to *12Shock/24Shock* in Chapter 3, and two supernova-cloud scenarios in the *large cloud regime*, *SN1/SN2*, looking at impacts at equivalent times to *S1/S2*. Just like Chapter 3, the disturbance is introduced at a "pre-TI" (*S1/SN1*) and "post-TI" (*S2/SN2*) stage, and the models are evolved for a timescale corresponding to the first snapshots when the shock-cloud scenarios *S1/S2* showed evidence of local gravitational collapse.

For our chosen parameters, the Mach number of the supernova shock is roughly a factor $\sim 4.5\times$ stronger at impact than that of the planar shock. However on aggregate the supernova is significantly less disruptive than the sustained impact from the idealised post-shock flow. In *S1/S2*, the post-shock flow is constantly replenished and approaches the cloud at $\sim 100\,\mathrm{km\,s^{-1}}$. This provides a ram pressure that consistently throughout the simulation is a factor $\sim 100\times$ larger than from the $\sim 10\,\mathrm{km\,s^{-1}}$ flows that develop around the cloud in the *SN1/SN2* scenarios. Additionally, the constantly replenished flow means that the ambient thermal pressure is maintained at higher values than those in the cloud, resulting in continuous compression throughout the entire simulation. In contrast, the profile within the remnant is Sedov-Taylor-like. As such the impact of the blast on the cloud decays rapidly, the cloud is not met with a continuous flow, and the ambient thermal pressure drops below that of the cloud in less than 1 Myr. These facts accounts for all of the differences seen between the supernova/shock models, and we observe the following particular outcomes:

1. *SN1/SN2*: The cloud is impacted by two shocks - a primary shock that is the forward shock from the initial blast, and a secondary shock resulting from the reverse shock that reflects at the blast epicentre and propagates back outwards and towards the cloud. The impact of the secondary shock on each cloud is weak, and its influence is mainly felt at the cloud − ambient interface.

2. *SN1/SN2*: The primary and secondary shocks sweep over the cloud and generate complex wave patterns that propagate both downstream and upstream. The upstream components generate a flow on the cloud interface that converges at the front.

3. *SN1/SN2*: The primary shock loses much of its strength as it sweeps over the cloud. When it converges at the rear of the cloud, the convergence has negligible effect in amplifying the impact. In fact, as the model evolves, the strongest ram pressures occur at the front of the cloud where the upstream interface flow converges. This is in stark contrast to *S1/S2*, where the strongest compression was at the rear.

4. *SN1*: The lower ambient pressure compared to that of the cloud (ram + thermal) results in a constant and gradual cloud expansion. Where the upstream flow converges, the expansion is prevented - giving the cloud a lobe-like morphology.

5. *SN1*: The lack of continuous flow means that the Rayleigh-Taylor, Vishniac and Kelvin-Helmholtz instabilities are not triggered.

6. *SN1*: The TI is triggered behind the primary shock. This forms a cap-like structure with clumps embedded inside with properties expected from such a phase transition. The maximum densities in these structures do not exceed $100\,\mathrm{cm}^{-3}$, however the cold mass fraction is increasing, suggesting the structure is not in its final stages of formation. Nevertheless, we do not expect star formation to occur on the same timescales as *S1*.

7. *SN2*: The passage of the shock through the interclump medium results in the formation of tail-like structures due to clump envelopes being ablated. This does not happen to the same extent as in *S2*, e.g. no clumps are seen to break away from the parent cloud and get entrenched in an external flow. This effect is however more pronounced than that due to flows resulting only from gravitational acceleration of material in the *NoShock* scenario.

8. *SN2*: After shock passage, the clumps appear to increase in size. This is not due to an increase in mass, and instead due to expansion. This happens because the inter-clump pressure drops below that of the clumps after shock passage.

9. *SN2*: Clumps are seen to coalesce and merge. This however does not increase the maximum density in the cloud or cause any local gravitational collapse.

10. *SN2*: Although the exterior pressure drops below that of the cloud within the first 1 Myr, the cloud does not expand as it is gravitationally dominated. After ~ 3.5 Myr, the cloud is almost indistinguishable from the *NoShock* scenario. Thus, apart from the trivial global collapse of the cloud, we do not expect to see any additional star formation.

Chapter 5

Turbulence analysis

The results for the *12Shock* and *24Shock* scenarios shown in this chapter are published in Kupilas *et al.* (2021).

5.1 Introduction

For molecular clouds dominated by H_2 gas, cold temperatures of $\mathrm{T} \sim 10\,\mathrm{K}$ imply sound speeds of $c_s \approx 0.2\,\mathrm{km\,s^{-1}}$. Internal velocity dispersions however, as measured by the linewidth, are calculated to be $\sigma \approx 0.5 - 10\,\mathrm{km\,s^{-1}}$ (see e.g. Larson, 1981; Solomon *et al.*, 1987). Thus the gas in molecular clouds is mostly highly supersonic, with Mach numbers $M = \sigma / c_s \gg 1$.

The empirical size-linewidth relation of Larson (1981), although often contested (see e.g. Ballesteros-Paredes *et al.*, 2019, and references therein), has for over 40 years implied that molecular clouds are supersonically turbulent. Indeed considering even simple physical arguments, this is almost certainly true. Formally, for a system with a characteristic size L, characteristic velocity V and kinematic viscosity ν, its flows are considered turbulent when the Reynolds number $\mathrm{Re} \gg 1$, where

$$\mathrm{Re} = \frac{LV}{\nu}. \tag{5.1}$$

The quantity $V/\nu = 1/l_{\mathrm{diss}}$, where l_{diss} is the dissipation length. Flows where $\mathrm{Re} < 1$ are laminar, and the transition to turbulence occurs at $\mathrm{Re} \gtrsim 1$. Note that the transition from laminar to turbulent flows is an unsolved problem in physics, as such these numbers only provide order of magnitude estimates. Following the argument presented in Krumholz (2014), for a non-magnetic, diffuse gas, the kinematic viscosity is $\nu = 2\overline{u}\lambda$, where $\overline{u}$ is the root mean square (RMS) particle speed, and $\lambda \sim 1/n\sigma$ is the particle mean free path. Here, n is the particle number density and σ is the cross section. For a neutral particle like H_2, $\sigma \sim 10^{-15}\,\mathrm{cm}^2$. Thus, typical densities in molecular clouds of $n \sim 100\,\mathrm{cm}^{-3}$ imply $\lambda \sim 10^{13}\,\mathrm{cm}$, and with the RMS particle speed being comparable to the sound speed, i.e. $\overline{u} \sim 0.2\,\mathrm{km\,s}^{-1}$, it means that $\nu \sim 10^{17}\,\mathrm{cm}^2\,\mathrm{s}^{-1}$. Combining this result with a characteristic length and velocity of $L = 10\,\mathrm{pc}$ and $V = 1\,\mathrm{km\,s}^{-1}$ respectively, we find that in molecular clouds $\mathrm{Re} \sim 10^9$. Thus the flows are invariably turbulent

The role of turbulence in molecular cloud dynamics is a strongly debated topic and its importance is emphasised by many authors (Mac Low & Klessen, 2004a; McKee & Ostriker, 2007; Hennebelle & Falgarone, 2012; Federrath, 2013a). Numerical simulations and analytical models with fine-tuned turbulence driving parameters are able to address fundamental problems associated with stellar clustering (e.g. Hopkins, 2012a, 2013b), the star formation rate (e.g. Kravtsov, 2003; Wada & Norman, 2007), the filamentary nature of molecular clouds (e.g. Federrath, 2016), and the slope and peak of the IMF (e.g. Padoan & Nordlund, 2002; Hennebelle & Chabrier, 2008, 2009; Clark *et al.*, 2011; Hennebelle & Chabrier, 2013; Hopkins, 2012b, 2013a). It is not fully understood however what these driving parameters represent, and more broadly what the dominant physical processes governing the flows are.

In molecular clouds, the fluid viscosity is one of many interacting dissipative mechanisms, with the action of ambipolar diffusion (e.g. Li *et al.*, 2012) and thermal phase transitions (e.g. Wareing *et al.*, 2019, 2021, hereafter WPF19, WPF21) possibly setting the dissipative limit prior to the action of fluid viscosity, acting to lower the Reynolds numbers. The dominant driving mechanisms are unclear also: spiral-arm compression (e.g. Dobbs *et al.*, 2008; Dobbs & Bonnell, 2008) magnetorotational instability (e.g. Balbus & Hawley, 1991; Tamburro *et al.*, 2009), gravitationally driven flows and fragmentation (e.g. Field *et al.*, 2008; Van Loo *et al.*, 2014; Vázquez-Semadeni *et al.*, 2019), cloud-cloud collisions (e.g. Wu *et al.*, 2018), supernova explosions (e.g. Padoan *et al.*, 2016), thermal instability alone (WFP19), or with combinations of other processes (e.g. Saury *et al.*, 2014; Kim *et al.*, 2008; Yang & Krumholz, 2012), all contribute on different time and length scales.

To address this problem, turbulent flows are often described in terms of statistics of density and velocity (and magnetic field for MHD turbulence). A common statistic is the power spectrum, which characterises how rapidly the quantity under analysis changes as one moves between two points in a turbulent flow (see e.g. Elmegreen & Scalo, 2004). Theoretically, between a driving scale and a dissipation scale, a turbulence power spectrum should display an inertial range over many decades of wave number that scales as $E(k) \propto k^{\alpha}$ with a constant value of α, where $E(k)$ corresponds to power contained in wave number modes in the interval between k and $k + \mathrm{d}k$. The Kolmogorov (1941, hereafter K41), incompressible, hydrodynamical turbulence power spectrum scaling follows an $E(k) \propto k^{-5/3}$ slope, while the supersonic, compressible power spectrum scales as $E(k) \propto k^{-2}$ (Burgers, 1948, hereafter B48).

There are challenges with using the power spectrum as a tool to study molecular cloud turbulence. Due to the computational demands associated with resolving spatial scales of many orders of magnitude, numerical simulations are unable to resolve a full inertial range. The highest resolution turbulence simulations to date (4096^3 for hydrodynamic turbulence (Federrath, 2013b)) can capture a maximum of 3 decades. Additionally, comparisons of simulations should ultimately be made with observational results, which comes with its own set of challenges when using the power spectrum as a diagnostic tool (e.g. Lazarian, 2009). Finally, due to the statistical nature of a 1D spectrum, dynamical details can be lost when applying it to the study of molecular clouds, with very different fluid behaviour showing similar spectral behaviour (Kupilas *et al.*, 2021, hereafter KWPF21).

In this chapter, we take advantage of the fact that we have analysed models where the physical prescription is relatively simple, the dominant physics at different stages reasonably well understood, and derive the power spectra for the velocity, density and density logarithm. We attempt to connect their behaviour to the dynamics seen in the models, and explore whether any of it registers as spectra with constant slope, thus possibly capturing any turbulent behaviour. We present an overview of the methods in Section 5.2, in Section 5.3 we present the results, and in Section 5.4 we conclude this Chapter.

5.2 Methods

Power spectra are calculated using the same IDL script that was used in WFP19, WPF21 and KWPF21.

A power spectrum $E(\mathbf{k})$ of quantity $\mathbf{q(x)}$ can be defined in terms of the square of the Fourier coefficients,

$$E(\mathbf{k}) \equiv \frac{1}{2}|\tilde{\mathbf{q}}(\mathbf{k})|^2, \tag{5.2}$$

obtained from the 3D Fourier transform as

$$\tilde{\mathbf{q}}(\mathbf{k}) = \frac{1}{(2\pi)^3}\int_V \mathbf{q}(\mathbf{x})e^{-2\pi i\mathbf{k}\cdot\mathbf{x}}\mathrm{d}^3x \tag{5.3}$$

Here, $\mathbf{k} = k_x\hat{\imath} + k_y\hat{\jmath} + k_z\hat{k} = \frac{2\pi}{l_x}\hat{\imath} + \frac{2\pi}{l_y}\hat{\jmath} + \frac{2\pi}{l_z}\hat{k}$ is the 3D wave vector, and the integral is over the 3D physical volume V. Note that $E(\mathbf{k})$ is an expression for the power per unit volume in 3D k-space, and to derive the 1D spectrum, this is binned into wave numbers as

$$E(k) \equiv \int_{V_\mathrm{k}} E(\mathbf{k})\delta(|\mathbf{k}| - k)\mathrm{d}^3k \tag{5.4}$$

where $\delta(k)$ is the Dirac delta function, and the integral is performed over the 3D wave number volume V_k. $E(k)$ is then the total power contained in modes with wave numbers in the interval between k and $k + dk$. Note that both $E(\mathbf{k})$ and $E(k)$ are often referred to as power spectra in the literature. We explicitly refer to the latter expression of $E(k)$ as the power spectrum (sometimes quoted as $P(k)$ in the literature).

We derive power spectra for the *12Shock* and *24Shock* scenarios from Chapter 3, and *SN1* and *SN2* scenarios from Chapter 4. We then follow the evolution of the spectra over the initial 5.16 Myr timescale considered in these models, i.e. until the first evidence of gravitationally collapsing sub-structures were seen in the *12Shock* and *24Shock* scenarios. We take power spectra of the magnitude of the velocity vector $|\mathbf{v}| = \sqrt{v_x^2 + v_y^2 + v_z^2}$, the mass density ρ, and its logarithm $log(\rho)$. The raw data for the spectra is exported from a subsection of the domain in the region corresponding to -1.5 < xyz < 1.5, i.e a $150^3\,\mathrm{pc}^3$ box centered on the origin. We export the finest grid, and in regions where the grid is not fully refined, the values in the cells are interpolated to the finest grid. Our resolution means that the box under consideration has 512^3 cells. The box contains all of the cloud material, and a subsection of the remainder of the ambient gas (recall that the full computational domain is a $300^3\,\mathrm{pc}^3$ box). This choice of box size means that we can investigate the behaviour of the power spectrum across all of the thermodynamic phases in the model, consisting of hot ($\mathrm{T} > 10^4\,\mathrm{K}$) material in the ambient medium, and warm ($5000 < \mathrm{T} < 10^4$ K), unstable ($160 < \mathrm{T} < 5000$ K) and cold ($\mathrm{T} < 160$ K) material in the cloud, as defined by the cooling curve used (see Chapter 2 for details).

The primary focus is to identify if any insight into the dynamics can be gained from the power spectra, and in particular if the spectra contain an inertial range with self-similar scaling where $E(k) \sim k^{\alpha}$ scales with a constant value of α across a range of wave numbers. We are specifically looking out for two values of α. Subsonic and incompressible turbulence approaches the K41 index of $\alpha =$ -5/3. In this limit, both the density and velocity spectra are expected to behave in a similar fashion as the density field is not affected by fluctuations that are characteristic of compressible flows. Supersonic and compressible turbulence approaches the B48 index of $\alpha =$ -2. This slope is expected to emerge only in the velocity spectrum as compressibility can significantly affect the density structures due to the presence of shocks. This can in turn flatten the slope of the density spectrum, as more power is induced on the small scales (e.g. Kritsuk *et al.*, 2007). Flattening of the slope in the density spectrum is also expected when self-gravity becomes important (e.g. Federrath & Klessen, 2013). The density logarithm spectrum however are expected to display more stable and turbulent-like behaviour due to the logarithm operation filtering out extreme density contrasts (Kowal *et al.*, 2007).

5.3 Results

In this section we present the 1D power spectra of velocity, density and logarithmic density for the simulations presented in Chapters 3 and 4. We first present the power spectra for the shock-cloud *12Shock* and *24Shock* scenarios, followed by the spectra for the supernova-cloud *SN1* and *SN2* scenarios.

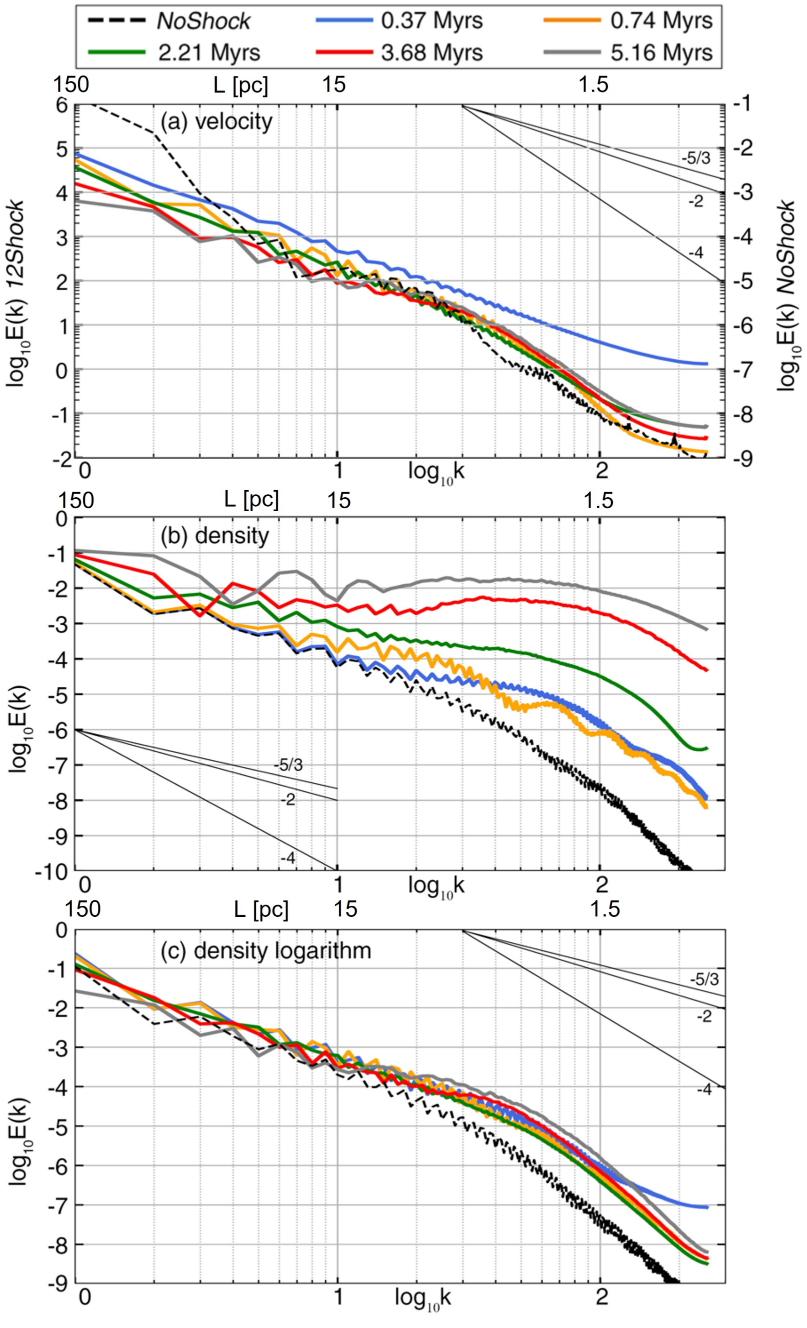

Figure 5.1: Shown are power spectra of velocity (panel a), density (panel b) and the density logarithm (panel c) for the *12Shock* scenario. The colours correspond to snapshots at times since shock introduction $t_{\rm shock} = 11.78\,$Myrs, and the black dashed line corresponds to the *NoShock* spectrum at $t_{\rm shock}$. In panel (a) the *NoShock* spectrum scale is shown on the right y-axis, whilst the *SN2* spectra correspond to the left y-axis. Note that the *NoShock* scenario considered in these panels is that from Chapter 3. The K41 -5/3, B48 -2 and a -4 slope are shown for comparison.

5.3.1 Shock-cloud scenarios

We illustrate the power spectra of the shock-cloud scenario *12Shock* in Fig. 5.1 and *24Shock* in Fig. 5.2. In both figures, spectra are shown for the velocity amplitudes in panel (a), density in panel (b) and density logarithm in panel (c). The *NoShock* spectrum is shown at the time of injection in all panels, and then 5 subsequent snapshots of the shock-cloud interaction spectra are shown. In the velocity spectra, the shock can be seen to have injected a large amount of energy on all scales, and as such the right y-axis scale corresponds to the *NoShock* spectrum, and the left y-axis to the shock-cloud spectrum. Note that this is only the case for the velocity spectra, and the scale on all other panels is the same for both the *NoShock* and shock-cloud scenarios. Lines with slopes α = -5/3 (K41), -2 (B48), and -4 are also shown on the figures.

5.3.1.1 ***12Shock* interaction**

Turning first to Fig. 5.1(a), we see that the shock injects a substantial amount of power on all scales. It is striking that at the initial stages of the interaction the spectrum appears to display a large inertial range spanning all scales of the computational domain, and the slope follows a power law somewhat close to the B48 α = -2. This is peculiar, as it is indicative of supersonic, compressible turbulence, which is unlikely to have had a chance to develop on these timescales, especially since the initial shock is weak and the post-shock flow is subsonic. One explanation for this slope could simply be due to the presence of a shock, regardless of how it interacts. Mac Low & Klessen (2004b) and Krumholz (2014) comment on the fact that a Fourier transform of a step function representative of a perfect shock results in an $\alpha = $-2 slope. We tested this by deriving a velocity power spectrum for a shock with physical properties identical to *12Shock* and *24Shock*, but without the cloud being present. The power spectrum was derived as soon as the shock was imposed, at a few subsequent time-step intervals, and at 60 kyrs. At all times a perfect $\alpha = $-2 slope was recovered with the spectra appearing the same as that seen at 0.37 Myrs in Fig. 5.1(a). The same timescales were then considered for tests with the cloud present, with almost identical spectra derived. It is not surprising therefore that we see such spectra here, although it is interesting to observe that the full slope persists for 0.37 Myrs, post impact with the cloud. Note that the shock is still on the grid however and has swept only over half of the cloud's edge, as such the spectra could simply be reflecting the energy contained in this shock.

Investigating the spectral behaviour at 0.74 Myrs, we see that this changes and the velocity spectra lose power on all scales, with most significant losses occurring after $k \gtrsim 30$ ($l \lesssim 5\,\mathrm{pc}$) where the spectra appear to have $\alpha \approx$ -4. This behaviour implies that the onset of the dynamical Kelvin-Helmholtz, Rayleigh-Taylor and Vishniac instabilities, as well as radiative cooling, are possibly enough to obstruct energy transfer to scales smaller than 5 pc, and the break could be an indicator of the length-scale of the instabilities. It is difficult to find explicit evidence to help determine which of these processes dominate, as the instabilities act in interdependence with each other and with radiative cooling. As has been demonstrated by WFP19, a break on these scales can also be indicative of flows decelerating across the warm – cold boundary between the clump and the interclump medium. Note that on scales larger than this, the slope is shallower, and appears to be somewhere between the K41 $\alpha = $-5/3 and B48 $\alpha = $-2 index. Indeed, inspecting the velocity field within and around the cloud shows a mixture of laminar-like and turbulent-like flows, especially around regions where the dynamical instabilities have been triggered.

Turning to Fig. 5.1(b), the density spectra show drastic differences when compared to the velocity spectra. With increasing time, they show significant flattening and a gain in power across all length scales. It is clear that the spectrum captures a power increase on the smallest scales first, likely due to the compression of radiatively cooled regions that subsequently become clumps. As the model evolves, these scales then show the strongest increase in power, increasing by 7 orders of magnitude from the inital *NoShock* spectrum. By 2.21 Myrs, the spectrum has increased beyond the *NoShock* values on all scales and by 5.16 Myrs, except for fluctuations captured between $2 < k < 20$ ($75 > l > 7.5$ pc), the spectrum appears mostly flat.

Examining the logarithm of the density in Fig. 5.1(c), the spectra look a lot more stable. Except for the largest scales, they do not vary significantly in overall power between snapshots, and do not flatten as the cloud evolves. A bump is seen around $k = 30$ ($l = 5$ pc), likely reflecting the high density clumps on those scales, and the deceleration of the surrounding flow across the warm − cold phase boundary. The logarithm spectrum certainly appears to show K41-like behaviour in an inertial range of $1 < k < 20$ ($150 > l > 7.5$ pc). This is in agreement with Kowal *et al.* (2007) who find logarithmic density spectra show this behaviour when the regular density spectra do not.

5.3.1.2 *24Shock* interaction

Turning now to Fig. 5.2, we focus on the behaviour of the spectra in the *24Shock* scenario. Similar to the *12Shock* scenario, the velocity spectra in Fig. 5.2(a) show that the shock injects a substantial amount of power, and a large inertial range spanning all scales can initially be seen. The slope once more follows a power law somewhat close to the B48 $\alpha = -2$. As mentioned previously, this is likely simply due to the presence of the shock, as a Fourier transform of a perfect step function gives a slope of $\alpha = -2$. Note that the *NoShock* spectrum displays more turbulence-like behaviour at this time also, most likely due to the presence of

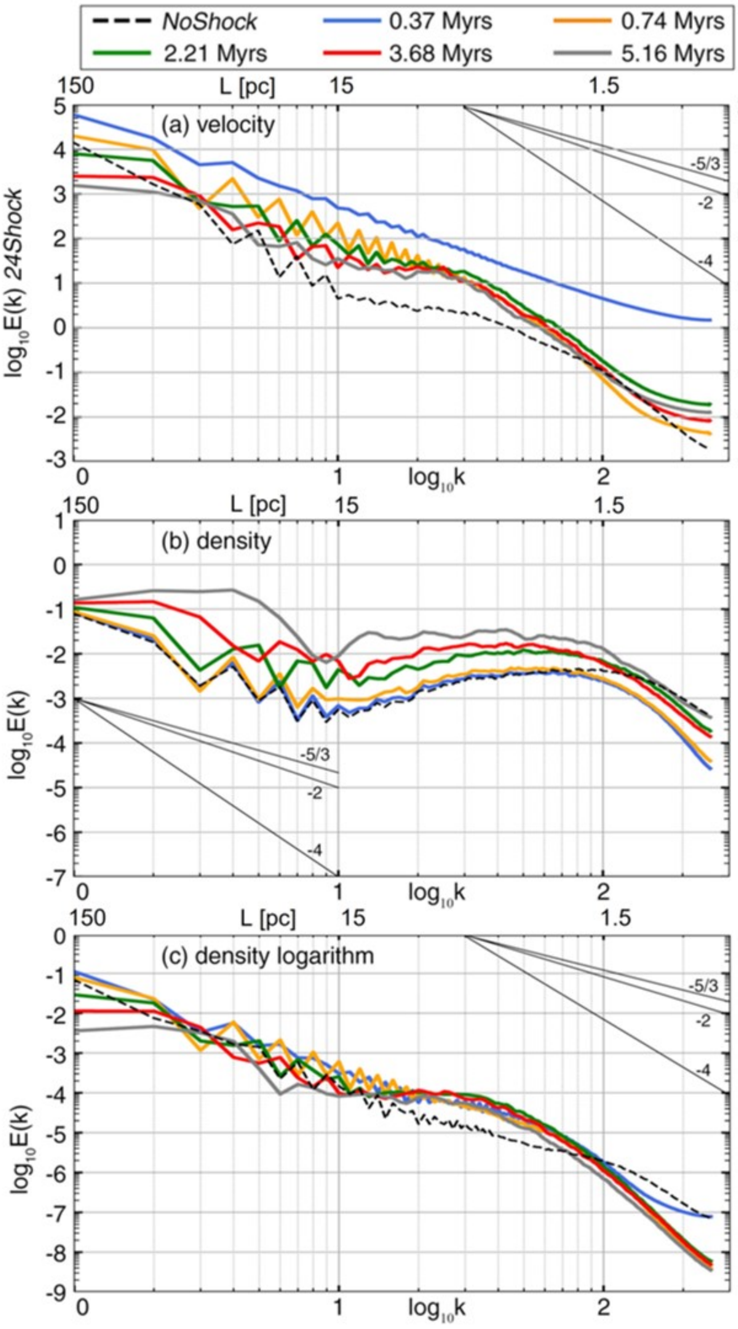

Figure 5.2: Shown are power spectra of velocity (panel a), density (panel b) and the density logarithm (panel c) for the *24Shock* scenario. The colours correspond to snapshots at times since shock introduction $t_{\mathrm{shock}} = 23.57\,\mathrm{Myrs}$, and the black dashed line corresponds to the *NoShock* spectrum at t_{shock}. In panel (a) the *NoShock* spectrum scale is shown on the right y-axis, whilst the *24Shock* spectra correspond to the left y-axis. The *NoShock* scenario considered in these panels is that from Chapter 3 also. The K41 -5/3, B48 -2 and a -4 slope are shown for comparison.

already formed clumps.

A 0.74 Myrs, the spectrum loses power on all scales, with the biggest drop occurring at $k > 30$ ($l < 5\,\mathrm{pc}$). After this however, little change is seen in the velocity spectra on these scales. Most of the subsequent changes are seen for $k < 30$ as the slope appears to approach an index somewhat closer to a K41 $\alpha =$-5/3. It does not look as though this happens due to power increasing at the larger k range, up to $k = 30$, indicative of an energy cascade, but instead due to power diminishing on small k (large scales). This is most likely due to the cloud shrinking in overall size as it is compressed by the external pressure, resulting in less power on larger scales. This is also seen in the *12Shock* spectra, however not to the same extent as the cloud is initially larger and ultimately not compressed as much as *24Shock*

Examining the behaviour at and after 0.74 Myrs in more detail, we see that it is very similar to *12Shock* also. This is interesting, because the *12Shock* and *24Shock* interactions are very different. The break at $k \approx 30$ ($l \approx 5\,\mathrm{pc}$) is more obvious to interpret here than in *12Shock*, as the only possible mechanism for it is the deceleration of flow across the phase boundary between the interclump medium and the clumps. The effect of the clumps is two fold however, as they also prevent the formation of the dynamical instabilities seen in *12Shock*. This will inevitably contribute to the bigger drop in energies on larger scales than what was seen in *12Shock*, simply because the instabilities that maintained energies at those scales are not there. Finally, just like *12Shock*, on scales $6 < k < 30$ ($24 > l > 5\,\mathrm{pc}$), the velocity spectra appear to settle into a turbulence-like slope with $-2 < \alpha < -5/3$. Inspecting the velocity field does indeed show chaotic flow patterns within the cloud, although large scale order is also present in the flow.

Examining Fig. 5.2(b), we see more differences between the *24Shock* and *12Shock* density spectra than in the velocity spectra. Firstly, the *NoShock* spectrum is already much flatter than in *12Shock* due to the presence of clumps. Over the next 0.74 Myrs, the *24Shock* spectrum remains almost identical to the *NoShock* spectrum on all scales where $k < 70$ ($l > 2.14\,\mathrm{pc}$), showing the initial impact of the shock is not effective in altering the density spectra. In contrast, the initial impact of the shock caused more dramatic changes in the *12Shock* scenario. We note that the change at large k is due to the action of changing the Riemann solver from Godunov (Godunov, 1959, hereafter GOD) to Kurganov-Tadmor (Kurganov & Tadmor, 2000, hereafter KT), as was done in the simulations in Chapter 3.

After 0.74 Myrs, the spectra experience an increase in power on all scales. The rate of increase is much smaller than what was seen in *12Shock*, likely due to the strong increase in cold material that *12Shock* experienced, which was not so much the case with *24Shock*. Recall that the clumps were initially mostly resistant to the flow, and in all the thermodynamic phases only small subsequent changes were seen. It is interesting to observe that a peak in the spectrum emerges at low k, with the final snapshot at 5.16 Myrs showing a peak at $k \approx 4$ ($l \approx 37.5\,\mathrm{pc}$). This is the signature of the cloud compression, as more mass overall becomes concentrated in a smaller volume and at the final snapshot the cloud has a diameter $\sim 30\,\mathrm{pc}$.

Turning to the density logarithm, we see from Fig. 5.2(c) that the *NoShock* spectrum at the moment preceding the shock injection already appears to contain a large inertial range within the interval $1 < k < 50$ ($150 > l > 3\,\mathrm{pc}$). This is reflective of the turbulence-like appearance that the thermal instability alone has generated (WFP19). Upon shock impact, the spectrum then increases in power over all scales, with the smallest scales showing behaviour reflecting the changes of Riemann solver. A bump develops around $k \approx 30$ ($l \approx 5\,\mathrm{pc}$) which remains as a consistent break during the full evolution of *24Shock*. This length-scale is likely a reflection of the clump scale, however it is interesting to observe a lack of this break in the *NoShock* spectrum. Further work needs to be done to investigate the significance of this to determine whether this again is simply the effect of changing the Riemann solver, e.g. the more diffusive KT solver causes clump envelopes to expand slightly, registering as a break at a different location to the GOD solver (a break can be seen at $k \approx 100$, $l \approx 1.5\,\mathrm{pc}$ in the *NoShock* spectrum). Just like in *12Shock* however, the general behaviour is again that the spectra are much more stable, although stronger shallowing can be seen towards the final snapshots - likely due to the cloud being a smaller size than *12Shock* to begin with. K41-like appearance in an inertial range of $1 < k < 30$ ($150 > l > 5\,\mathrm{pc}$) can be seen, again in agreement with Kowal *et al.* (2007).

5.3.2 Supernova-cloud scenarios

We now present the power spectra of the supernova-cloud scenarios *SN1* (Fig. 5.3) and *SN2* (Fig. 5.4). In both figures, spectra are shown for the velocity amplitudes in panel (a), density in panel (b) and density logarithm in panel (c). Just like in the previous sub-section, the *NoShock* spectrum is shown at the time of injection in all panels, and then 5 subsequent snapshots of the supernova-cloud spectra are shown. In the velocity spectra, the supernova can be seen to have injected a large amount of energy on all scales, and as such the right y-axis scale in figures 5.3(a) and 5.4(a) corresponds to the *NoShock* scenario only, and the left y-axis for *SN1/2* scenarios. The scale on all other panels is the same for both the *NoShock* and supernova-cloud scenarios.

5.3.2.1 ***SN1* interaction**

Turning first to the *SN1* velocity spectrum in Fig. 5.3(a), we can see that the supernova impact has resulted in a large inertial range on scales $k > 3$. The slope in this range appears to be steeper than the B48 $\alpha = \text{-}2$, with an index roughly

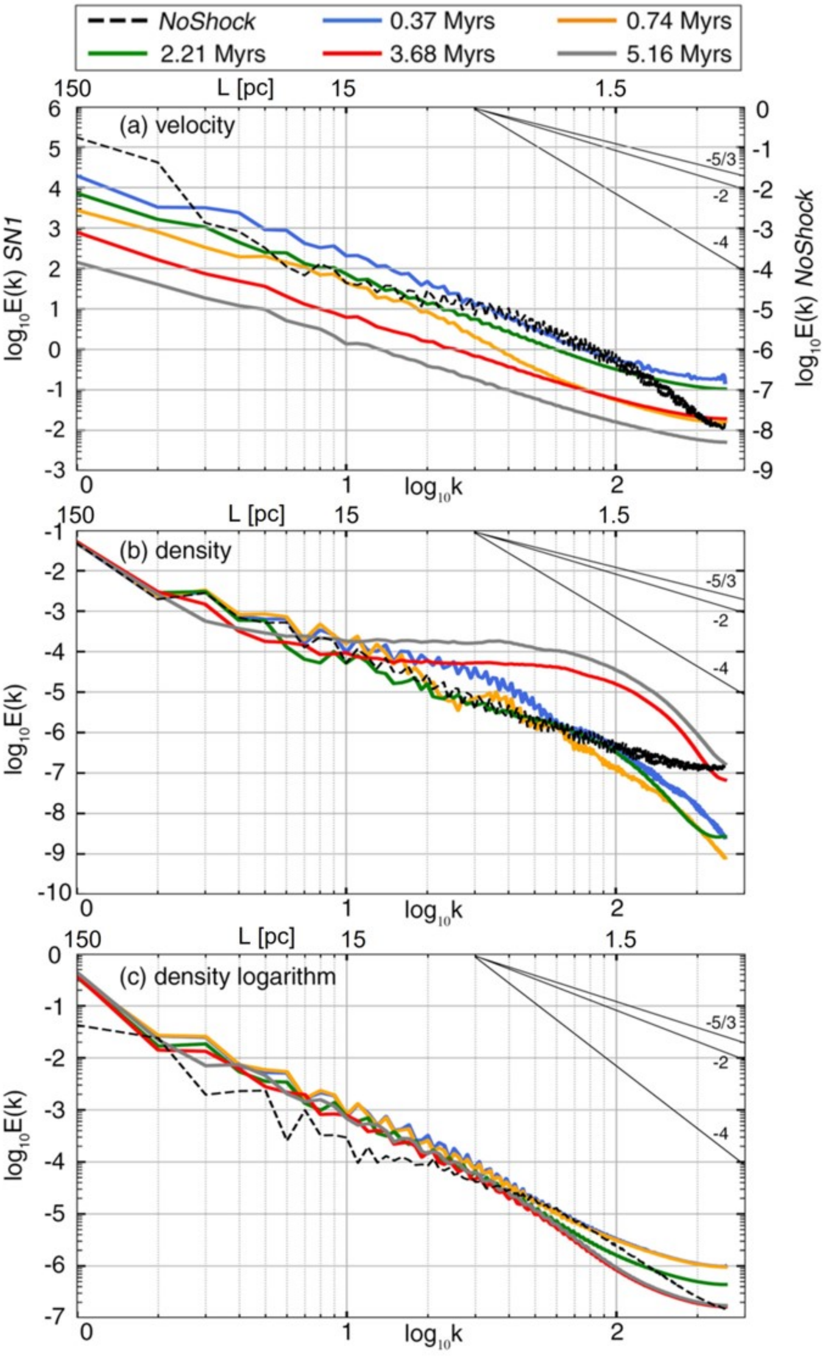

Figure 5.3: Shown are power spectra of velocity (panel a), density (panel b) and the density logarithm (panel c) for the *SN1* scenario. The colours correspond to snapshots at times since supernova injection $t_{\mathrm{inj}} = 11.78$ Myrs, and the black dashed line corresponds to the *NoShock* spectrum at t_{inj}. In panel (a) the *NoShock* spectrum scale is shown on the right y-axis, whilst the *SN1* spectra correspond to the left y-axis. Note that the *NoShock* scenario considered in these panels is that from Chapter 4. The K41 -5/3, B48 -2 and a -4 slope are shown for comparison.

$\alpha \approx$-3. This is interesting, as this is steeper than the *NoShock* spectrum prior to impact which has an index slightly exceeding -5/3. This *NoShock* index certainly suggests that turbulence could have been there prior to supernova injection, and the supernova has removed this turbulence. This is of course not true, as the cloud was effectively quiescent prior to injection, and the supernova injects substantial kinetic energy to the material in the cloud. Note however that it is inconclusive to what extent the supernova driven flows can be described as turbulent, as the shock flow is roughly laminar, with only a small number of distinct eddies present at the front of the cloud. This is contrasted by the spectrum behaviour, as it appears to approach, and remain at a B48 $\alpha =$-2 slope from 2.21 Myrs. It is likely therefore that the spectra are incorrectly reflecting this dynamical behaviour and important details are lost in this analysis.

At 0.74 Myrs, a very distinctive drop in the spectrum can be seen at $k > 20$ ($l < 7.5\,\mathrm{pc}$). No structure has formed at this stage, and so this drop cannot be explained by the deceleration of flow across the phase boundary as was seen in WFP19, WPF21 and the *24Shock* scenario. The only other possible physical origin of this dip is due to radiative cooling experienced in the post-shock layer at the front of the cloud, where the impact was the strongest, and the cooling timescale the shortest. It is in this region that cold structure forms, which appears to be reflected by the energy increase in the subsequent spectra. In fact, the spectrum appears to increase on all scales, which is most likely associated with the development of the convergent flow at the front of the cloud - adding a small amount of energy to larger scales and also accelerating the cold material.

It is interesting that for the final 3 Myrs the energy of the spectrum drops globally on all scales while maintaining a slope that appears to be very close to the B48 $\alpha =$-2. It is difficult to interpret this as something akin to B48 turbulence however, as the shock flow internal to the cloud is laminar, the convergent flow at the front of the cloud is laminar, and flows due to the global expansion of the cloud are laminar. There is indeed a shock present in these simulations at all times, and as commented on, shocks alone give an $\alpha = \text{-}2$ slope. However, this is internal to the cloud and the size of the region that the shock occupies decreases, with no known shocks being present in the ambient medium. Additionally, the shock is radiative and is being driven by a flow with a Sedov-Taylor-like profile, rather than a step function. Thus one might expect a shock with such behaviour to register as a feature that moves into regions of increasing k on the velocity spectrum, and not a global dropping spectrum with constant slope. It thus makes this spectral behaviour difficult to interpret, and as mentioned, certainly difficult to claim that what the spectrum shows is supersonic compressible turbulence, as an $\alpha = \text{-}2$ B48 slope predicts. Clearly further work needs to be done into how to interpret such spectra.

Turning to Fig. 5.3(b), we see the behaviour of the density spectrum. Post supernova impact, there is a drop in energy on lower scales at $k > 60$ ($l < 2.5\,\mathrm{pc}$), and they remain below the *NoShock* spectrum for the next 2.21 Myrs. Meanwhile, a sudden increase in energy is seen at $10 < k < 60$ ($15 > l > 2.5$), which drops down to, and stays at the *NoShock* values over the subsequent $\sim 2\,\mathrm{Myrs}$. The initial drop in power on small scales is likely due to the presence of densities with values of the order of $10^{-4}\,\mathrm{cm}^{-3}$ at the surface of the cloud generated by the expansion that trails behind the reflected primary shock. Densities in the interior of the remnant are of this order of magnitude also which will be contributing to the drop. As structure forms in the cloud and more material enters the cold phase, the spectrum flattens and increases energy on scales above $k > 10$ ($l < 15\,\mathrm{pc}$), and appears to drop below the *NoShock* spectrum at k smaller than this, conducive with the gradual expansion of ambient gas as the pressure gradients left behind after the passage of the remnant attempt to return to an equilibrium. Whilst regions of the spectra appear to match a K41 slope of $\alpha = -5/3$, especially at 2.21 Myrs, this is short lived and is followed by a further flattening of the spectrum, as seen in the shock-cloud scenarios.

The density logarithm behaves much differently to this. Where the density overall increased on all scales, the density logarithm appears to decrease. The decrease is strongest at $k > 100$ ($l < 1.5\,\mathrm{pc}$) and minimal below $k < 40$ ($l > 3.75\,\mathrm{pc}$). At $k < 40$, the spectrum is very stable, and continuously exhibits a slope slightly steeper than the B48 $\alpha = -2$. It is not entirely clear what is responsible for the difference in how the power spectra of density and density logarithm change, however the differences in stability of the spectra is aligned with expectations (see e.g. Kowal *et al.*, 2007). In any case, as established through inspecting the dynamics, we do not see any turbulence-like behaviour in our clouds, with most flows being laminar.

5.3.2.2 *SN2* interaction

A similar situation to *SN1* is seen in the *SN2* scenario. Examining first the velocity spectrum in Fig. 5.4a, we again see the supernova adds a considerable amount of energy on all scales, with a relatively steady inertial range for $k > 4$ ($l < 37.5\,\mathrm{pc}$) with a slope $\alpha \approx -3$. The spectrum subsequently loses energy on all scales, with the largest decreases occurring for $k > 30$ ($l < 5\,\mathrm{pc}$), likely due to cooling processes. It is interesting to note again that whilst the remainder of the spectrum stays the same, wave numbers of $k > 30$ experience a subsequent increase in energy, just like in *SN1*. The $10\,\mathrm{km\,s^{-1}}$ flow along the cloud interface converges at the front at this timescale and more of the cloud is shocked. It is likely therefore that this is what causes the increase. Once this energy is replenished, just like *SN1*, the final 3 Myrs of evolution results in a gradually dropping velocity spectrum with an approximately constant B48 slope of $\alpha \approx -2$.

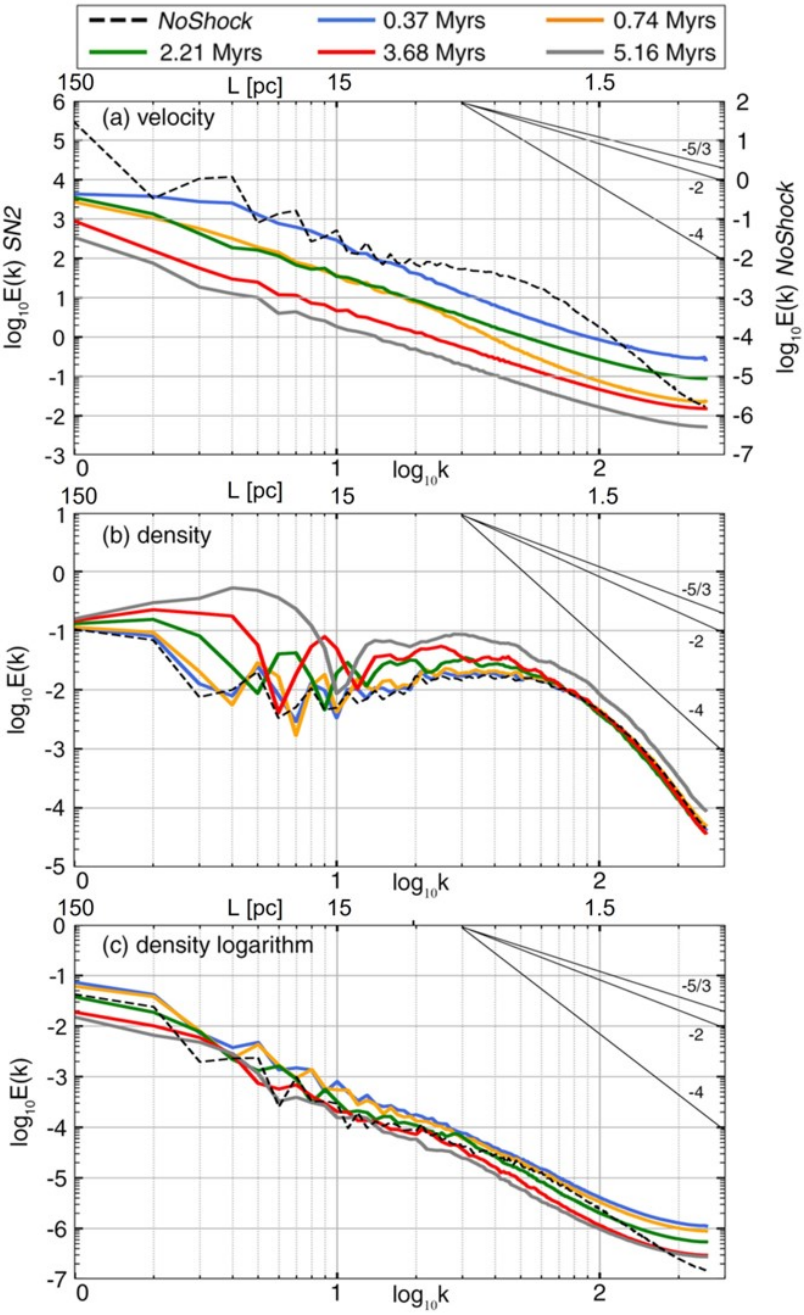

Figure 5.4: Shown are power spectra of velocity (panel a), density (panel b) and the density logarithm (panel c) for the *SN2* scenario. The colours correspond to snapshots at times since supernova injection $t_{\rm inj} = 26.5$ Myrs, and the black dashed line corresponds to the *NoShock* spectrum at $t_{\rm inj}$. In panel (a) the *NoShock* spectrum scale is shown on the right y-axis, whilst the *12Shock* spectra correspond to the left y-axis. Note that the *NoShock* scenario considered in these panels is that from Chapter 4 also. The K41 -5/3, B48 -2 and a -4 slope is shown for comparison.

The density and density logarithm spectra behave in a similar fashion to *SN1* also, however this time the *NoShock* cloud consists of a complex of cold and dense clumps embedded in a warm diffuse gas. Thus this is registered as an already flattened spectrum, roughly within the range $2 < k < 20$ ($75 > l > 7.5\,\mathrm{pc}$) followed by an increase in power up to a peak at $k \approx 40$ ($l \approx 3.75\,\mathrm{pc}$) corresponding to the size of the clumps, after which a steep slope of -4 follows. The spectrum subsequently increases in energy on all scales by the time the simulation is stopped. An increase in the density is accompanied by a global decrease in the density logarithm (Fig 5.4c). This decrease is more pronounced than it was in *SN1*, and is seen to happen on all scales. This maintains the slope at values between -2 and -5/3, and a steeper value is somewhat visible for $k > 30$ ($l < 5\,\mathrm{pc}$), likely reflecting the size of the clumps.

The flows in *SN2* could be considered more turbulent-like than in *SN1*, since internally the clumps distort the passage of the shock, meaning the flow is less laminar, and there are already pre-existing velocities present in the cloud during this time. As discussed in Chapter 4, after $\sim 3.5\,\mathrm{Myrs}$, the cloud is almost indistinguishable from a *NoShock* cloud. Turbulence-like spectra are thus not too surprising, as it was shown that it is possible for such clouds to exhibit power spectra like this in WFP19.

5.4 Conclusion

In this chapter we perform a Fourier analysis to obtain power spectra of the velocity, density and density logarithm of the models considered in this Thesis. Specifically, power spectra were derived for the *12Shock* and *24Shock* scenarios from Chapter 3 and the *SN1* and *SN2* scenarios from Chapter 4. Our goal was to take advantage of the fact that we have a reasonable understanding of the dynamics in those models, and investigate if any connections can be made between the cloud dynamics and the spectra. Specifically, we look to see if the spectra contain inertial ranges that scale as $E(k) \propto k^{\alpha}$ with constant value of α, allowing us to identify the physical behaviour responsible for such spectra and possibly gain insight into their nature. A value of $\alpha =$ -5/3 corresponds to subsonic, incompressible hydrodynamic turbulence (Kolmogorov, 1941, hereafter K41) and the value $\alpha =$ -2 corresponds to supersonic, compressible hydrodynamic turbulence (Burgers, 1948, hereafter B48).

While self-similar scaling is seen in many of the spectra, it is challenging to interpret this as representing turbulence in every case. Just as was found in KWPF21, different dynamics are able to show similar spectral behaviour, implying that important details may be lost in the analysis. Nevertheless, a very wide range of interesting spectral behaviour can be seen, and general features do appear to be captured.

In both shock-cloud interactions, velocity power spectra show a B48 $\alpha =$ -2 slope for a period of $\sim 400\,\mathrm{kyr}$ after shock impact. This is not reflective of compressible supersonic turbulence however, but simply corresponds to the presence of a shock on the grid, as confirmed by tests that looked at the Fourier transform of the shock only. Both shock-cloud interactions display subsequent velocity spectra with turbulence-like behaviour with a slope somewhere between the K41 $\alpha =$ -5/3 and B48 $\alpha =$ -2, roughly spanning just over a decade in wave number with a break around $3 < l < 5\,\mathrm{pc}$. Inspecting the velocity field indeed shows a mixture of laminar and turbulent-like flows, especially around regions influenced by dynamical instabilities. Both supernova-cloud interactions show a 3 Myr period with B48 $\alpha =$ -2 slope also. This is very interesting since in the *SN1* scenario almost all flows are laminar during this period. More believable is the *SN2* spectrum as it is likely capturing the pre-existing thermal flows and the distortions of the shock as it passes over clumps. Once again however, we observe that very different fluid dynamics give rise to similar spectra.

The density spectra show drastic differences when compared to the velocity spectra. With increasing time, they show significant flattening and a gain in power across all length scales. This is in line with predictions in the literature (e.g. Kritsuk *et al.*, 2007; Federrath & Klessen, 2013; Kowal *et al.*, 2007). As also predicted by those authors, our density logarithm spectra behave differently: they are stable, and in all models show turbulence-like slopes. In our shock-cloud models, these are mostly achieved not by an energy increase on small scales, indicative of an energy cascade, but due to energy decreasing on large scales. Thus the spectra are likely capturing the overall compression of the cloud due to the external flows. This is likely what is captured in the spectrum for the *SN2* scenario as the cloud is compressed also, however it is inconclusive what causes this behaviour in *SN1*, as the cloud expands. Further investigation is clearly required.

The dynamics in every scenario is different, thus while the spectra most likely correctly capture the turbulent nature of the flows where they exist, many details are lost. Most strangely, in the *SN1* scenario, all flows are laminar, as such further investigation is needed to elucidate the reason for a turbulent-like spectrum. Thus as mentioned, a similar conclusion can be drawn here as it was in KWPF21: the spectra appear to be unable to convey the key information about the nature of the interactions, with different interactions showing similar spectra. Clearly more work is required than is shown in this chapter however, as power spectra are not the only statistical description important for understanding molecular clouds and star formation more broadly. Single point statistics, such as density probability distribution functions, are also used alongside two point statistics such as autocorreleation functions and power spectra, which are all important in numerical and analytical models of star formation (Mac Low & Klessen, 2004a).

Chapter 6

Conclusions

6.1 Summary

In this Chapter we summarise our approach, findings, and provide a discussion with suggestions for potential future work.

In this Thesis, using the MG code we numerically studied the relative importance between the thermal instability (TI), gravity and shock impact in the process of molecular cloud (MC) formation out of an initially quiescent atomic medium. Our models built on earlier work in our group (Wareing *et al.*, 2016a, hereafter WPFVL16), who using numerical simulations showed that even in isolation, the TI is an effective mechanism for forming MCs out of a diffuse atomic medium, and is able to generate clumps with properties that match observations. The clouds in WPFVL16 were left undisturbed by any external events for $\sim 50\,$Myrs, and so it is of interest to investigate deviations from such an idealisation. As the role of the TI was extensively studied by WPFVL16, combining it with the extensively studied shock-cloud problem is one appropriate step to take, and one I decided to take here.

A total of five scenarios were considered in this Thesis. These were an unshocked scenario, two planar shock-cloud scenarios in the *small cloud regime* in Chapter 3, and two supernova-cloud scenarios in the *large cloud regime* in Chapter

4. The regimes were defined in terms of the distance of the shock wave origin away from the nearest cloud edge, and allowed us to study shock-cloud interactions in two very extreme circumstances. Additionally, the shock was introduced at two different times: when the cloud was in a "pre-TI" warm atomic state prior to any noticeable action of the TI, and a "post-TI" state after cold and dense clumps have formed. This allowed us to study the effects of the presence/absence of clumps on the resulting dynamics. In Chapter 5 we took advantage of the fact that the dynamics in the models were well understood in the previous chapters, and via a Fourier analysis derived the power spectra of velocity, density and density logarithm. This allowed us to understand how the dynamics were reflected in the spectra, and if any turbulence was present, as reflected by spectra containing inertial ranges of constant slope.

6.1.1 Chapter 3: Shock-cloud interactions in the small cloud regime

We first turn to summarise our results from Chapter 3 where the un-shocked *NoShock* scenario was considered, and scenarios where a shock with Mach 1.5 impacts a "pre-TI" cloud (*12Shock*) and a "post-TI" cloud (*24Shock*).

Both *12Shock* and *24Shock* showed early and sustained evidence of local gravitational collapse on a timescale of ~ 5 Myrs since shock introduction, successfully demonstrating the capacity for star formation in the clouds. This is interesting, since local collapse was not seen in the *NoShock* cloud, despite the 4.5 Myr free-fall timescale for gas with $n = 100\,\mathrm{cm}^{-3}$, which the *NoShock* cloud contained after ≈ 15 Myr - only global collapse on an ≈ 35 Myr timescale was seen. More massive clouds like that in *NoShock* did show local collapse in Wareing *et al.* (2019) however, clearly indicating that this difference between *NoShock* and Wareing *et al.* is due to the *NoShock* clumps being unable to accumulate enough mass to take them over the Jeans limit, requiring additional compressive mechanisms to do so, such as that due to a shock like in my work. Where this threshold lies, beyond which no compressive devices are needed to induce local gravitational collapse, would be an interesting exploration for future work, and could prove valuable insight to the study of global hierarchical collapse (Vázquez-Semadeni *et al.*, 2019).

Focusing now on each case individually, the first thing to note is that in the *12Shock* scenario, the shock prevented the TI from developing. Instead what we saw was gas being shocked into the thermally unstable regime, and subsequent cooling directly to the cold phase. Some shocked regions appeared to have a higher potential for TI triggering than others, especially where the shock was the weakest, however the instability was prevented from developing there due to repeated shocking of gas on a cloud-crushing timescale. Where the shock was the strongest, the radiative cooling and compression resulted in the formation of a cold, thin and dense shell. This fragmented due to dynamical instabilities, with some regions originating from the rear of the cloud eventually collapsing due to gravity.

Turning now to *24Shock*, we first point out that the TI-formed clumps played quite a significant role, but were not too strongly disturbed by the shock itself, at least to begin with. Primarily, they strongly influenced the structure of the velocity field, as external flows were directed via low density inter-clump channels. Inspecting the velocity field visually showed it to appear turbulent-like, with lots of un-ordered regions of flow. There was still some larger scale order, however, as the majority of the flow was directed through the channels to the centre of the cloud, and back upstream against the cloud drag. The flows in the cloud substantially increased the probability of clump-clump interactions, and these occurrences were largely responsible for the first instances of local gravitational collapse.

In our models, the shocked molecular clouds remained starless for ~ 5 Myrs in the *12Shock* scenario and ~ 15 Myrs in the *24Shock* scenario, reflecting the possible lifetimes of molecular clouds prior to star formation.

6.1.2 Chapter 4: Supernova-cloud interactions in the large cloud regime

In Chapter 4 we performed an analogous study to the previous chapter but this time in the *large cloud regime*. Namely, the idealised planar shock was replaced by a $10\,M_\odot$ and 10^{51} erg detonation at a distance of 50 pc away from the nearest cloud edge, reflecting a realistic supernova event. All five scenarios were considered in this chapter, consisting of the un-shocked scenario *NoShock*, two re-simulated shock-cloud scenarios *S1/S2* (analogous to *12Shock/24Shock* in Chapter 3), and two supernova-cloud scenarios *SN1/SN2* at equivalent timescales as *S1/S2* (i.e. impact with pre-TI and post-TI clouds, evolved for ≈ 5 Myrs). Like previously, we studied the relative importance of the TI, gravity and supernova impact, but now compared and contrasted the models not only to the *NoShock* scenario, but also to the *S1/S2* scenarios in the *small cloud regime*.

For our chosen parameters, upon impact the Mach number of the supernova shock was ≈ 7, and this was stronger than the planar shock roughly by a factor of 4.5, which had a Mach number of 1.5. On aggregate however, the supernova was significantly less disruptive than the sustained impact from the idealised post-shock flow. Since *S1/S2* were in the *small cloud regime*, the post-shock flow was constantly replenished and approached the cloud at $\sim 100\,\mathrm{km\,s^{-1}}$. This provided a ram pressure that consistently throughout the simulation was at least a factor of 100 higher than that due to the $\sim 10\,\mathrm{km\,s^{-1}}$ flows that developed around the cloud in *SN1/SN2*. A constantly replenished flow also meant that in *S1/S2* the ambient thermal pressure was maintained at higher values than those in the cloud, resulting in continuous compression throughout the entire simulation. *SN1/SN2* were a strong contrast to this, where the compression dropped strongly due the Sedov-Taylor-like profile in the interior of the remnant, causing the ambient pressure to drop below the cloud's after 1 Myr.

In the *SN1* scenario, the ambient pressure drop after the passage of the shocks resulted in the expansion of the cloud. The edges expanded everywhere at the same rate, except at the front where an upstream flow had developed that halted the expansion and gave the cloud a lobe-like morphology. This unique evolution, and a lack of oncoming flow meant that the Rayleigh-Taylor, Vishniac and Kelvin-Helmholtz instabilities were not triggered, which were fundamental to the *S1/S2* evolution. Internally, where the impact was the strongest, the TI appeared to be triggered which formed a cap-like structure with clumps embedded inside. We concluded however that we would not expect any star formation in this scenario, at the very least on the same timescales as in *S1*, as the maximum densities obtained were $100\,\mathrm{cm}^{-3}$.

In the *SN2* scenario the decrease of the ambient pressure was followed by even more surprising behaviour. The shock had almost no effect on the cloud at all. In fact, after ~ 3.5 Myrs from the initial disturbance, the cloud recovered into a state that was almost indistinguishable from the *NoShock* cloud. The only signatures of the supernova remnant were seen in the warm medium morphology, and the formation of tail-like structures in the clumps nearest to the cloud edge as they appeared to be ablated by the transmitted shock. After the transmitted shock passed the outer edge clumps, the interclump medium dropped in pressure, which resulted in some clumps expanding and merging with neighbouring clumps. This however did not raise the maximum density in the cloud, thus doing little to aid the possibility of further star formation beyond that expected due to the trivial collapse of the entire cloud (as dictated by the initial condition).

6.1.3 Chapter 5: Turbulence analysis

In Chapter 5 we performed a Fourier analysis to obtain power spectra of velocity, density and density logarithm of the *12Shock* and *24Shock* scenarios from Chapter 3, and the *SN1* and *SN2* scenarios from Chapter 4. Our goal was to take advantage of the fact that we understood those models reasonably well, and investigate if any connections could be made between the cloud dynamics and the spectra. Specifically, we wanted to see if the spectra contained any inertial ranges that scaled as $E(k) \propto k^{\alpha}$ with constant value of α, and whether we could identify the physical behaviour responsible for such spectra. Recall that a value of $\alpha =$-5/3 corresponds to subsonic, incompressible hydrodynamic turbulence (Kolmogorov, 1941, hereafter K41) and the value of $\alpha =$-2 corresponds to supersonic, compressible hydrodynamic turbulence (Burgers, 1948, hereafter B48).

While self-similar scaling was seen in many of the spectra, it was challenging to interpret this as representing turbulence in every case, with some spectra showing misleading results altogether. In *12Shock* and *24Shock* for example, velocity power spectra showed a B48 $\alpha =$-2 slope for a period of $\sim$400 kyr after shock impact. This was not due to any compressible supersonic turbulence being present in the simulations, but simply due to the presence of a shock on the grid, as confirmed by tests that looked at the Fourier transform of the shock only. Subsequently, both scenarios displayed velocity spectra with turbulence-like behaviour, with a slope somewhere between the K41 $\alpha =$-5/3 and B48 $\alpha =$-2, roughly spanning just over a decade in wave number with a break around $3 < l < 5$ pc. Around regions influenced by dynamical instabilities, the velocity field was indeed turbulent-like.

Both supernova-cloud interactions showed a period of 3 Myr with a B48 $\alpha =$-2 slope also, which was interesting, since in the *SN1* scenario almost all flows were laminar during this period. More believable were the *SN2* spectra, as they likely captured the pre-existing thermal flows due to the thermal instability, and the distortions of the shock as it passed over clumps. The density spectra showed drastic differences when compared to the velocity spectra, displaying significant flattening with increasing time. The density logarithm spectra were stable however, and in all models showed turbulence-like slopes.

It appeared that turbulence-like spectra in our shock-cloud models were mostly achieved not by an energy increase on small scales, indicative of an energy cascade, but by an energy decrease on large scales, shallowing the slope to something approximating an α of -5/3. There the spectra were likely capturing the overall compression of the cloud, which is likely what was being captured in the *SN2* spectra too as the cloud was shrinking due to gravitational contraction. It was inconclusive what caused this behaviour in the *SN1* scenario, as the cloud expanded.

6.2 Final remarks and possible future work

To our knowledge, the works presented in this Thesis are the first systematic studies of the impact of a shock on a cloud that is evolving due to the TI and gravity, where comparisons are made between shocked and un-shocked clouds and small and large cloud regimes. Our work has significance in elucidating the role of the TI, supernovae and gravity in the early stages of star formation and ISM evolution, thus it is very interesting to see such a vast array of surprising behaviour.

One would expect that all else being equal, the closer a blast source is to an object, the stronger the impact. Indeed, studying the impact of supernovae on molecular cloud velocity dispersions, Seifried *et al.* (2018) found that doubling

R_{c} decreased the maximum impact by roughly 40%. It is interesting therefore to observe planar shocks significantly disrupting clouds in the *small cloud regime*, while appearing not to have much of an impact in the *large cloud regime*, especially given that the *small cloud regime* is often employed as an approximation to supernova remnants. It is useful therefore to consider how reflective simulations in the *small cloud regime* are of realistic astrophysical systems.

To illustrate this with our models, it is worth considering again how the boundaries between the regimes were defined in Chapter 1. A cloud with radius r_{cl}, density contrast χ, and blast source distance R_{c} (from nearest cloud edge) qualifies for the *small cloud regime* if the parameters satisfy $r_{\mathrm{cl}} \ll 0.1 R_{\mathrm{c}}/\chi^{1/2}$, the *medium cloud regime* if they satisfy $0.1 R_{\mathrm{c}}/\chi^{1/2} \lesssim r_{\mathrm{cl}} \lesssim 0.05 R_{\mathrm{c}}$, and the *large cloud regime* if they satisfy $r_{\mathrm{cl}} > 0.05 R_{\mathrm{c}}$.

At the time of impact, $\chi \approx 500$ evaluates the first equation to $r_{\mathrm{cl}} \ll 0.0047 R_{\mathrm{c}}$, requiring a cloud to have a radius that is at an absolute maximum 0.5 % the size of R_{c} to qualify for the *small cloud regime*. For clouds like ours with $r_{\mathrm{cl}} = 50\,\mathrm{pc}$, this requires a minimum $R_{\mathrm{c}} \approx 11\,\mathrm{kpc}$, which is clearly unrealistic for a single supernova. In fact, using equation (39.31) in Draine (2011) to calculate the "fade-away radius" R_{fade} - the theoretical length-scale at which the shock Mach number falls below unity and a supernova remnant mixes with the ISM, we get $R_{\mathrm{fade}} \approx 200\,\mathrm{pc}$ for our $10\,\mathrm{M}_{\odot}$, $10^{51}\,\mathrm{erg}$ supernova exploding into a medium with $n_{\mathrm{amb}} = 0.0022\,\mathrm{cm}^{-3}$. Using R_{fade} to approximate the maximum distance that R_{c} can take that would lead to an interaction with a cloud, only clouds with $r_{\mathrm{cl}} \ll 1\,\mathrm{pc}$ would fall into the *small cloud regime*. Clearly, our *12Shock/24Shock* and *S1/S2* models are not representative of a supernova like that seen in *SN1/SN2* exploding far away.

It is clear that a necessary condition for a supernova explosion to represent something approximating a wind-like flow like that in a shock-cloud system is a supernova rate of 1 every $t_{\rm P}$, where $t_{\rm P} \simeq 0.1 R_{\rm c}/v_{\rm b}$ approximates the variation timescale of the shock-driving pressure in a supernova remnant (McKee *et al.*, 1987; Klein *et al.*, 1994). Thus whilst a single supernova may not drive the kind of wind seen in *S1*/*S2*, a superbubble due to a cluster of supernovae might. Given the size of our clouds, it is likely that our *S1*/*S2* scenarios are thus more reflective of the kinds of clouds embedded in galactic winds and superbubbles due to clusters of supernovae (e.g. Fielding *et al.*, 2018). However, given typical wind speeds ($500-1500\,{\rm km\,s^{-1}}$) and molecular phase speeds ($50-300\,{\rm km\,s^{-1}}$) observed in such systems (see e.g. Strickland & Heckman, 2009; Rupke, 2018), it is unclear what region of the parameter space our models occupy.

Thus many avenues of exploration remain, and we provide some suggestions here. Some immediate extensions to the work could involve exploring the parameter space between the small and large cloud regimes, by varying the distance of a single supernovae (e.g. Seifried *et al.*, 2018), and by varying the supernova rate from a single supernova, to whole clusters of supernovae (e.g. Padoan *et al.*, 2016). Additionally, as the final "goal" of such a cloud is to form a star, it would be helpful to consider the impact of increasing the cloud mass, as larger clouds similar to ours showed higher potential for star formation (Wareing *et al.*, 2019), and could thus show interesting behaviour when impacted by a shock. Considering different cloud shapes would be helpful also, as clearly a large factor impacting the dynamics in our models is the initial spherical shape of the cloud. Exploring an initial condition of a filament-like cloud could therefore prove insightful (e.g. Goldsmith & Pittard, 2020), as well as the inclusion of magnetic fields, which have been demonstrated to form filaments from clouds like ours (Wareing *et al.*, 2016a, 2021). For those less interested in the assembly stage of a molecular cloud, the shock-cloud scenarios in this work showed evidence of local gravitational collapse, and are thus very amenable for the study of stellar feedback and cloud dispersal.

We also have suggestions with how to improve the turbulence analysis presented in Chapter 5. Firstly, power spectra are not the only statistical description important for understanding molecular cloud turbulence. Single point statistics, such as density probability distribution functions, are also used, as well as other two point statistics such as autocorreleation functions. These are all important in numerical and analytical models of star formation (Mac Low & Klessen, 2004a). It would also be worth investigating whether we should, and by how much, be worried about the fact that turbulence power spectra can give almost identical results for very different dynamical behaviour. This would be worthwhile, given that power spectra are the primary go-to tool in turbulence analysis.

References

ABBOTT, D. (1982). The return of mass and energy to the interstellar medium by winds from early-type stars. *ApJ*, **263**, 723. 11

ALŪZAS, R., PITTARD, J., HARTQUIST, T., FALLE, S. & LANGTON, R. (2012). Numerical simulations of shocks encountering clumpy regions. *MNRAS*, **425**. 16

ALŪZAS, R., PITTARD, J., FALLE, S. & HARTQUIST, T. (2014). Numerical simulations of a shock interacting with multiple magnetized clouds. *MNRAS*, **444**. 16

ANDRÉ, P., DI FRANCESCO, J., WARD-THOMPSON, D., INUTSUKA, S.I., PUDRITZ, R.E. & PINEDA, J. (2014). *Protostars and Planets VI*, **27**. 1, 49

AOTA, T., INOUE, T. & AIKAWA, Y. (2013). Thermal instability behind a shock wave in hi and molecular clouds. *ApJ*, **775**, 26. 16, 51

BALBUS, S.A. & HAWLEY, J.F. (1991). A powerful local shear instability in weakly magnetized disks. i-linear analysis. ii-nonlinear evolution. *ApJ*, **376**, 214. 2, 123

BALLESTEROS-PAREDES, J., ROMÁN-ZÚÑIGA, C., SALOMÉ, Q., ZAMORA-AVILÉS, M. & JIMÉNEZ-DONAIRE, M.J. (2019). What is the physics behind the Larson mass–size relation? *MNRAS*, **490**, 2648. 121

Banda-Barragán, W.E., Zertuche, F.J., Federrath, C., García Del Valle, J., Brüggen, M. & Wagner, A.Y. (2019). On the dynamics and survival of fractal clouds in galactic winds. *MNRAS*, **486**. 60

Banda-Barragán, W.E., Zertuche, F.J., Federrath, C., García Del Valle, J., Brüggen, M. & Wagner, A.Y. (2019). On the dynamics and survival of fractal clouds in galactic winds. *MNRAS*, **486**. 16

Bergin, E.A. & Tafalla, M. (2007). *Annu. Rev. Astron. Astrophys.*, **45**, 339. 1, 74

Briggs, W.L., Henson, V.E. & McCormick, S.F. (2000). *A multigrid tutorial*. SIAM. 45

Burgers, J.M. (1948). A mathematical model illustrating the theory of turbulence. In *Advances in applied mechanics*, vol. 1, 171. 123, 141, 148

Castor, J.I., Abbott, D.C. & Klein, R.I. (1975). Radiation-driven winds in Of stars. *ApJ*, **195**, 157–174. 12

Chandrasekhar, S. (1961). *Hydrodynamic and hydromagnetic stability*. 18

Chevalier, R. & Clegg, A.W. (1985). Wind from a starburst galaxy nucleus. *Nature*, **317**. 13

Cioffi, D.F., McKee, C.F. & Bertschinger, E. (1988). Dynamics of radiative supernova remnants. *ApJ*, **334**. 14, 100

Clark, P.C., Glover, S.C.O., Klessen, R.S. & Bromm, V. (2011). Gravitational Fragmentation in Turbulent Primordial Gas and the Initial Mass Function of Population III Stars. *ApJ*, **727**, 110. 2, 122

Clark, P.C., Glover, S.C.O., Klessen, R.S. & Bonnell, I.A. (2012). How long does it take to form a molecular cloud? *MNRAS*, **424**, 2599. 2

Cooper, J.L., Bicknell, G.V., Sutherland, R.S. & Bland-Hawthorn, J. (2008). Three-dimensional simulations of a starburst-driven galactic wind. *ApJ*, **674**, 157. 13

Cooper, J.L., Bicknell, G.V., Sutherland, R.S. & Bland-Hawthorn, J. (2009). Starburst-driven galactic winds: filament formation and emission processes. *ApJ*, **703**, 330. 13

Courant, R. & Friedrichs, K.O. (1999). *Supersonic flow and shock waves*, vol. 21. Springer Science & Business Media. 27

Courant, R., Friedrichs, K. & Lewy, H. (1967). On the partial difference equations of mathematical physics. *IBM journal of Research and Development*, **11**. 38

Dinnbier, F., Wünsch, R., Whitworth, A.P. & Palouš, J. (2017). Fragmentation of vertically stratified gaseous layers: monolithic or coalescence-driven collapse. *MNRAS*, **466**, 4423–4441. 108

Dobbs, C. & Bonnell, I. (2008). Simulations of spiral galaxies with an active potential: molecular cloud formation and gas dynamics. *MNRAS*, **385**, 1893. 2, 123

Dobbs, C., Glover, S., Clark, P. & Klessen, R. (2008). The ism in spiral galaxies: can cooling in spiral shocks produce molecular clouds? *MNRAS*, **389**, 1097. 2, 123

DRAINE, B.T. (2011). *Physics of the interstellar and intergalactic medium*. Princeton series in astrophysics, Princeton University Press, Princeton, N.J. xxix, 4, 5, 6, 14, 150

ELLING, V. (2009). The carbuncle phenomenon is incurable. *Acta Mathematica Scientia*, **29**. 91

ELMEGREEN, B.G. & SCALO, J. (2004). Interstellar turbulence i: Observations. *Annu. Rev. Astron. Astrophys*, **42**. 123

FALLE, S. (1991). Self-similar jets. *MNRAS*, **250**. 40, 52, 88, 89

FALLE, S. (2005). Amr applied to non-linear elastodynamics. In *Adaptive Mesh Refinement-Theory and Applications*, Springer. 52, 88

FALLE, S., KOMISSAROV, S. & JOARDER, P. (1998). A multidimensional upwind scheme for magnetohydrodynamics. *MNRAS*, **297**. 36

FALLE, S., WAREING, C. & PITTARD, J. (2020). Thermal instability revisited. *MNRAS*, **492**, 4484. 56, 72, 108

FEDERRATH, C. (2013a). On the universality of supersonic turbulence. *MNRAS*, **436**, 1245. 122

FEDERRATH, C. (2013b). On the universality of supersonic turbulence. *MNRAS*, **436**, 1245. 124

FEDERRATH, C. (2016). On the universality of interstellar filaments: theory meets simulations and observations. *MNRAS*, **457**. 122

FEDERRATH, C. & KLESSEN, R.S. (2013). On the star formation efficiency of turbulent magnetized clouds. *ApJ*, **763**, 51. 126, 142

FEDERRATH, C., BANERJEE, R., CLARK, P.C. & KLESSEN, R.S. (2010). Modeling collapse and accretion in turbulent gas clouds: implementation and comparison of sink particles in amr and sph. *ApJ*, **713**, 269. 76

FEDERRATH, C., SUR, S., SCHLEICHER, D.R., BANERJEE, R. & KLESSEN, R.S. (2011). A new jeans resolution criterion for (m) hd simulations of self-gravitating gas: application to magnetic field amplification by gravity-driven turbulence. *ApJ*, **731**, 62. 2

FERLAND, G., KORISTA, K., VERNER, D., FERGUSON, J., KINGDON, J. & VERNER, E. (1998). Cloudy 90: numerical simulation of plasmas and their spectra. *Publications of the Astronomical Society of the Pacific*, **110**, 761. 43

FERRIERE, K.M. (2001). The interstellar environment of our galaxy. *Reviews of Modern Physics*, **73**, 1031. 4

FIELD, G., GOLDSMITH, D. & HABING, H. (1969). Cosmic-ray heating of the interstellar gas. *ApJ*, **155**, L149. 2, 4, 49, 61

FIELD, G.B. (1965). Thermal instability. *ApJ*, **142**, 531. 2, 6, 9, 49

FIELD, G.B., BLACKMAN, E.G. & KETO, E.R. (2008). A model of cloud fragmentation. *MNRAS*, **385**, 181. 2, 123

FIELDING, D., QUATAERT, E. & MARTIZZI, D. (2018). Clustered supernovae drive powerful galactic winds after superbubble breakout. *MNRAS*, **481**. 151

FRAGILE, P.C., MURRAY, S.D., ANNINOS, P. & VAN BREUGEL, W. (2004). *ApJ*, **604**, 74. 16

FRAGILE, P.C., ANNINOS, P., GUSTAFSON, K. & MURRAY, S.D. (2005). *ApJ*, **619**, 327. 16

Franeck, A., Wünsch, R., Martínez-González, S., Orlitová, I., Boorman, P., Svoboda, J., Szécsi, D. & Douna, V. (2022). X-ray emission from star-cluster winds in starburst galaxies. *ApJ*, **927**, 212. 13

Gazol, A., Vázquez-Semadeni, E. & Kim, J. (2005). *ApJ*, **630**, 911. 57

Gnat, O. & Ferland, G.J. (2012). Ion-by-ion cooling efficiencies. *ApJSupplement Series*, **199**, 20. 43

Godunov, S.K. (1959). *Matematicheskii Sbornik*, **89**, 271. 31, 38, 89, 133

Goldsmith, K. & Pittard, J. (2016). The interaction of a magnetohydrodynamical shock with a filament. *MNRAS*, **461**, 578. 16

Goldsmith, K. & Pittard, J. (2020). The isothermal evolution of a shock-filament interaction. *MNRAS*, **491**, 4783. 16, 151

Goldsmith, P.F., Heyer, M., Narayanan, G., Snell, R., Li, D. & Brunt, C. (2008). Large-scale structure of the molecular gas in taurus revealed by high linear dynamic range spectral line mapping. *ApJ*, **680**, 428. 50

Harper-Clark, E. & Murray, N. (2009). One-dimensional dynamical models of the carina nebula bubble. *ApJ*, **693**, 1696. 13

Heitsch, F., Stone, J.M. & Hartmann, L.W. (2009). Effects of magnetic field strength and orientation on molecular cloud formation. *ApJ*, **695**, 248. 16, 51

Hennebelle, P. & Audit, E. (2007). *A&A*, **465**, 431. 57

Hennebelle, P. & Chabrier, G. (2008). Analytical Theory for the Initial Mass Function: CO Clumps and Prestellar Cores. *ApJ*, **684**. 122

Hennebelle, P. & Chabrier, G. (2009). ANALYTICAL THEORY FOR THE INITIAL MASS FUNCTION. II. PROPERTIES OF THE FLOW. *ApJ*, **702**. 122

Hennebelle, P. & Chabrier, G. (2013). ANALYTICAL THEORY FOR THE INITIAL MASS FUNCTION. III. TIME DEPENDENCE AND STAR FORMATION RATE. *ApJ*, **770**. 122

Hennebelle, P. & Falgarone, E. (2012). Turbulent molecular clouds. *The Astronomy and Astrophysics Review*, **20**, 55. 122

Hennebelle, P. & Iffrig, O. (2014). Simulations of magnetized multiphase galactic disc regulated by supernovae explosions. *Astronomy & Astrophysics*, **570**, A81. 13

Hill, A.S., Joung, M.R., Mac Low, M.M., Benjamin, R.A., Haffner, L.M., Klingenberg, C. & Waagan, K. (2012). Vertical structure of a supernova-driven turbulent, magnetized interstellar medium. *ApJ*, **750**, 104. 13

Hollenbach, D.J. & Tielens, A. (1999). Photodissociation regions in the interstellar medium of galaxies. *Reviews of Modern Physics*, **71**, 173. 12

Hopkins, P.F. (2012a). An excursion-set model for the structure of giant molecular clouds and the interstellar medium: *ISM structure and growth histories. MNRAS*, **423**. 122

Hopkins, P.F. (2012b). The stellar initial mass function, core mass function and the last-crossing distribution: *The CMF and stellar IMF. MNRAS*, **423**. 122

HOPKINS, P.F. (2013a). A general theory of turbulent fragmentation. *MNRAS*, **430**. 122

HOPKINS, P.F. (2013b). Why do stars form in clusters? An analytic model for stellar correlation functions. *MNRAS*, **428**, 1950. 122

HOYLE, F. (1953). On the fragmentation of gas clouds into galaxies and stars. *ApJ*, **118**, 513. 2

HUBBER, D., FALLE, S. & GOODWIN, S. (2013). Convergence of amr and sph simulations – i. hydrodynamical resolution and convergence tests. *MNRAS*, **432**, 711. 52, 88

INOUE, T. & INUTSUKA, S.I. (2009). Two-fluid magnetohydrodynamics simulations of converging hi flows in the interstellar medium. ii. are molecular clouds generated directly from a warm neutral medium? *ApJ*, **704**, 161. 16, 51, 66

INOUE, T. & INUTSUKA, S.I. (2012). Formation of turbulent and magnetized molecular clouds via accretion flows of h i clouds. *ApJ*, **759**, 35. 9

INOUE, T. & INUTSUKA, S.I. (2016). Formation of h i clouds in shock-compressed interstellar medium: Physical origin of angular correlation between filamentary structure and magnetic field. *ApJ*, **833**, 10. 66

INOUE, T. & OMUKAI, K. (2015). *ApJ*, **805**, 73. 16, 51, 57

JEANS, J.H. (1902). I. the stability of a spherical nebula. *Philosophical Transactions of the Royal Society of London. Series A, Containing Papers of a Mathematical or Physical Character*, **199**, 1. 10

JIANG, B., CHEN, Y., WANG, J., SU, Y., ZHOU, X., SAFI-HARB, S. & DELANEY, T. (2010). Cavity of molecular gas associated with supernova remnant 3c 397. *ApJ*, **712**, 1147. 16

KAASTRA, J.S. (1992). An x-ray spectral code for optically thin plasma. *Internal SRON-Leiden Report*. 43

KIM, C.G., KIM, W.T. & OSTRIKER, E.C. (2008). *ApJ*, **681**, 1148. 2, 9, 123

KIM, C.G., KIM, W.T. & OSTRIKER, E.C. (2010). Galactic spiral shocks with thermal instability in vertically stratified galactic disks. *ApJ Letters*, **720**, 1454. 2

KIM, C.G., KIM, W.T. & OSTRIKER, E.C. (2011). Regulation of star formation rates in multiphase galactic disks: numerical tests of the thermal/dynamical equilibrium model. *ApJ*, **743**, 25. 13

KIM, C.G., OSTRIKER, E.C. & KIM, W.T. (2013). Three-dimensional hydrodynamic simulations of multiphase galactic disks with star formation feedback. i. regulation of star formation rates. *ApJ*, **776**, 1. 13

KINOSHITA, S.W., NAKAMURA, F. & WU, B. (2021). Star formation triggered by shocks. *ApJ*, **921**, 150. 87

KLEIN, R.I., MCKEE, C.F. & COLELLA, P. (1994). *ApJ*, **420**, 213. 3, 15, 59, 87, 151

KLESSEN, R.S. & HENNEBELLE, P. (2010). Accretion-driven turbulence as universal process: galaxies, molecular clouds, and protostellar disks. *A&A*, **520**. 2

KOENIG, X., LEISAWITZ, D., BENFORD, D., REBULL, L., PADGETT, D. & ASSEF, R. (2011). Wide-field infrared survey explorer observations of the evolution of massive star-forming regions. *ApJ*, **744**, 130. 11

KOLMOGOROV, A.N. (1941). *Cr Acad. Sci. URSS*, **30**, 301. 123, 141, 148

KOO, B.C., RHO, J., REACH, W.T., JUNG, J. & MANGUM, J.G. (2001). Shocked molecular gas in the supernova remnant hb 21. *ApJ*, **552**, 175. 15

KOWAL, G., LAZARIAN, A. & BERESNYAK, A. (2007). Density fluctuations in mhd turbulence: spectra, intermittency, and topology. *ApJ*, **658**, 423. 126, 130, 134, 138, 142

KOYAMA, H. & INUTSUKA, S.I. (2000). Molecular cloud formation in shock-compressed layers. *ApJ*, **532**, 980. 41

KOYAMA, H. & INUTSUKA, S.I. (2002). *ApJL*, **564**, L97. xix, 42, 43

KOYAMA, H. & INUTSUKA, S.I. (2004). The field condition: a new constraint on spatial resolution in simulations of the nonlinear development of thermal instability. *ApJ*, **602**, L25. 56

KRAVTSOV, A.V. (2003). On the Origin of the Global Schmidt Law of Star Formation. *ApJ*, **590**. 122

KRITSUK, A.G., NORMAN, M.L., PADOAN, P. & WAGNER, R. (2007). The statistics of supersonic isothermal turbulence. *ApJ*, **665**, 416. 126, 142

KROUPA, P. (2001). On the variation of the initial mass function. *MNRAS*, **322**, 231. 11

KRUMHOLZ, M.R. (2014). The big problems in star formation: The star formation rate, stellar clustering, and the initial mass function | Elsevier Enhanced Reader. *Physics Reports*, **539**. 122, 128

KRUMHOLZ, M.R. (2015). notes on star formation. *arXiv preprint arXiv:1511.03457*. 9, 11

Krumholz, M.R., Stone, J.M. & Gardiner, T.A. (2007). Magnetohydrodynamic evolution of h ii regions in molecular clouds: simulation methodology, tests, and uniform media. *ApJ*, **671**, 518. 24

Kudritzki, R.P. & Puls, J. (2000). Winds from hot stars. *ARA&A*, **38**, 613. 12

Kupilas, M.M., Wareing, C.J., Pittard, J.M. & Falle, S. (2021). Interactions of a shock with a molecular cloud at various stages of its evolution due to thermal instability and gravity. *MNRAS*, **501**, 3137. 16, 49, 121, 124

Kupilas, M.M., Pittard, J.M., Wareing, C.J. & Falle, S. (2022). Shocking interactions of supernova remnants with atomic and molecular clouds - the interplay between shocks, thermal instability and gravity in the large cloud regime. *MNRAS in press*. 87

Kurganov, A. & Tadmor, E. (2000). *Journal of Computational Physics*, **160**, 241. 89, 133

Larson, R.B. (1981). *MNRAS*, **194**, 809. 1, 49, 121

Lazarian, A. (2009). Obtaining spectra of turbulent velocity from observations. *Space Science Reviews*, **143**, 357. 124

Leao, M., de Gouveia Dal Pino, E., Falceta-Gonçalves, D., Melioli, C. & Geraissate, F. (2009). Local star formation triggered by supernova shocks in magnetized diffuse neutral clouds. *MNRAS*, **394**, 157. 16

Li, P.S., Myers, A. & McKee, C.F. (2012). AMBIPOLAR DIFFUSION HEATING IN TURBULENT SYSTEMS. *ApJ*, **760**. 122

Lim, A., Falle, S. & Hartquist, T. (2005). The production of magnetically dominated star-forming regions. *ApJ*, **632**, L91. 9

Mac Low, M.M. & Klessen, R.S. (2004a). Control of star formation by supersonic turbulence. *Reviews of Modern Physics*, **76**. 13, 122, 142, 152

Mac Low, M.M. & Klessen, R.S. (2004b). Control of star formation by supersonic turbulence. *Reviews of modern physics*, **76**, 125. 128

Mac Low, M.M., McKee, C.F., Klein, R.I., Stone, J.M. & Norman, M.L. (1994). Shock Interactions with Magnetized Interstellar Clouds. I. Steady Shocks Hitting Nonradiative Clouds. *ApJ*, **433**, 757. 16

McKee, C.F. & Ostriker, E.C. (2007). Theory of Star Formation. *ARA&A*, **45**. 122

McKee, C.F. & Ostriker, J.P. (1977). A theory of the interstellar medium-three components regulated by supernova explosions in an inhomogeneous substrate. *ApJ*, **218**. 4, 13

McKee, C.F. & Zweibel, E.G. (1992). On the virial theorem for turbulent molecular clouds. *ApJ*, **399**, 551. 9

McKee, C.F., Hollenbach, D.J., Seab, G.C. & Tielens, A. (1987). The structure of the time-dependent interstellar shocks and grain destruction in the interstellar medium. *ApJ*, **318**. 19, 151

Mewe, R., Kaastra, J.S. & Liedahl, D.A. (1992). An x-ray spectral code for optically thin plasma. *Legacy, 6, 16*. 43

Michaut, C., Cavet, C., Bouquet, S., Roy, F. & Nguyen, H. (2012). Numerical study of the vishniac instability in supernova remnants. *ApJ*, **759**, 78. 69

Nakamura, F., McKee, C.F., Klein, R.I. & Fisher, R.T. (2006). *ApJSS*, **164**, 477. 16, 54, 87

Obergaulinger, M., Iyudin, A., Müller, E. & Smoot, G. (2014). Hydrodynamic simulations of the interaction of supernova shock waves with a clumpy environment: the case of the rx j0852. 0- 4622 (vela jr) supernova remnant. *MNRAS*, **437**. 16

Osterbrock, D. & Ferland, G. (2006). Astrophysics of gaseous nebulae and active galactic nuclei, 2n [nasa ads] d ed., ed. *DE Osterbrock, & GJ Ferland (Sausalito, CA: University Science Books)(In the text)*. 43

Padoan, P. & Nordlund, A. (2002). The Stellar Initial Mass Function from Turbulent Fragmentation. *ApJ*, **576**. 122

Padoan, P., Pan, L., Haugbølle, T. & Nordlund, Å. (2016). Supernova driving. i. the origin of molecular cloud turbulence. *ApJ*, **822**, 11. 13, 123, 151

Parker, E.N. (1953). Instability of thermal fields. *ApJ*, **117**, 431. 2, 9, 49

Pattle, K., Ward-Thompson, D., Berry, D., Hatchell, J., Chen, H.R., Pon, A., Koch, P.M., Kwon, W., Kim, J., Bastien, P. *et al.* (2017). The jcmt bistro survey: the magnetic field strength in the orion a filament. *ApJ*, **846**, 122. 50

Peretto, N., André, P., Könyves, V., Schneider, N., Arzoumanian, D., Palmeirim, P., Didelon, P., Attard, M., Bernard, J., Di Francesco, J. *et al.* (2012). The pipe nebula as seen with herschel: formation of filamentary structures by large-scale compression? *Astronomy & Astrophysics*, **541**, A63. 15

Pittard, J. & Parkin, E. (2016a). *MNRAS*, **457**, 4470. 16

Pittard, J., Dyson, J., Falle, S. & Hartquist, T. (2003). The formation of broad emission line regions in supernova-qso wind interactions-ii. 2d calculations. *A&A*, **408**, 79. 69

Pittard, J., Hartquist, T. & Falle, S. (2010). *MNRAS*, **405**, 821. 16

Pittard, J., Wareing, C. & Kupilas, M. (2021a). How to inflate a wind-blown bubble. *MNRAS*, **508**, 1768. 12

Pittard, J.M. (2011). Tails of the unexpected: the interaction of an isothermal shell with a cloud. *MNRAS letters*, **411**, L41–L45. 16, 87, 114

Pittard, J.M. & Goldsmith, K.J.A. (2016). *MNRAS*, **458**, 1139–1163. 16

Pittard, J.M. & Parkin, E.R. (2016b). The turbulent destruction of clouds – III. Three-dimensional adiabatic shock–cloud simulations. *MNRAS*, **457**, 4470. 16

Pittard, J.M., Falle, S., Hartquist, T.W. & Dyson, J.E. (2009). *MNRAS*, **394**, 1351. 16, 54, 87

Pittard, J.M., Kupilas, M.M. & Wareing, C.J. (2021b). How D-type Hiiregion expansion depends on numerical resolution. *MNRAS*, **510**, 2797–2801. 12

Poludnenko, A.Y., Frank, A. & Blackman, E.G. (2002). Hydrodynamic Interaction of Strong Shocks with Inhomogeneous Media. I. Adiabatic Case. *ApJ*, **576**. 16

Quirk, J.J. (1997). A contribution to the great riemann solver debate. In *Upwind and High-Resolution Schemes*, Springer. 59, 91

Ranjan, D., Oakley, J. & Bonazza, R. (2011). Shock-Bubble Interactions. *Annual Review of Fluid Mechanics*, **43**. 16

Roe, P.L. (1981). Approximate riemann solvers, parameter vectors, and difference schemes. *Journal of computational physics*, **43**. 24

Rogers, H. & Pittard, J. (2013). Feedback from winds and supernovae in massive stellar clusters i. hydrodynamics. *MNRAS*, **431**, 1337. 2, 13

Rupke, D.S. (2018). A review of recent observations of galactic winds driven by star formation. *Galaxies*, **6**, 138. 151

Saury, E., Miville-Deschênes, M.A., Hennebelle, P., Audit, E. & Schmidt, W. (2014). The structure of the thermally bistable and turbulent atomic gas in the local interstellar medium. *A&A*, **567**, A16. 2, 123

Scannapieco, E. & Brüggen, M. (2015). The launching of cold clouds by galaxy outflows. i. hydrodynamic interactions with radiative cooling. *ApJ*, **805**, 158. 16

Schneider, E.E. & Robertson, B.E. (2017). Hydrodynamical coupling of mass and momentum in multiphase galactic winds. *ApJ*, **834**, 144. 13

Schneider, N., Bontemps, S., Simon, R., Jakob, H., Motte, F., Miller, M., Kramer, C. & Stutzki, J. (2006). A new view of the cygnus x region-kosma co 2 1, 3 2, and co 3 2 imaging. *Astronomy & Astrophysics*, **458**. 15

Sedov, L.I. (1959). *Similarity and Dimensional Methods in Mechanics*. 14

Seifried, D., Walch, S., Haid, S., Girichidis, P. & Naab, T. (2018). Is molecular cloud turbulence driven by external supernova explosions? *ApJ*, **855**, 81. 104, 149, 151

SHETTY, R. & OSTRIKER, E.C. (2012). Maximally star-forming galactic disks. ii. vertically resolved hydrodynamic simulations of starburst regulation. *ApJ*, **754**, 2. 13

SOD, G.A. (1978). A survey of several finite difference methods for systems of nonlinear hyperbolic conservation laws. *Journal of computational physics*, **27**. 35

SOLOMON, P., RIVOLO, A., BARRETT, J. & YAHIL, A. (1987). *ApJ*, **319**, 730. 1, 121

STERN, J., HENNAWI, J.F., PROCHASKA, J.X. & WERK, J.K. (2016). A universal density structure for circumgalactic gas. *ApJ*, **830**, 87. 9

STEVENS, I.R. & HARTWELL, J.M. (2003). The cluster wind from local massive star clusters. *MNRAS*, **339**. 13

STRICKLAND, D.K. & HECKMAN, T.M. (2009). Supernova feedback efficiency and mass loading in the starburst and galactic superwind exemplar m82. *ApJ*, **697**, 2030. 151

STUTZ, A.M. & GOULD, A. (2016). Slingshot mechanism in orion: Kinematic evidence for ejection of protostars by filaments. *A&A*, **590**, A2. 50

STUTZ, A.M., GONZALEZ-LOBOS, V.I. & GOULD, A. (2018). Gaia: Orion's Integral Shaped Filament is a Standing Wave. *MNRAS submitted. arXiv:1807.11496*. 50

TAMBURRO, D., RIX, H.W., LEROY, A., MAC LOW, M.M., WALTER, F., KENNICUTT, R., BRINKS, E. & DE BLOK, W. (2009). What is driving the h i velocity dispersion? *AJ*, **137**, 4424. 2, 123

TAN, J.C. (2000). Star formation rates in disk galaxies and circumnuclear starbursts from cloud collisions. *ApJ*, **536**, 173. 2

TAYLOR, G. (1950). *Proceedings of the Royal Society of London Series A*, **201**, 159–174. 14

TORO, E.F. (2009). *Riemann solvers and numerical methods for fluid dynamics: a practical introduction*. Springer Science & Business Media. 26, 35

TRUELOVE, J.K., KLEIN, R.I., MCKEE, C.F., HOLLIMAN II, J.H., HOWELL, L.H. & GREENOUGH, J.A. (1997). *ApJ*, **489**, L179. 59

VAN LEER, B. (1977). *Journal of computational physics*, **23**, 276. 38

VAN LOO, S., FALLE, S., HARTQUIST, T. & MOORE, T. (2007). *A&A*, **471**, 213. 16, 51, 87

VAN LOO, S., FALLE, S. & HARTQUIST, T.W. (2010). *MNRAS*, **406**, 1260. 16, 51, 66, 71

VAN LOO, S., KETO, E. & ZHANG, Q. (2014). Core and filament formation in magnetized, self-gravitating isothermal layers. *ApJ*, **789**, 37. 2, 123

VÁZQUEZ-SEMADENI, E., RYU, D., PASSOT, T., GONZÁLEZ, R.F. & GAZOL, A. (2006). Molecular cloud evolution. i. molecular cloud and thin cold neutral medium sheet formation. *ApJ*, **643**, 245. 57

VÁZQUEZ-SEMADENI, E., GÓMEZ, G.C., JAPPSEN, A.K., BALLESTEROS-PAREDES, J., GONZÁLEZ, R.F. & KLESSEN, R.S. (2007). *ApJ*, **657**, 870. 43

VÁZQUEZ-SEMADENI, E., PALAU, A., BALLESTEROS-PAREDES, J., GÓMEZ, G.C. & ZAMORA-AVILÉS, M. (2019). Global hierarchical collapse in molecular clouds. towards a comprehensive scenario. *MNRAS*, **490**, 3061. 123

VISHNIAC, E. (1983). The dynamic and gravitational instabilities of spherical shocks. *ApJ*, **274**, 152. 16, 69

VISHNIAC, E.T. (1994). Nonlinear instabilities in shock-bounded slabs. *ApJ*, **428**. 16

VÁZQUEZ-SEMADENI, E., PALAU, A., BALLESTEROS-PAREDES, J., GÓMEZ, G.C. & ZAMORA-AVILÉS, M. (2019). Global hierarchical collapse in molecular clouds. Towards a comprehensive scenario. *MNRAS*, **490**. 145

WAREING, C., PITTARD, J. & FALLE, S. (2016b). Magnetohydrodynamic simulations of mechanical stellar feedback in a sheet-like molecular cloud. *MNRAS*, **465**, 2757. 2, 3, 13

WAREING, C.J., PITTARD, J.M. & FALLE, S. (2017). Hydrodynamic simulations of mechanical stellar feedback in a molecular cloud formed by thermal instability. *MNRAS*, **470**, 2283. 2, 3, 13

WAREING, C.J., PITTARD, J.M., WRIGHT, N.J. & FALLE, S.A.E.G. (2018). A new mechanical stellar wind feedback model for the rosette nebula. *MNRAS*, **475**, 3598. 2, 3, 13

WAREING, C., FALLE, S. & PITTARD, J. (2019). Sheets, filaments, and clumps – high-resolution simulations of how the thermal instability can form molecular clouds. *MNRAS*, **485**. 9, 50, 114, 118, 123, 144, 151

WAREING, C., PITTARD, J. & FALLE, S. (2021). Striations, integrals, hourglasses, and collapse – thermal instability driven magnetic simulations of molecular clouds. *MNRAS*, **500**. 9, 50, 89, 123, 151

WADA, K. & NORMAN, C.A. (2007). Density Structure of the Interstellar Medium and the Star Formation Rate in Galactic Disks. *ApJ*, **660**. 122

Walch, S., Girichidis, P., Naab, T., Gatto, A., Glover, S.C.O., Wünsch, R., Klessen, R.S., Clark, P.C., Peters, T., Derigs, D. & Baczynski, C. (2015). The SILCC (SImulating the LifeCycle of molecular Clouds) project - I. Chemical evolution of the supernova-driven ISM. *MNRAS*, **454**, 238. 13

Wareing, C., Pittard, J., Falle, S. & Van Loo, S. (2016a). Magnetohydrodynamical simulation of the formation of clumps and filaments in quiescent diffuse medium by thermal instability. *MNRAS*, **459**, 1803. v, 2, 41, 50, 87, 143, 151

Wareing, C. (2005). *Hydrodynamical modelling of planetary nebulae and their interaction with the interstellar medium.thesis*. Ph.D. thesis. 47

Weaver, R., McCray, R., Castor, J., Shapiro, P. & Moore, R. (1977). Interstellar bubbles. II. Structure and evolution. *ApJ*, **218**, 377–395. 12

Westmoquette, M., Slavin, J., Smith, L. & Gallagher, J. (2010). Vlt/flames-argus observations of stellar wind–ism cloud interactions in ngc 6357. *MNRAS*, **402**. 15

Whitworth, A.P., Bhattal, A.S., Chapman, S.J., Disney, M.J. & Turner, J.A. (1994). Fragmentation of shocked interstellar gas layers. *A&A*, **290**, 421–427. 108

Williams, J.P., Blitz, L. & Stark, A.A. (1995). The density structure in the rosette molecular cloud: Signposts of evolution. *ApJ*, **451**, 252. 75

Wolfire, M.G., Hollenbach, D., McKee, C.F., Tielens, A. & Bakes, E. (1995). The neutral atomic phases of the interstellar medium. *ApJ*, **443**, 152. xviii, 2, 4, 7, 8, 41, 49

Wolfire, M.G., McKee, C.F., Hollenbach, D. & Tielens, A. (2003). Neutral atomic phases of the interstellar medium in the galaxy. *ApJ*, **587**, 278. 2, 4, 49

Woltjer, L. (1972). Supernova Remnants. *ARA&A*, **10**, 129. 14

Woosley, S.E. & Weaver, T.A. (1986). The physics of supernova explosions. *ARA&A*, **24**. 14

Wu, B., Van Loo, S., Tan, J.C. & Bruderer, S. (2015). Gmc collisions as triggers of star formation. i. parameter space exploration with 2d simulations. *ApJ*, **811**, 56. 2

Wu, B., Tan, J.C., Christie, D., Nakamura, F., Van Loo, S. & Collins, D. (2017a). Gmc collisions as triggers of star formation. iii. density and magnetically regulated star formation. *ApJ*, **841**, 88. 2

Wu, B., Tan, J.C., Nakamura, F., Van Loo, S., Christie, D. & Collins, D. (2017b). Gmc collisions as triggers of star formation. ii. 3d turbulent, magnetized simulations. *ApJ*, **835**, 137. 2

Wu, B., Tan, J.C., Nakamura, F., Christie, D. & Li, Q. (2018). Giant molecular cloud collisions as triggers of star formation. vi. collision-induced turbulence. *PASJ*, **70**, S57. 2, 123

Xia, C. & Keppens, R. (2016). Formation and plasma circulation of solar prominences. *ApJ*, **823**, 22. 9

Yang, C.C. & Krumholz, M. (2012). Thermal-instability-driven turbulent mixing in galactic disks. i. effective mixing of metals. *ApJ*, **758**, 48. 2, 123

Yirak, K., Frank, A. & Cunningham, A.J. (2010). Self-convergence of radiatively cooling clumps in the interstellar medium. *ApJ*, **722**, 412. 16